NASA-CR-204105

SRI International

Final
IN-46-CR
OCIT
024 319
62P

Final Technical Report • March 1997

MODELING OF THE COUPLED MAGNETOSPHERIC AND NEUTRAL WIND DYNAMOS

SRI Project 4604

Submitted by:

Jeffrey P. Thayer, Senior Research Physicist
Radio Sciences Center

Prepared for:

National Aeronautics and Space Administration Headquarters
Space Physics Division
Washington, D.C. 20546

Attention: Mary Mellott, Code: SS
NASA Technical Officer

Grant: NAGW-3508

Approved:

Murray J. Baron, Vice President and Director
Radio Sciences Center

333 Ravenswood Avenue • Menlo Park, CA 94025-3493 • (415) 326-6200 • FAX (415) 326-5512 • Telex 334486

CONTENTS

APPENDIX A: Gary, J.B., R.A. Heelis, W.B. Hanson, and J.A. Slavin, "Field-aligned Poynting flux observations in the high-latitude ionosphere,"*J. Geophys. Res.*, 87, 11417-11427, 1994

APPENDIX B: Thayer, J.P., J.F. Vickrey, R.A. Heelis, and J.B. Gary, "Interpretation and modeling of the high-latitude electromagnetic energy flux," *J. Geophys. Res.*, Vol. 100, No. A10, pp. 19,715-19,728, 1995

APPENDIX C: Gary, J.B., R.A. Heelis, and J.P. Thayer, "Summary of field-aligned Poynting flux observations from DE 2," *Geophys. Res. Lett*, 1861-1864, 1995

APPENDIX D: Thayer, J.P., "Height-resolved Joule heating rates in the high-latitude E region and the influence of neutral winds," submitted to the *Journal of Geophysical Research*

1 PROJECT SUMMARY

This final report summarizes the results of NASA Grant No. NAGW-3508 entitled "Modeling of the Coupled Magnetospheric and Neutral Wind Dynamos." Over the past four years of funding, SRI, in collaboration with the University of Texas at Dallas, has been involved in assessing the influence of thermospheric neutral winds on the electric field and current systems at high latitudes. The initial direction of the project was to perform a set of numerical experiments concerning the contribution of the magnetospheric and neutral wind dynamo processes, under specific boundary conditions, to the polarization electric field and/or the field-aligned current distribution at high latitudes. To facilitate these numerical experiments we developed a numerical scheme that relied on using output from the NCAR Thermosphere–Ionosphere General Circulation Model (NCAR–TIGCM), expanding them in the form of spherical harmonics and solving the dynamo equations spectrally. Once initial calculations were completed, it was recognized that the neutral wind contribution could be significant but its actual contribution to the electric field or currents depended strongly on the generator properties of the magnetosphere. Solutions to this problem are not unique because of the unknown characteristics of the magnetospheric generator, therefore the focus was on two limiting cases. One limiting case was to consider the magnetosphere as a voltage generator delivering a fixed voltage to the high-latitude ionosphere and allowing for the neutral wind dynamo to contribute only to the current system. The second limiting case was to consider the magnetosphere as a current generator and allowing for the neutral wind dynamo to contribute only to the generation of polarization electric fields. This work was completed and presented at the1994 Fall AGU meeting.

The direction of the project then shifted to applying the Poynting flux concept to the high-latitude ionosphere. This concept was more attractive as it evaluated the influence of neutral winds on the high-latitude electrodynamics without actually having to determine the generator characteristics of the magnetosphere. The influence of the neutral wind was then determined not by estimating how much electric potential or current density it provides, but by determining the contribution of the neutral wind to the net electromagnetic energy transferred between the ionosphere and magnetosphere. The estimate of the net electromagnetic energy transfer and the role of the neutral winds proves to be a more fundamental quantity in studies of magnetosphere–ionosphere coupling [e.g., Kelley et al., 1991; Cowley et al., 1991; Thayer and Vickrey, 1992]. Kelley et al., [1991] also showed that by using electric and magnetic field measurements from the HILAT satellite, the Poynting flux could be a measurable quantity from polar-orbiting, low-altitude spacecraft. Through collaboration with Dr. Heelis and others at UTD and their expertise of the electric field measurements on the DE-B satellite, an extensive analysis was planned to determine the Poynting flux from the DE-B measurements in combination with a modeling effort

to help interpret the observations taking into account the coupled magnetosphere–ionosphere (MI) system.

This effort has been very successful in establishing the DC Poynting flux as a fundamental quantity in describing the coupling of electromagnetic energy between the magnetosphere and ionosphere. The DE-B satellite electric and magnetic field measurements were carefully scrutinized to provide, for the first time, a large data set of DC, field-aligned, Poynting flux measurements. Investigations describing the field-aligned Poynting flux observations from DE-B orbits under specific geomagnetic conditions and from many orbits, were conducted to provide a statistical average of the Poynting flux distribution over the polar cap. The theoretical modeling effort has provided insight into the observations by formulating the connection between Poynting's theorem and the electromagnetic energy conversion processes that occur in the ionosphere. Modeling and evaluation of these processes has helped interpret the satellite observations of the DC Poynting flux and improve our understanding of the coupling between the ionosphere and magnetosphere.

Upon evaluating the DE-B measurements and developing the numerical experiments to evaluate the Poynting flux, it was realized that the electrical characteristics of the E region (i.e., conductivity, neutral winds, and electric fields) and the vertical extent of the magnetospheric coupling into the high-latitude E region was important for interpreting the Poynting flux measurement and was poorly represented in the theoretical models. At the same time, new operating modes were being implemented at the Sondrestrom incoherent-scatter radar facility that vastly improved the radar's capability to probe at high resolution the electrodynamic behavior of the high-latitude ionosphere. Although the satellite measurement could provide the net electromagnetic transfer between the magnetosphere and ionosphere, it could not determine how this energy was distributed within the E region. The radar measurements provided an opportunity to evaluate the altitude distribution of the electromagnetic energy transfer rate at high latitudes as well as the partitioning of this electromagnetic energy into other energy forms (such as Joule heating and mechanical energy) and the influence of the neutral wind on the electromagnetic energy transfer. Thus, the third and final effort within the project was to pursue the distribution in altitude of the electromagnetic energy transfer in the high-latitude E region through the use of measurements by the Sondrestrom incoherent-scatter radar.

As evidence for the success of this project, three publications and two additional manuscripts (one recently submitted to the *Journal of Geophysical Research*, the other in preparation for submission) have been produced. The titles for these manuscripts are given in Section 3 of this report, with the full manuscripts of all but the work in progress manuscript included as appendices. Highlights from these manuscripts are given in the following section.

2 PROJECT HIGHLIGHTS

2.1 DE-B POYNTING FLUX OBSERVATIONS: CASE STUDY

Work at the University of Texas at Dallas by J. B. Gary and R. A. Heelis included the careful determination of the electric field and perturbation magnetic field from the DE-B satellite measurements. Significant effort was involved in determining the magnetometer baseline in an automated and physically defensible manner. The results from this effort led to the development of a routine processor for evaluating the field-aligned Poynting flux from the DE-B measurements. This was a necessary step toward determining unambiguously the Poynting flux from the DE-B satellite measurements. J. F. Vickrey and J. P. Thayer contributed to the early development of the DE-B calculations and provided consultation on the interpretation of the measurement. The Poynting flux case study of a few chosen DE-B orbits illustrated that

- The field-aligned Poynting flux is directed mainly downward into the high-latitude ionosphere with typical magnitudes of a few tens of mW/m^2 in the auroral zone and from zero to 10 mW/m^2 inside the polar cap
- Regions of upward Poynting flux were observed over localized regions with magnitudes averaging less than 2 mW/m^2.

2.2 ELECTRODYNAMIC MODEL

Work at SRI involved modeling the exchange of electromagnetic energy between the ionosphere and magnetosphere to help interpret the DE-B Poynting flux observations. In this study a model simulation providing a self-consistent description of the thermosphere and ionosphere was used to study the coupled aspects of the MI system at high latitudes. This approach differs from previous efforts in which the electrodynamic properties of the ionosphere and magnetosphere were evaluated separately to demonstrate the potential role of the neutral winds in the electrodynamics.

To describe the electrical properties of the high-latitude ionosphere, a numerical model was constructed, from the framework provided by the Vector Spherical Harmonic (VSH) model, that determines the ionospheric currents, conductivities, and electric fields including both magnetospheric inputs and neutral wind dynamo effects. This model development grew from the earlier question of whether an electrical energy source in the ionosphere was capable of providing an upward Poynting flux. The model solves the steady-state neutral wind dynamo equations and the Poynting flux equation to provide insight into the electrodynamic role of the neutral winds. The VSH model is based on a spectral representation of the output fields from NCAR–TIGCM simulations. A set of NCAR–TIGCM runs has been expanded into VSH model coefficients that can be used to represent a range of geophysical conditions.

The modeling effort to determine the high-latitude energy flux has been able to reproduce many of the large-scale features observed in the Poynting flux measurements made by DE-2. Because the Poynting flux measurement is an integrated result of energy flux into or out of the ionosphere, we investigated the ionospheric properties that may contribute to the observed flux of energy measured by the spacecraft. The results are summarized in the appended manuscript, Appendix C. Under steady-state conditions the electromagnetic energy flux, or DC Poynting flux, is equal to the Joule heating rate and the mechanical energy transfer rate in the high-latitude ionosphere. Although the Joule heating rate acts as an energy sink, transforming electromagnetic energy into thermal or internal energy of the gas, the mechanical energy transfer rate may be either a sink or source of electromagnetic energy. In the steady state, it is only the mechanical energy transfer rate that can generate electromagnetic energy and result in a DC Poynting flux that is directed out of the ionosphere.

The model simulation led to a number of conclusions.

- The electromagnetic energy flux is predominantly directed into the high-latitude ionosphere, with greater input in the morning sector than the evening sector by a factor of three.
- The Joule heating rate accounts for much of the electromagnetic energy deposited in the ionosphere, with the conductivity-weighted neutral wind contributing significantly to the Joule heating rate and thus to the net electromagnetic energy flux in the ionosphere.
- On average, the mechanical energy transfer rate contributes about 20% to the net electromagnetic energy flux in the dawn, dusk, and polar cap regions, acting as a sink of electromagnetic energy flux in the dawn and dusk sectors and a source of electromagnetic energy flux in the polar cap.
- An upward electromagnetic energy flux is found in the regions near the convection reversal boundaries. This flux is due to the mechanical energy transfer rate exceeding the Joule heating rate. The upward electromagnetic energy flux was found to be small partly due to the relationship of the conductivity-weighted neutral wind to the imposed electric field and partly due to the Joule heating rate increasing irrespective of the source of electromagnetic energy flux.

2.3 DE-B POYNTING FLUX OBSERVATIONS: STATISTICAL STUDY

Using DE-B data of ion drift velocities and magnetic fields, the field-aligned Poynting flux for 576 orbits over the satellite lifetime were calculated. The data were sorted for interplanetary magnetic field conditions (northward and southward IMF) and geomagnetic activity ($K_p \leq 3$ and $K_p > 3$) and binned by invariant latitude and magnetic local time. In general, it was found that the average Poynting flux is directed into the ionosphere over the entire polar cap indicating electric fields of magnetospheric origin generally dominate. The dawnside auroral zone generally has the largest Poynting flux values in the polar cap, exceeding 6 mW/m^2. We also investigated

the distribution of upward Poynting flux and found it never exceeded 3 mW/m^2 over the entire polar cap. An interesting feature in the DE-B data set is the significant occurrence and magnitude of upward Poynting flux in the predawn sector during periods of southward IMF and high K_p conditions.

2.4 HEIGHT-RESOLVED E-REGION ELECTRODYNAMICS AND JOULE HEATING RATES

The improved capability of the Sondrestrom incoherent-scatter radar to sample the E region at high resolution provides new insight into high-latitude E-region electrodynamic behavior in terms of currents, conductivities, electric fields, and neutral winds, and their role in the exchange of electromagnetic energy between the ionosphere and magnetosphere. This capability permitted the direct investigation of electromagnetic energy dissipation—that is, Joule heating—in the high-latitude ionosphere, which is fundamental in M–I coupling. Also, the net Poynting flux could be estimated from the radar measurements by determining the electromagnetic energy transfer rate throughout the ionosphere. The radar estimation of the height-resolved and height-integrated E-region Joule heating rates and the influence of the neutral wind on these estimates is the focus of a paper recently submitted to the *Journal of Geophysical Research* and provided in Appendix D. The following summarizes the conclusions obtained from this study.

1. The ability to measure the height-resolved Joule heating rate, q_j, that includes the neutral wind revealed significantly more structure in both experiments than observed in the q_j^E profiles (whose altitude dependence is described by the Pedersen conductivity). This structure is attributed to the E-region neutral wind and its altitude-dependent influence on the Joule heating rate; often, enhancing the local Joule heating rate at one altitude while reducing the Joule heating rate at another. This led to a number of occasions where a much narrower and more localized enhancement occurred in the height-resolved Joule heating rate. The localization of the E-region Joule heating rate (about 12 km for the cases presented) caused by the presence of the neutral wind is a new observation whose impact on the ionosphere–thermosphere system requires further investigation.

2. The upper E-region neutral winds modify the Joule heating rate in a manner that is associated with the behavior of the electric field. Typically, it was found that when the electric field direction remained steady and only the magnitude of the electric field was enhanced, the neutral winds acted to reduce the upper E-region Joule heating rate. During times when the electric field direction changed significantly, it was found that the neutral winds acted to enhance the upper E-region Joule heating rate. Subsequent counterclockwise rotation of the neutral wind with decreasing altitude typically led to enhancements in the Joule heating rate in the lower E region.

3. The most significant neutral wind contribution to the Joule heating rate came after a substorm period on May 2, 1995, where an enhancement in the height-integrated Joule heating rate by over 400% occurred. Here the majority of the neutral wind contribution came from the

upper E region. This enhancement occurred during a 180° change in electric field direction and an overall reduction in electric field magnitude. Other enhancements of the height-integrated Joule heating rate by 200% were observed to occur during periods of significant changes in the electric field direction. Reduction of the height-integrated Joule heating rate by the neutral winds by as much as 40% were observed during periods of elevated magnitude in the electric field but with the direction of the electric field steady for extended periods.

4. Overall, the estimate of the height-integrated Joule heating rate, Q_j^E, assuming the neutral wind is zero, served as a limited proxy for the two data sets presented and showed an invariance to moderate changes in the ion-neutral collision frequency model. The height-integrated Joule heating rate, Q_j, is more susceptible to changes in the ion-neutral collision frequency model, as the height-resolved profile is inversely proportional to the collision frequency. Yet, the height of maximum Joule heating is best estimated by the q_j profile, which is not influenced by the change in collision frequency. Finally, reasonable changes to the ion-neutral collision frequency model can modify the absolute values presented in this work, but cannot eliminate the neutral wind effects presented nor the trends observed.

2.5 ELECTROMAGNETIC ENERGY TRANSFER RATES

The radar estimation of the height-resolved and height-integrated electromagnetic energy transfer rate is the focus of a paper still in preparation for submission to the *Journal of Geophysical Research*. The proposed title of the manuscript is "Evaluation of electromagnetic energy transfer in the high-latitude E-region as determined by the Sondrestrom incoherent scatter radar" by J.P. Thayer. Because this work is not finalized, we do not include it as an appendix, but provide a brief summary of the approach presented therein.

The transfer of electromagnetic energy flux is a fundamental quantity that describes the electrical exchange between the ionosphere and magnetosphere. The purpose of this paper is to establish that the Sondrestrom radar is capable of providing estimates of this electrical transfer on a routine basis and to interpret these measurements in terms of MI coupling. The approach is to apply high-resolution electrodynamic measurements of the E region determined by the Sondrestrom radar to evaluate the height-resolved and height-integrated transfer of electromagnetic energy between the high-latitude ionosphere and magnetosphere. This will allow the altitude distribution of the electromagnetic energy flux, q, and the total flux into or out of the ionosphere to be determined directly. In addition, the redistribution of this energy flux in the ionosphere can be evaluated from the radar measurements by determining the height-resolved Joule heating rate, q_j, and mechanical energy transfer rate, q_m.

3 SCIENTIFIC REPORTS

A paper describing the technique and giving examples of Poynting flux measurements from DE-2 has been published: J..B. Gary, R.A. Heelis, W.B. Hanson, and J.A. Slavin, "Field-aligned Poynting flux observations in the high-latitude ionosphere," *J. Geophys. Res.*, 87, 11417-11427, 1994. (See Appendix A.)

A paper describing the numerical results for the modeling study of the Poynting flux has been published: J.P. Thayer, J.F. Vickrey, R.A. Heelis, J.B. Gary, "Interpretation and modeling of the high-latitude electromagnetic energy flux," *J. Geophys. Res.*, 100, 19715-19728, 1995. (See Appendix B.)

A paper describing the distribution of the Poynting flux measurements from DE-2 has been published: J.B. Gary, R.A. Heelis, and J.P. Thayer, "Summary of field-aligned Poynting flux observations from DE 2," *Geophys. Res. Lett*, 22, 1861-1864, 1995. (See Appendix C.)

A paper describing the influence of the neutral winds on estimates of the height-resolved Joule heating rate from the Sondrestrom incoherent-scatter radar has been submitted to the *Journal of Geophysical Research*: "Height-resolved Joule heating rates in the high-latitude E region and the influence of neutral winds," by J.P. Thayer. (See Appendix D.)

A paper describing the estimation of the height-resolved and height-integrated electromagnetic transfer rate at high latitudes by the Sondrestrom incoherent-scatter radar is in preparation for submission to the *Journal of Geophysical Research*: "Evaluation of electromagnetic energy transfer in the high-latitude E-region as determined by the Sondrestrom incoherent-scatter radar," by J.P. Thayer.

4 REFERENCES

Cowley, S.W.H., "Acceleration and heating of space plasmas: Basic concepts," *Ann. Geophys.*, *9*, 176–187, 1991.

Kelley, M.C., D.J. Knudsen, and J.F. Vickrey, "Poynting flux measurements on a satellite: A diagnostic tool for space research," *J. Geophys. Res.*, *96*, A1, 201–207, 1991.

Thayer, J.P., and J.F. Vickrey, "On the contribution of the thermospheric neutral wind to high-latitude energetics," *Geophys. Res. Lett.*, *19*, 3, 265-268, 1992.

APPENDIX A

Gary, J.B., R.A. Heelis, W.B. Hanson, and J.A. Slavin, "Field-aligned Poynting flux observations in the high-latitude ionosphere," *J. Geophys. Res.*, 87, 11417-11427, 1994.

JOURNAL OF GEOPHYSICAL RESEARCH, VOL. 99, NO. A6, PAGES 11,417–11,427, JUNE 1, 1994

Field-aligned Poynting flux observations in the high-latitude ionosphere

J. B. Gary, R. A. Heelis, and W. B. Hanson
Center for Space Sciences, Physics Programs, University of Texas at Dallas, Richardson

J. A. Slavin
Laboratory for Extraterrestrial Physics, NASA Goddard Space Flight Center, Greenbelt, Maryland

Abstract. We have used data from Dynamics Explorer 2 to investigate the rate of conversion of electromagnetic energy into both thermal and bulk flow particle kinetic energy in the high-latitude ionosphere. The flux tube integrated conversion rate $\mathbf{E}\cdot\mathbf{J}$ can be determined from spacecraft measurements of the electric and magnetic field vectors by deriving the field-aligned Poynting flux, $S_{||}=\mathbf{S}\cdot\hat{B}_o$, where $\hat{B}_o$ is in the direction of the geomagnetic field. Determination of the Poynting flux from satellite observations is critically dependent upon the establishment of accurate values of the fields and is especially sensitive to errors in the baseline (unperturbed) geomagnetic field. We discuss our treatment of the data in some detail, particularly in regard to systematically correcting the measured magnetic field to account for attitude changes and model deficiencies. $S_{||}$ can be used to identify the relative strengths of the magnetosphere and thermospheric winds as energy drivers and we present observations demonstrating the dominance of each of these. Dominance of the magnetospheric driver is indicated by $S_{||}$ directed into the ionosphere. Electromagnetic energy is delivered to and dissipated within the region. Dominance of the neutral wind requires that the conductivity weighted neutral wind speed in the direction of the ion drift be larger than the ion drift, resulting in observations of an upward directed Poynting flux. Electromagnetic energy is generated within the ionospheric region in this case. We also present observations of a case where the neutral atmosphere motion may be reaching a state of sustained bulk flow velocity as evidenced by very small Poynting flux in the presence of large electric fields.

Introduction

The study of coupling processes between the Earth's magnetosphere and ionosphere is frequently aided by an examination of the energy flow between these regions. Poynting vectors determined from in situ electric and magnetic field measurements have been frequently used in the study of magnetospheric wave phenomena associated with micropulsations of the magnetic field. *Cummings et al.* [1978] performed such an analysis using ATS 6 data from geosynchronous orbit to establish the presence of standing hydromagnetic waves along the magnetic field. *Mauk and McPherron* [1980], again with ATS 6 data, used calculated Poynting vectors in their analysis of possible Alfven/ion cyclotron waves originating in the equatorial magnetosphere. More recently, *Erlandson et al.* [1990], *LaBelle and Truemann* [1992], and *Fraser et al.* [1992] calculated Poynting vectors from satellite data to establish the presence of electromagnetic ion cyclotron waves similar to those discussed by Mauk and McPherron [1980].

The use of Poynting flux determined from satellite measurements in an analysis of very large scale, high-latitude ionospheric activity was first proposed by *Knudsen* [1990] and shortly thereafter by *Kelley et al.* [1991]. These authors described in some detail the application of global Poynting flux determination from in situ measurements to the geophysical system comprised of the coupled magnetosphere and ionosphere. Using the principle of conservation of electromagnetic energy (Poynting's theorem), they demonstrated the possibility of determining the rate of energy conversion taking place in a volume extending from the satellite orbit down to the base of the ionosphere by examining the vertical component of the Poynting vector. The energy conversion rate $\mathbf{E}\cdot\mathbf{J}$ is related to the Joule heating rate of the plasma and the rate of momentum transfer between the ions and the neutral gas in the lower ionosphere. They also included results of such an analysis

Paper number 93JA03167.
0148-0227/94/93JA-03167$05.00

using data from the HILAT satellite at 800 km altitude. Our approach to the technique is similar to theirs with the exceptions that the volume to which Poynting's theorem is applied is a single flux tube in our case and we determine the field-aligned component of the Poynting vector rather than approximate it using the vertical component. We refer the reader to the Appendix of *Kelley et al.* [1991] for further details. The major assumption in applying Poynting's theorem to determine the rate of electromagnetic energy conversion using in situ measurements is the assumption that steady state conditions prevail. This ignores possible contributions from wave phenomena which are likely to be present in the high latitude ionosphere but which are likely to present a signature at DE 2 altitudes below the minimum scale size that we are considering in the present work (tens of kilometers).

The electric fields and currents which link the magnetosphere and ionosphere are generated by the dynamo action of plasma flowing through the ambient magnetic field. Electromagnetic energy in the high latitude ionosphere can come from two sources, one originating from the interaction of the solar wind and magnetosphere and the other originating in the ionosphere. The magnetospheric source can be considered as a dynamo directly connected to the polar cap at the highest magnetic latitudes which, under most conditions in the ionosphere, magnetosphere, and solar wind, will drive energy into the lower regions of the earth's atmosphere where the circuit is closed through the ionosphere. In these circumstances, the ionosphere acts as a resistive load to the magnetospheric generator, although it is not a passive resistive element in this circuit. The effect of the ionosphere on the global circuit is determined by the ionospheric conductivity and on the behavior of the neutral wind. Electromagnetic energy can also be produced within the high latitude ionosphere via the action of a neutral wind dynamo, principally in the E region. In this region the neutral atmosphere motion may be driven by solar heating but, more importantly, energy is "stored" in the neutral atmosphere at lower ionospheric altitudes through frictional coupling between the magnetosphere-driven plasma and the neutral gas in which it is embedded. Electric fields mapped from the magnetosphere impose a circulation pattern on the ions in the ionosphere. During prolonged times of strong interplanetary magnetic field (IMF) conditions, this circulation is transferred to the neutrals through collisions. If the IMF then changes its orientation, say from southward to northward, then the ions can be driven by electric fields in a different direction from that in which the neutrals are moving. The resulting ion motion will then be determined by the relative strengths of the newly established electric fields from the magnetosphere and the inertial and viscous effects of the neutral wind. If the electric field in the frame of reference of the neutral particles is small, then the ions may be driven by the neutral wind dynamo along the previously established convection pattern. Conceptually, these are the anticipated circumstances under which an upward directed Poynting flux may be observed in a reference frame corotating with the Earth.

The initial motivations behind an effort to calculate the large scale Poynting vector in the Earth's ionosphere have been to provide observations of the action of a neutral wind dynamo. *Lyons et al.* [1985] proposed a neutral wind dynamo as a current source in the polar cap during times of stagnant ion convection. Modeling efforts of neutral wind phenomenon have been carried out recently by *Deng et al* [1991] and by *Thayer and Vickrey* [1992]. These efforts have suggested the existence of regions of outward directed electromagnetic energy flux in the polar cap. *Fejer* [1983] also described a neutral wind dynamo effect, termed a disturbance dynamo, as an electric field driver at sub-auroral latitudes following the onset of geomagnetic storms. The dominance of these dynamos would be readily identifiable with field-aligned Poynting flux observations of sufficient accuracy.

Measurements from DE 2

A measurement of the Poynting vector is critically dependent on accurate measurements of the electric field and the magnetic field perturbation vectors. Accordingly, the bulk of the technical work involved in this research involves an analysis of the absolute magnitudes of the measured quantities, as well as their uncertainties, and the development of suitable techniques to render accurate calculations of the Poynting vector over the widest possible range of acquired DE 2 data.

We have taken some care to provide the highest quality derivation of the drift velocities. This is particularly important in the derivation of the ion drift velocity along the spacecraft x axis (ram) which involves a least squares analysis of the ion energy distribution measured by the retarding potential analyzer (RPA). A planar retarding potential analyzer was flown on DE 2 and this instrument is described in detail by *Hanson et al.* [1981]. Substantial variations in the spacecraft potential, $\phi_{s/c}$, are known to occur, for example, as the vehicle traverses regions of elevated electron temperature, which affect the derived ion velocities in a manner not generally compensated for in the RPA analysis [Anderson *et al*, 1994]. Changes in $\phi_{s/c}$ can alter the baseline values for the ram drift by 100 m/s or more, and we have modified the RPA analysis to account for these changes.

The components of the ion drift velocity perpendicular to the direction of the spacecraft velocity vector were measured using an ion drift meter, described by *Heelis et al.* [1981]. This measurement is also sensitive to $\phi_{s/c}$, although less so than the RPA, and changes in the ion arrival angle produced by a changing spacecraft potential are taken into account in determining the ion drift velocity vector. The ion drifts are then used to calculate the electric field under the assumption that $\mathbf{E} = -\mathbf{V} \times \mathbf{B}$. Comparisons between the values of the electric field measured directly by the Vector Electric Field Instrument and those derived from the ion drift

have shown generally very good agreement [Hanson *et al.*,1993].

Magnetic field measurements from DE 2 were made using a triaxial flux gate magnetometer, which has been described in detail by *Farthing et al.* [1981]. For determination of the Poynting vector, it is the perturbation magnetic field vector produced by currents in the system that must be known. The perturbation magnetic field $\delta\mathbf{B}$ is defined as the difference between the measured ambient magnetic field $\mathbf{B}$ and a vector spherical harmonic model of the Earth's unperturbed field $\mathbf{B}_O$ which incorporates satellite measurements from the MAGSAT magnetic field mapping mission [*Langle and Estes*, 1985]: $\delta\mathbf{B} = \mathbf{B}\text{-}\mathbf{B}_o$. The determination of accurate perturbation magnetic field vectors is the major procedural obstacle to methodically establishing the Poynting vector from satellite data. This difficulty is mostly a reflection of the uncertainty in our knowledge of the actual spacecraft attitude, that is, its orientation relative to the unperturbed field $\mathbf{B}_O$. Efforts to reduce this error have been made by many spacecraft magnetometer investigators in the past, and their approaches have ranged from estimating the attitude error using complicated functions involving spacecraft attitude and position [e.g., *McDiarmid et al.*, 1978] to simple endpoint matching [e.g., *Doyle et al.* [1981].

The magnitude of the attitude error between that derived from the spacecraft horizon sensors and the magnetometer may be several tenths of a degree and variable over the course of a polar pass. For this reason, it is not unusual for the perturbation magnetic fields to be biased by several hundred nanoTesla due to these attitude errors. Compensations for these errors can be made if it is assumed that (1) the total attitude error changes slowly over a polar pass, and (2) the natural perturbation magnetic field below about 50 deg invariant latitude is small. The first assumption generally appears to be true in that while a single attitude correction made at the beginning of a polar pass is not sufficient to "level" the magnetic field base line at the end of the pass, the error appears to grow steadily over the course of the pass. The second assumption also appears to be reasonable in that the sum of the magnetic fields associated with the magnetopause currents, the tail current systems and the Sq currents should not be any larger than several tens of nanoTesla at mid-latitudes. We therefore determine a new base line for the magnetic field perturbations by fitting a cubic spline to the magnetometer output with four anchor points located at invariant latitudes sufficiently below the auroral oval to escape influences from field-aligned currents on both the entering and departing sections of the high-latitude pass. This curve is now assumed to be a realistic base line for the intrinsic magnetic field, since it takes into account possible inaccuracies in both spacecraft orientation and in the model field. We typically choose the anchor points as near to 40 deg invariant latitude as the data allows. The difference between the measured field and the spline fit in these regions is less than 50 nT, and we have no reason to expect this uncertainty to increase in the high latitude region where the Poynting flux is being determined.

In assessing the total uncertainty in our results, we must examine the combined effect of our uncertainties in determining the magnetic and electric fields. If we denote the uncertainty in the perturbation magnetic field as β and the uncertainty in the electric field as ϵ, then the true (as opposed to measured) Poynting vector can be written as

$$\mathbf{S}_{\mathbf{True}} = \frac{1}{\mu}(\mathbf{E} \pm \epsilon) \times (\delta\mathbf{B} \pm \beta). \qquad (1)$$

Combining all terms containing ϵ and β we can arrive at the following estimate for the maximum uncertainty in the magnitude of $\mathbf{S}_{True}$ (ΔS) :

$$\Delta S = \frac{1}{\mu}(E\beta \pm \delta B\epsilon \pm \beta\epsilon). \qquad (2)$$

Our uncertainty in the field-aligned Poynting flux depends not only on the product of the uncertainties ϵ and β but on their product with E and δB as well. In order to gain some intuition as to the relative size of the uncertainty, we can take the ratio of ΔS to our calculated value of $\mathbf{S} = \frac{1}{\mu}(\mathbf{E} \times \delta\mathbf{B})$:

$$\frac{\Delta S}{S} = \pm\frac{\beta}{\delta B} \pm \frac{\epsilon}{E} \pm \frac{\epsilon\beta}{E\delta B}. \qquad (3)$$

For the perturbation magnetic field, we estimate 50 nT to be the maximum cumulative uncertainty, while for the electric field we take 2 mV/m to be the cumulative uncertainty. The sensitivity of the Poynting flux to the measured data is immediately apparent, especially to the determination of the perturbation magnetic field, and allows us to place confidence bounds on our analysis. As an illustration, a calculated Poynting flux of

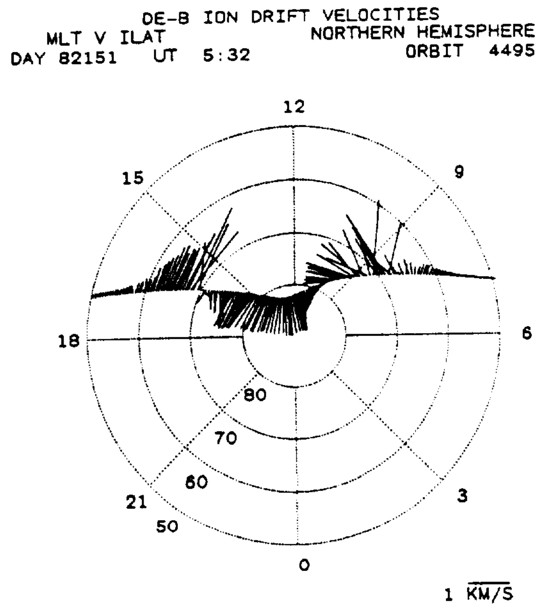

Figure 1. Polar plot of horizontal ion drift velocities for orbit 4495.

1 mW/m^2 corresponding to $\delta B = 200$ nT and $E = 6.3$ mV/m gives $\frac{\Delta S}{S} \sim 0.60$, that is, a possible error of 60 percent, whereas typical auroral zone values of $S \sim 20$ mW/m^2 with $\delta B = 500$ nT and $E = 50$ mV/m lead to an uncertainty of about 14 percent.

Data Analysis

We have selected six high latitude passes of Dynamics Explorer 2 to illustrate the variation in the large scale Poynting flux along the spacecraft track and the role that this parameter may play in revealing the conditions under which energy exchange between the ionosphere and the magnetosphere can be drastically different. The chosen passes lie approximately along the dawn-dusk meridian. We have chosen a coordinate system in which the positive x direction is always along the spacecraft velocity vector (ram direction or meridional), positive y is always upward (out of the ionosphere), z makes up the remaining (zonal) component of the right-handed system. For each orbit we present the magnetometer data used in the calculations before and after the base line alterations, together with the spline curve taken as the new base line. The field-aligned Poynting flux is shown together with the horizontal ion drift velocities.

Poynting's theorem for steady state conditions applied to a single flux tube bounded by the satellite at top and the base of the ionosphere at bottom reads

$$\int \mathbf{S}_{\parallel} \cdot \hat{n} da = -\int \mathbf{E} \cdot \mathbf{J} dV, \qquad (4)$$

which relates the surface integral of the field-aligned

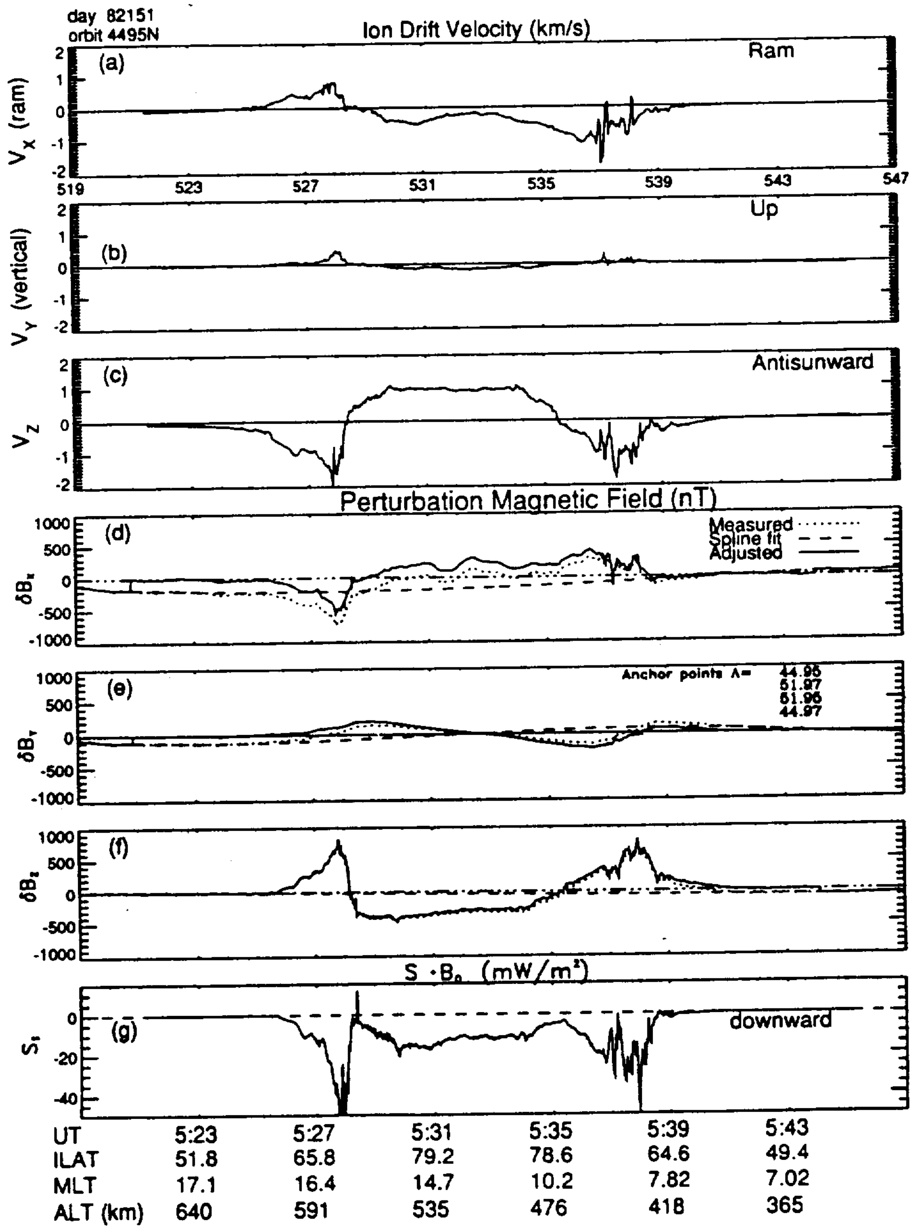

Figure 2. Ion drift velocity components for orbit 4495 : (a) ram, (b) vertical, and (c) cross-track; (d-f) perturbation magnetic field components as measured and after spline fit; and (g) field-aligned Poynting flux $S_{\parallel} = \mathbf{S} \cdot \hat{\mathbf{B}}_O$. All quantities are in spacecraft coordinates.

Poynting flux $\mathbf{S}_\parallel$ across the boundary to the energy conversion rate within the volume. With $\hat{n}$ pointing outward everywhere, and assuming that no energy flows out the bottom of the region, a measurement of $\mathbf{S}_\parallel$ at the top of the region is equal to minus the rate of energy conversion below [*Kelley, et al.*, 1991].

The right-hand side of (4) can be written [e.g., *Thayer and Vickrey*, 1992] as

$$\int \mathbf{E} \cdot \mathbf{J} dV = \int \mathbf{E}' \cdot \mathbf{J} + \mathbf{U} \cdot (\mathbf{J} \times \mathbf{B}) dV, \qquad (5)$$

where $\mathbf{E}'$ is the electric field in the frame of the neutrals and is related to the measured electric field $\mathbf{E}$ by the transformation $\mathbf{E}' = \mathbf{E} + \mathbf{U} \times \mathbf{B}$. This equation may be further examined by decomposing the current density $\mathbf{J}$ into Hall and Pedersen components, after which (5) becomes

$$\int \mathbf{E} \cdot \mathbf{J} dV = \int [\sigma_P \mathbf{E}'^2 - \sigma_P \mathbf{U} \cdot (\mathbf{E}' \times \mathbf{B}) + \sigma_H B \mathbf{U} \cdot \mathbf{E}'] dV. \qquad (6)$$

Equation (6) makes explicit the interplay between the electric field $\mathbf{E}'$ typically originating in the magnetosphere and the neutral wind velocity $\mathbf{U}$, as well as the weighting of the energy conversion rate by the conductivities. It is interesting that there is a term weighted by the Hall conductivity, a fact often neglected in assessments of $\mathbf{E} \cdot \mathbf{J}$.

The first term in (6) gives the contribution to the energy conversion rate from frictional heating between the ions and the neutrals, leading to elevated temperatures from increased thermal motion. This may also be termed the Joule heating rate or Joule dissipation rate, although there is a certain lack of consistency in the widespread usage of these terms. The second and third terms in (6) describe the rate of change of kinetic energy of the neutral gas due to collisions with the ions.

Given that our assessment of the field-aligned Poynting flux is correct, we see that there must be three general cases of interest in looking at the data: $\mathrm{S}_\parallel < 0$ (into the ionosphere, ionospheric load), $\mathrm{S}_\parallel > 0$ (out of the ionosphere, ionospheric generator), and $\mathrm{S}_\parallel = 0$ (no net energy conversion). Equation (6) demonstrates the requirements for these conditions, and we see that the direction of the field-aligned Poynting flux is principally dependent upon the relative orientations of $\mathbf{U}$ and $\mathbf{E}'$. Observationally, we take the ion drift velocity $\mathbf{V}$ to be indicative of the overall nature of $\mathbf{E}'$ since, in the F region where our measurements are made, $\mathbf{E}' = (\mathbf{U}-\mathbf{V}) \times \mathbf{B}$. While we are unable to discriminate between the effects of the individual terms in (6), we can make some statements from the more general equation (5). Whenever the height-integrated quantity $\mathbf{U} \cdot (\mathbf{J} \times \mathbf{B})$ is positive, the entire quantity $\mathbf{E} \cdot \mathbf{J}$ is positive and electromagnetic energy is being converted into particle thermal and kinetic energy within the volume. Electromagnetic energy generation within the volume requires that $\mathbf{U}$ oppose the $\mathbf{J} \times \mathbf{B}$ force and that the flux tube-integrated magnitude of $\mathbf{U} \cdot (\mathbf{J} \times \mathbf{B})$ be greater than that of $\mathbf{E}' \cdot \mathbf{J}$ ($=\Sigma_P \mathrm{E}'^2$), signifying the dominance of the neutral wind over the magnetosphere as the driver of the energy flow. The conditions for $\mathrm{S}_\parallel < 0$ are perhaps best exemplified during times of southward IMF where a well defined two-cell convection pattern generally forms in the ionosphere. The large scale electric field is generally imposed from the magnetosphere as indicated by the organized ion drifts. We can expect $\mathrm{S}_\parallel < 0$ in the polar cap, where both $\mathbf{V}$ and $\mathbf{U}$ are generally antisunward with $V > U$, and in the auroral zone where $\mathbf{V}$ and $\mathbf{U}$ are oppositely directed. We present two cases which are typical of these conditions and in which the sunward and antisunward ion drift velocities exceed 1 km/s, much larger than we would expect neutral wind velocities to be.

The first case presented is orbit 4495 from May 31, 1982. The satellite passes through the dayside northern high latitude summer ionosphere, moving from dusk to dawn at altitudes descending from 640 to 365 km. The ion drift velocities, seen in the polar dial of Figure 1 and as separate components in Figures 2a-2c, show a characteristic two-cell convection pattern associated with a steady southward IMF, suggesting that the magnetosphere is in firm control of the circulation in the ionosphere. Hourly averaged values of the IMF indicate that the IMF was in fact steady, although not strongly, southward during this time.

Figures 2d-2f show the three components of the magnetic field perturbation measured from DE 2 together with the corrected perturbations obtained by establishing a new base line for the measurement. The originally measured perturbations are indicated by the dotted curve. It can be seen that substantial perturbations exist at invariant latitudes below 50° where we would expect such perturbations to be small. The dashed curve shows the cubic spline base line determined by requiring the perturbation to be zero at 45° and 52°

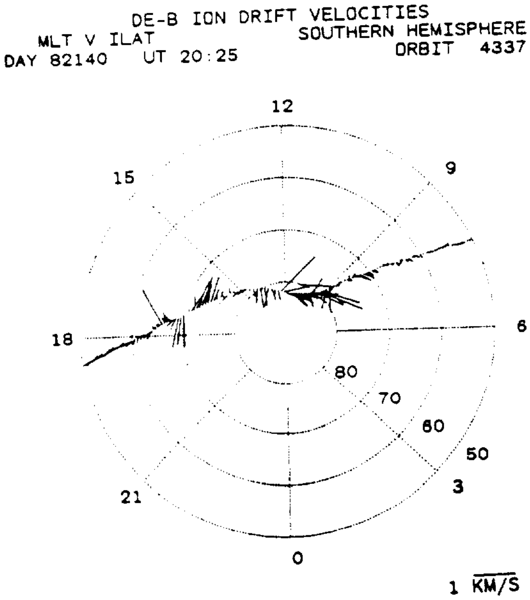

Figure 3. Polar plot of horizontal ion drift velocities for orbit 4337.

invariant latitude. The resulting magnetic field perturbations used in the calculation of the Poynting flux are shown by the solid curve. The result of this correction procedure has the most pronounced effect on $\delta\mathbf{B}_X$ with a maximum difference between corrected and uncorrected values of about 200 nT. Notice, however, that this correction procedure essentially preserves the gradients in $\delta\mathbf{B}$ from which field-aligned currents (FAC) would be determined. The presence of region 1 and region 2 FAC can be clearly seen in the horizontal components of the perturbation magnetic field, especially $\delta\mathbf{B}_z$ (figure 2f). The satellite passed between the large scale current sheet on the duskside at roughly 0527 UT, with the region 1 current associated with the δ B gradients just poleward and the region 2 current sheet associated with the equatorward gradient [e.g.,*Zanetti et al.*, 1983]. On the dawnside, the region 1 current was apparently spread over a larger extent as indicated by the smaller gradient, and is more structured than on the dusk side. The high degree of correlation between the horizontal components of the magnetic field perturbation $\delta\mathbf{B}_X$ and $\delta\mathbf{B}_z$ suggest that the spacecraft is passing through an "infinite" field-aligned current sheet at the dusk side convection reversal. The quasi-sinusoidal signature evident in the vertical component ($\delta\mathbf{B}_Y$) is indicative of the effect of the distant auroral electrojet [*Zanetti et al.*, 1983]. The cross-track components of $\mathbf{V}$ and $\delta\mathbf{B}$ have a correlation coefficient of 0.93 across the entire pass. This would be expected if the height-integrated Pedersen conductivity was uniform [*Sugiura et al.*, 1982], and for these data the E region below was sunlit.

As can be seen in Figure 2c, the horizontal ion drift across the polar cap is largely antisunward and of sufficient magnitude for us to conjecture that $|\mathbf{V}| > |\mathbf{U}|$ and that the electric field is primarily magnetospheric, consistent with our expectations for downward Poynting

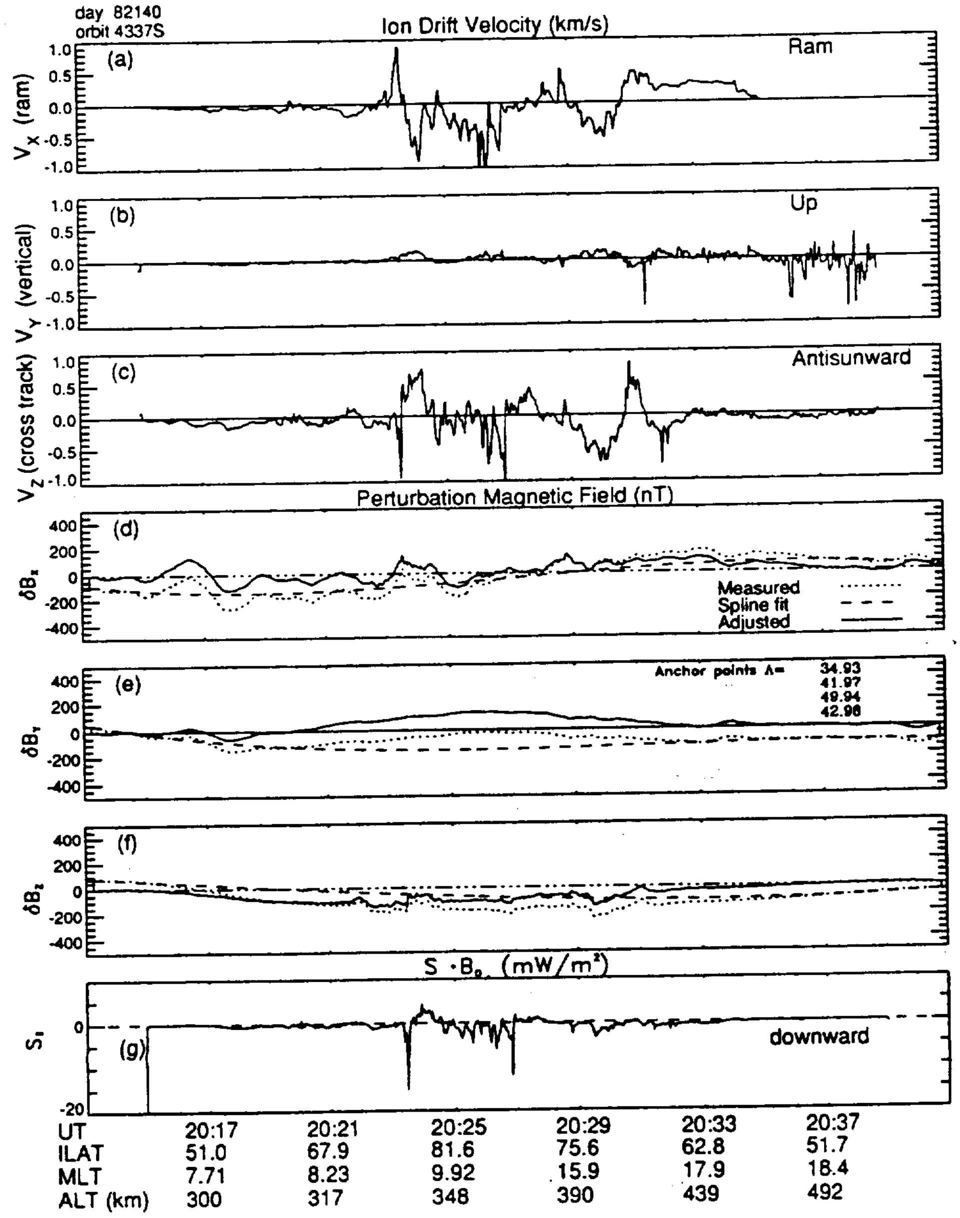

Figure 4. Data for orbit 4337 in the same format as Figure 2.

flux in the polar cap. In the auroral zone, the drift velocities are large and sunward. The observed Poynting flux is downward along the entire pass across the polar cap, averaging 6.29 mW/m^2 over the pass, with maximum values in the auroral zones of about 82 mW/m^2 on the dusk side and 40 mW/m^2 on the dawn side. This asymmetry is in accordance with the findings of *Foster et al.* [1983] and *Vickrey et al.* [1982] on the local time variation of Joule heating rates. The distribution of the field-aligned Poynting flux across the polar cap, from about 0528 UT to 0536 UT, supports the idea that appreciable region 1 current closes across the polar cap with resulting Joule dissipation and momentum transfer in the region of the lower ionosphere. This is consistent with previous interpretations of the horizontal perturbation magnetic field signature across the polar cap, with the antisunward/tailward extension of δB_z in that section of the pass indicating region 1 current closure across the polar cap [e.g., *McDiarmid et al.*, 1978]

As we have mentioned, the case of upward, or outward, Poynting flux is indicative of a neutral wind dynamo process. The criterion for a neutral wind dynamo is most likely to be satisfied during times of northward IMF when the ions are not being strongly driven by electric fields from the magnetosphere. It is also possible for there to be small regions of upward Poynting flux during southward IMF near the reversal boundaries where the ion drifts become comparable to the neutral wind velocities.

We now present a case for which the conditions necessary for upward Poynting flux are apparently met. Orbit 4337, day 82140, passed across the dayside southern winter ionosphere at an altitude of about 300 km roughly from dawn to dusk. The IMF was steadily northward for several hours preceding the pass with an hourly averaged B_z of 1.4 nT for the time of the orbit. Figure 3 and Figures 4a-4c show the structured ion drifts typical of northward IMF, winter conditions, and the perturbation magnetic field signatures seen in Figures 4d-4f do not indicate the presence of large scale field-aligned currents. The electrodynamic coupling between the magnetosphere and ionosphere is far weaker in this instance, having no well-defined convection patterns or large field-aligned current systems. The plot of $S_{\|}$ (Figure 4g) reveals two relatively large scale regions as well as a few isolated locations where the Poynting flux is directed upward. The regions of upward Poynting flux are well correlated with regions of antisunward ion drift velocities, as we expect from our earlier arguments. The largest region of upward $S_{\|}$, between 2023 and 2024 UT, spans 427 km along the satellite track with a peak value of 3.6 mW/m^2 and an average value of 1.54 mW/m^2. The second region, between 2027 and 2028 UT, represents a smaller energy conversion rate, with a maximum value across the 480 km stretch being only 1.55 mW/m^2 and an average value of only 0.57 mW/m^2. This weaker region marks the extreme edge of confidence in our ability to determine the field-aligned Poynting flux from DE 2 measurements with the cor-

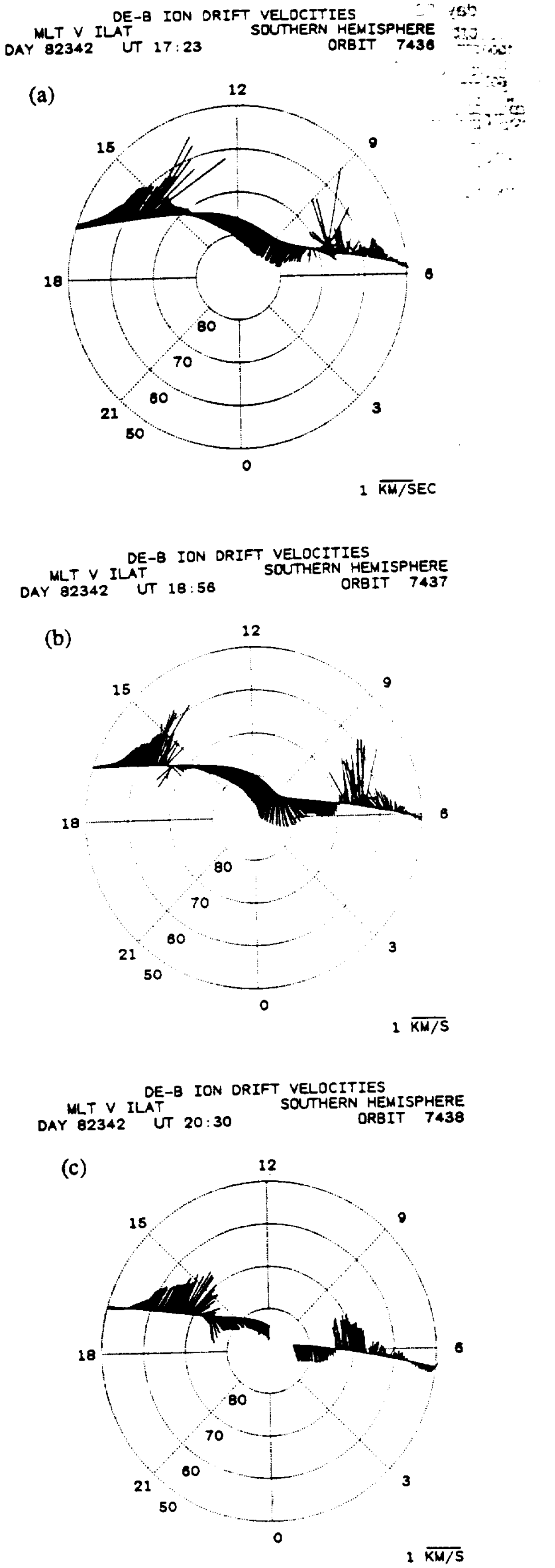

Figure 5. Polar plots of the horizontal ion drift velocities for orbits (a) 7436, (b) 7437, and (c) 7438.

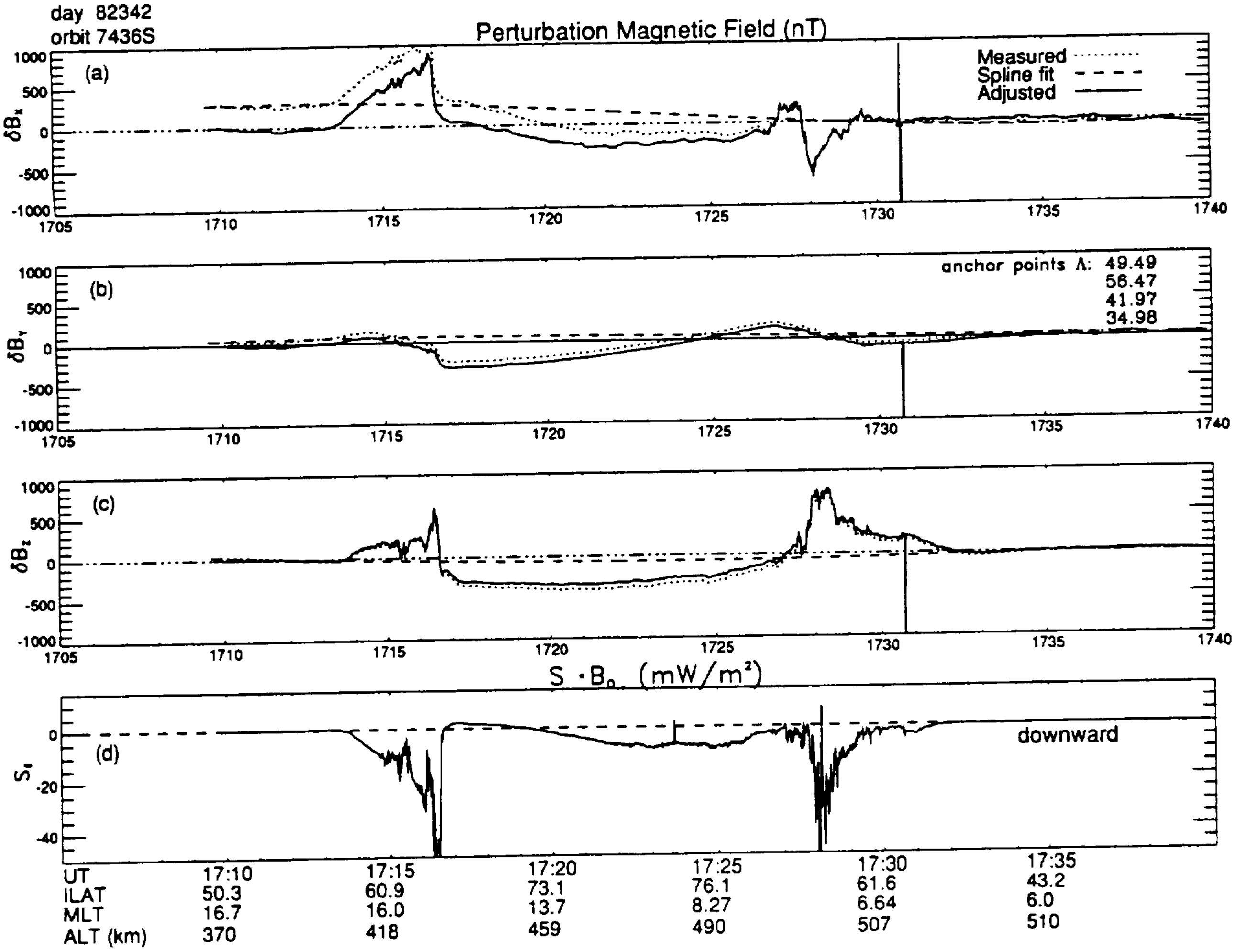

Figure 6. Perturbation magnetic field components in spacecraft coordinates and field-aligned Poynting flux for orbit 7436: (a) δB_x or ram, (b) δB_y or vertical, (c) δB_z or cross track, and (d) $S_\parallel$.

rection procedures we have described, with an average uncertainty determined from (1) of 55 percent.

The condition under which $S_\parallel$ may equal 0, implying that no net energy conversion is taking place in the flux tube volume, is for $\mathbf{E}'\cdot\mathbf{J} = -\mathbf{U}\cdot(\mathbf{J}\times\mathbf{B})$. $S_\parallel$ will also equal zero if the ion drift, and hence electric field, is zero. Note that this may be achieved by changing coordinates to a system that is moving with the ions, so that the Poynting flux is dependent on the choice of coordinate system. In the frame co-rotating with the Earth, however, this condition is unlikely to be met under steady state conditions in that while the electric field may change sign over a very short spatial scale, as in a shear reversal, there is no point where the ions are actually stationary. In general, $S_\parallel = 0$ indicates that the rate of frictional heating of the ions is balanced by the rate of bulk flow kinetic energy transfer between the ions and the neutrals due to collisions. This condition may mark the establishment of a sustained neutral wind "flywheel", where the neutral particles have been accelerated by the ions until they are moving at comparable speeds, thus in some sense storing the energy until the bulk ion flow changes in response to varying electrodynamic conditions. Observation of the development of such a situation requires consecutive data sets during a time of stable conditions.

The orbits shown in the polar dials of Figure 5 represent a sequence of three southern hemisphere summer dayside passes, all on day 82342 between 1700 UT and 2100 UT. The spacecraft measurements shown lie entirely in daylight and the conductivities in the polar cap ionosphere are dominated by ionization produced by solar UV radiation. Under these conditions, we may assume that the principal differences between orbits in the sequence are attributable to variations in the electromagnetic energy driver rather than in the conductivity of the ionosphere, at least on the global scale which we are considering here. Therefore changes in the ionospheric energy conversion rate are more a reflection of changes in IMF conditions and in the motion of the neutral wind.

The IMF was strongly southward for at least two hours before the beginning of the sequence and continued to be so until around 2000 UT. Hourly averages for B_z during this interval range from -7.4 to -10.0 nT, after which B_z began to swing northward. The hourly average for B_z during the third orbit was near zero, and reached 3.6 nT in the following hour. The ion drift

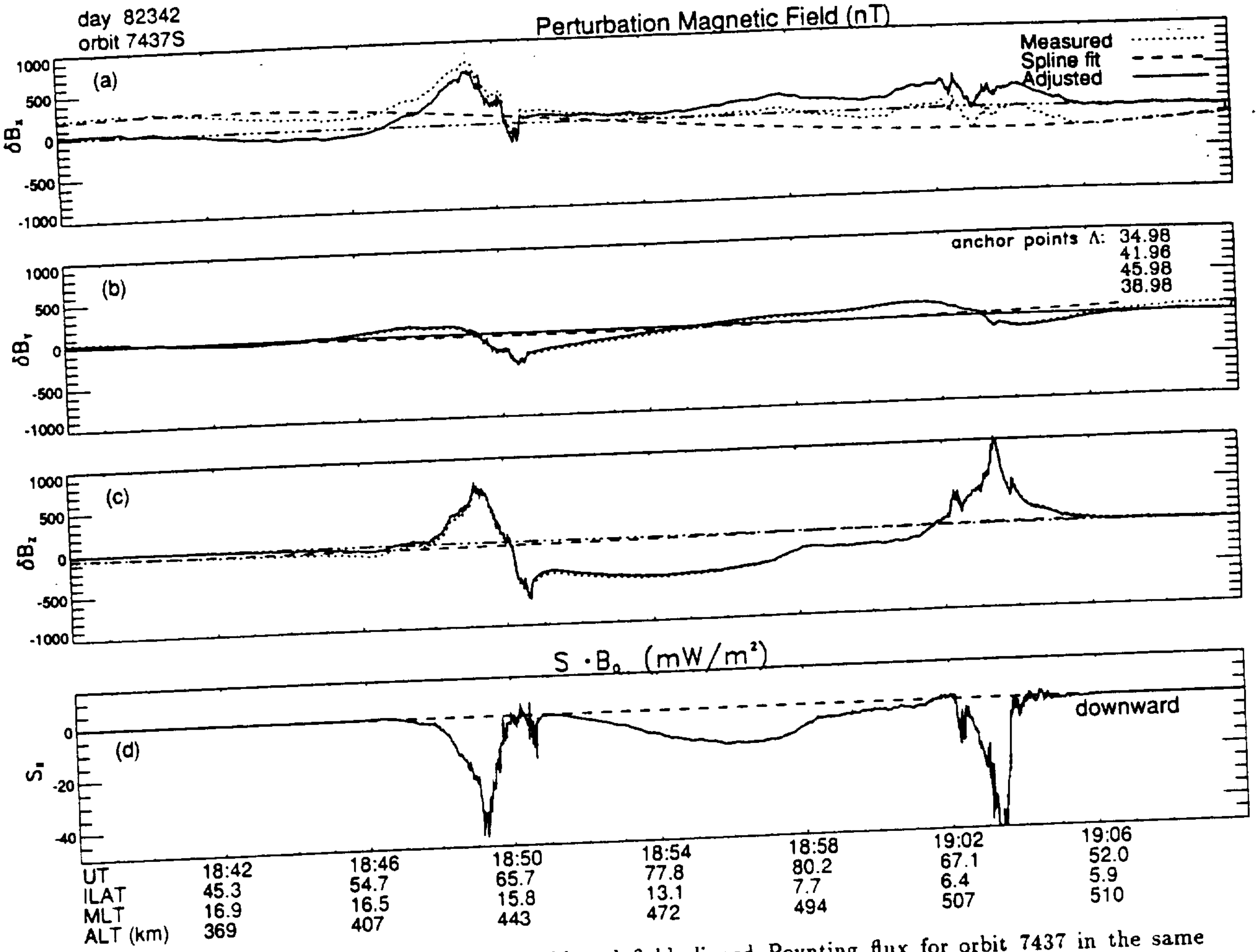

Figure 7. Perturbation magnetic field and field-aligned Poynting flux for orbit 7437 in the same format as Figure 6.

velocities in all three cases suggest a strong two-cell convection pattern, with the drifts increasing from the first orbit to the second and then decreasing between the second and final orbits. In all three orbits, the perturbation magnetic field signature contains well defined region 1 and region 2 field-aligned currents. The field-aligned Poynting flux in each case is almost everywhere directed into the ionosphere and is of smaller magnitude in the polar cap than in the auroral zones.

For the first orbit in the sequence, orbit 7436, $S_{\parallel}$ across the polar cap is dominantly downward and has an average value of 3.7 mW/m^2. There is a region of upward Poynting flux poleward of the duskside convection reversal boundary, as seen in figure 6d, centered near 1715 UT. The average value for $S_{\parallel}$ across this region is 1.4 mW/m^2, and it spans about 1050 km along the satellite track. Orbit 7437 took place near the conclusion of the period of strongly southward B_z, and it can be seen in the polar plot (figure 5b) that there is a substantial increase in ion drift velocity from the previous orbit, implying that the ions are being more strongly driven by the magnetosphere. The observed values for $S_{\parallel}$ across the polar cap are consistent with this interpretation, with an average value of 8.7 mW/m^2. The region 1 and region 2 current signatures in $\delta\mathbf{B}$ seen in Figures 7a-7c in this case are consistent with substantial field-aligned current closing across the polar cap, as evidenced by the very sharp gradient in $\delta\mathbf{B}_z$ on the duskside.

In the final orbit, 7438, the ion drifts have slowed (Figure 5c) and $S_{\parallel}$ across the polar cap has an average value of only 1.37 mW/m^2. Comparison with the plots of $S_{\parallel}$ for the three orbits (Figures 6c, 7c and 8c) clearly demonstrates the marked decrease in the energy conversion rate. This observation, combined with the decrease in B_z to near zero, leads us to conclude that the ions and neutrals must be moving at very nearly the same speed, representing an "undriven" ionosphere in the polar cap. Examination of the $\delta\mathbf{B}$ signature suggests that the large scale field-aligned currents have greatly diminished in magnitude from the previous orbit, and that much of the region 1 current could be closing through the neighboring region 2 current rather than across the polar cap as indicated by the small values of $S_{\parallel}$.

Conclusions

We have undertaken an examination of the electromagnetic energy conversion rate in the earth's ionosphere by determination of the Poynting vector at points along the trajectory of a polar orbiting satellite. In so doing, we have presented a systematic approach to es-

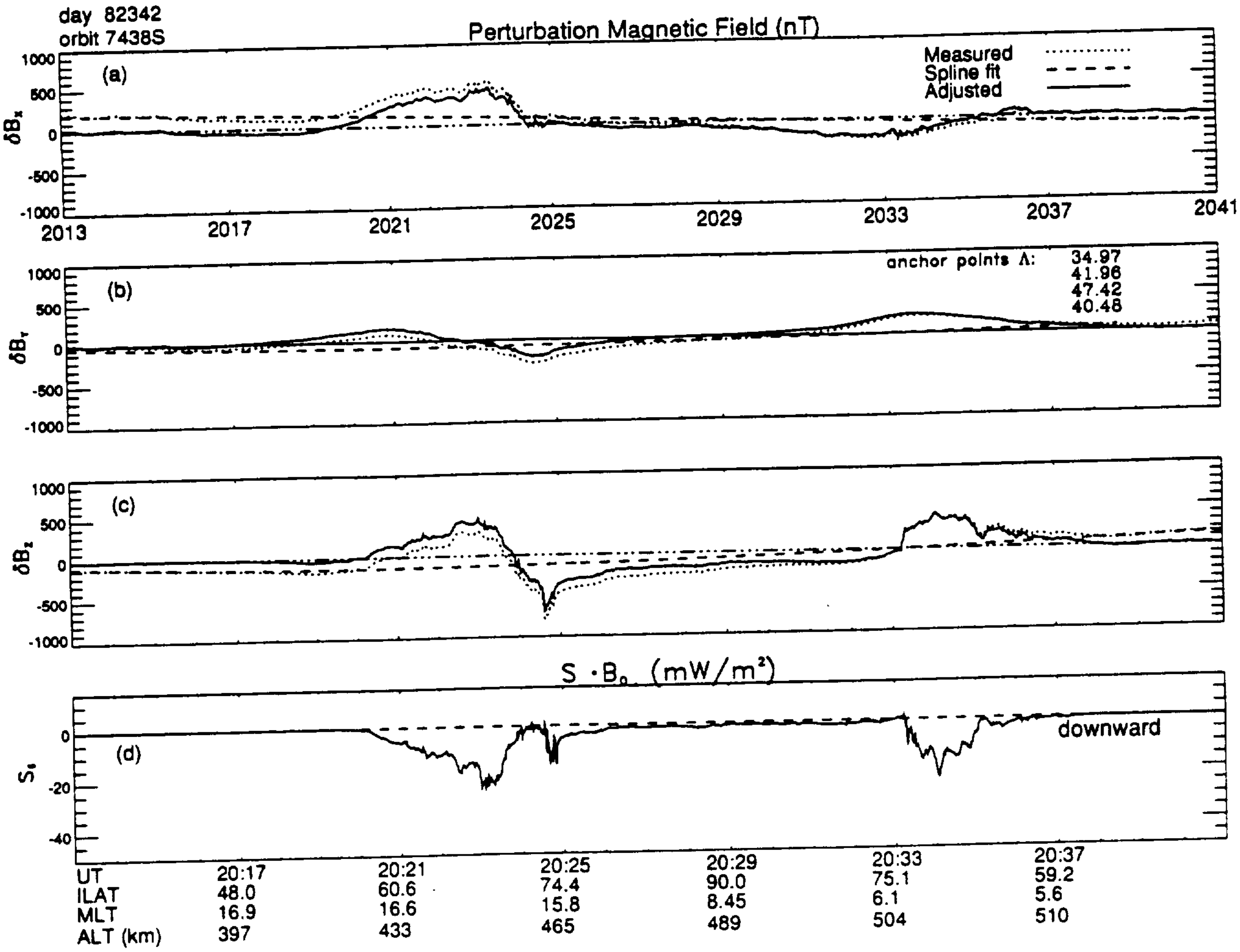

Figure 8. Perturbation magnetic field and field-aligned Poynting flux for orbit 7438 in the same format as Figure 6.

tablishing the magnitudes of the electric field and perturbation magnetic field, as well as providing error estimates for each quantity and the cumulative uncertainty of our results. The electromagnetic energy flux is equivalent to the sum of the rates at which kinetic energy is transferred to the neutral atmosphere via Lorentz (J × B) forcing and at which the atmosphere is heated by Joule dissipation. Poynting's theorem, applied to a magnetic flux tube segment bounded at the top by the satellite and at the bottom by the base of the ionosphere, allows the field-aligned energy flux measured at the satellite altitude to be equated to the rate of electromagnetic energy conversion taking place in the volume.

The ionosphere often acts as an active load in the global high latitude ionosphere-magnetosphere circuit with energy deposited from the magnetosphere into the ionosphere. Energy is delivered to the lower ionosphere when the neutral wind is in the direction of the $\mathbf{J}\times\mathbf{B}$ force, and it is transported from the region when this component of the neutral wind velocity is larger than the ion drift and oppositely directed to the $\mathbf{J}\times\mathbf{B}$ force. Hence we expect that in the auroral zones, where the ion drift and neutral wind are generally oppositely directed, the Poynting flux will be downward and dominated by the frictional heating rate. Upward Poynting flux, indicative of a dynamo process, may be expected in the polar cap at times when the neutral wind velocity may exceed the ion drift velocity. We have presented observations indicative of each of these drivers, including a sequence demonstrating the approach of a steady state neutral wind pattern.

Downward directed Poynting flux with magnitudes of a few tens of mW/m^2, typical of our observations, are consistent with a Pedersen conductivity near 10 Mhos and ion drifts of the order of 1 km/s. It is important to emphasize that the adjustments to the measured data as described here can easily alter the zero line for the derived Poynting flux by a few tens of mW/m^2. The automated correction procedure that we have outlined may be of value to investigators interested in the absolute magnitude of the perturbation magnetic field or any quantity, such as the Poynting flux, which is proportional to this magnitude. Such corrections, or lack thereof, may change observations of the downward Poynting flux by 50 percent, which may be considered unimportant to some investigations. However, such ad-

justments can change the magnitude of upward Poynting flux by several hundreds of percent, and even the inferred direction, which may lead to significant interpretive misunderstandings. Assuming that the large scale neutral wind velocity in the E region will not exceed a few hundreds of meters per second, we should not expect upward directed Poynting flux to exceed 10 mW/m^2 over large spatial scales.

Acknowledgments. This work is supported at the University of Texas at Dallas by NASA grants NAG 5-305 and NAG 5-306, and by Air Force Geophysics Directorate contract F19628-90-K-0001. The authors wish to acknowledge the extremely helpful input from F.S. Johnson of UTD, Jeff Thayer of SRI, Menlo Park, and Reuben Edgar of SwRI, San Antonio. The Editor thanks J. C. Samson and J. F. Vickrey for their assistance in evaluating this paper.

References

Anderson, P. C., W. B. Hanson, W. R. Coley, and W. R. Hoegy, Spacecraft potential effects on the Dynamics Explorer 2 satellite, *J. Geophys. Res.*, *99*, 3985, 1994.

Cummings, W.D., S.E. DeForest, and R. L. McPherron, Measurements of the Poynting vector of standing hydromagnetic waves at geosynchronous orbit, *J. Geophys. Res.*, *83*, 697, 1978.

Deng,W., T.L. Killeen, A.G. Burns, and R.G. Roble, The flywheel effect:Ionospheric currents after a geomagnetic storm, *Geophys. Res. Lett*, *18*, 1845 , 1991.

Doyle, M.A., F.J. Rich, W.J. Burke, and M. Smiddy, Field-aligned currents and electric fields observed in the region of the dayside cusp, *J. Geophys. Res.*, *86*, 5656, 1981.

Erlandson, R.E., L.J. Zanetti, T.A. Potemra, L.P. Block, and G. Holmgren, Viking magnetic and electric field observations of Pc 1 waves at high latitudes, *J. Geophys. Res.*, *95*, 5941, 1990.

Farthing, W.H., M. Sugiura, and B.G. Ledley, Magnetic field observations on DE-A and -B, *Space Sci. Instrum.*, *5*, 551, 1981.

Fejer, B.G., M.F. Larsen, and D.T. Farley, Equatorial disturbance dynamo electric fields, *Geophys. Res. Lett.*, *10*, 537, 1983.

Foster, J.C., J.-P. St.-Maurice, and V.J. Abreu, Joule Heating at hight latitudes, *J. Geophys. Res.*, *88*, 4885, 1983.

Fraser, B.J., J.C. Samson, Y.D. Hu, R.L. McPherron, and C.T. Russell, Electromagnetic ion cyclotron waves observed near the oxygen cyclotron frequency by ISEE 1 and 2, *J. Geophys. Res.*, *97*, 3063, 1992.

Hanson, W.B., R.A. Heelis, R.A. Power, C.R. Lippincott, D.R. Zuccaro, B.J. Holt, L.H. Harmon, and S. Sanatani, The retarding potential analyzer for Dynamics Explorer-B, *Space Sci. Instrum.*, *5*, 503, 1981.

Hanson, W.B., W.R. Coley, R.A. Heelis, N.C. Maynard, and T.L. Aggson, A comparison of in Situ Measurements of E and $-\mathbf{V}\times\mathbf{B}$ from Dynamics Explorer 2, *J. Geophys. Res.*, *98*, 21493, 1993.

Heelis, R.A., W.B. Hanson, C.R. Lippincott, D.R. Zuccaro, L.H. Harmon, B.J. Holt, J.E. Doherty, and R.A. Power, The ion drift meter for Dynamics Explorer-B, *Space Sci. Instrum.*, *5*, 511, 1981.

Kelley, M.C., D.J. Knudsen, and J.F. Vickrey, Poynting flux measurements on a satellite: A diagnostic tool for space research., *J. Geophys. Res.*, *96*, 201-207, 1991.

Knudsen, D.J., Alfven waves and static fields in magnetosphere/ionosphere coupling: In-situ measurements and a numerical model, Ph.D. thesis, Cornell Univ., Ithaca, N. Y., 1990.

LaBelle, J., and R.A. Treumann, Poynting vector measurements of electromagnetic ion cyclotron waves in the plasmasphere, *J. Geophys. Res.*, *97*, 13,789, 1992.

Langle, R.A., and R.H. Estes, The near-Earth magnetic field at 1980 determined from Magsat data, *J. Geophys. Res.*, *90*, 2495, 1985.

Lyons, L.R., T.L. Killeen, and R. L. Waltersheid, The neutral wind "flywheel" as a source of quiet-time, polar-cap currents, *Geophys. Res. Lett.*, *12*, 101, 1983.

Mauk, B.H., and R.L. McPherron, An experimental test of the electromagnetic ion cyclotron instability within the Earth's magnetosphere, *Phys. Fluids*, *23*, 2111, 1980.

McDiarmid, I.B., J.R. Burrows and Margaret D. Wilson, Comparison of Magnetic Field perturbations at high latitudes with charged particle and IMF measurements, *J. Geophys. Res.*, *83*, 681, 1978.

Sugiura, M., N.C. Maynard, W.H. Farthing, J.P.H.G. Ledley, and J.L.J. Cahill, Initial results on the correlation between the magnetic and electric fields observed from the DE-2 satellite in field-aligned current regions, *Geophys. Res. Lett.*, *9*, 985, 1982.

Thayer, J.P., and J.F. Vickrey, On the contribution of the thermospheric neutral wind to high-latitude energetics, *Geophys. Res. Lett.*, *19*, 265, 1992.

Vickrey, J.F., R.R. Vondrak, and S.J. Matthews, Energy deposition by precipitating particles and Joule dissipation in the auroral ionosphere, *J. Geophys. Res.*, *87*, 5184, 1982.

Zanetti, L.J., W. Baumjohann, and T.A. Potemra, Ionospheric and Birkeland current distributions inferred from the MAGSAT magnetometer data, *J. Geophys. Res.*, *88*, 4875, 1983.

J. B. Gary, R. A. Heelis, and W. B. Hanson, Center for Space Sciences, M.S. FO22, University of Texas at Dallas, P. O. Box 830688, Richardson, TX 75083.(e-mail: Internet.gary@utdallas.edu; Internet.heelis@utdallas.edu; SPAN.utspan::utadnx::utdssa::cssmail)

J. A. Slavin, Laboratory for Extraterrestrial Physics, NASA Goddard Space Flight Center, Greenbelt, MD 20771. (e-mail: Internet.slavin@lepjas.gsfc.nasa.gov)

(Received May 17, 1993; revised August 30, 1993; accepted October 28, 1993.)

APPENDIX B

Thayer, J.P., J.F. Vickrey, R.A. Heelis, and J.B. Gary, "Interpretation and modeling of the high-latitude electromagnetic energy flux," *J. Geophys. Res.*, Vol. 100, No. A10, pp. 19,715-19,728, 1995.

JOURNAL OF GEOPHYSICAL RESEARCH, VOL. 100, NO. A10, PAGES 19,715–19,728, OCTOBER 1, 1995

Interpretation and modeling of the high-latitude electromagnetic energy flux

J. P. Thayer and J. F. Vickrey
SRI International, Menlo Park, California

R. A. Heelis
Center for Space Science, Physics Program, University of Texas at Dallas, Richardson

J. B. Gary
Applied Physics Laboratory, Johns Hopkins University, Laurel, Maryland

Abstract. An interpretation of the electromagnetic energy flux at high latitudes under steady state conditions is presented and analyzed through modeling of the large-scale coupling between the high-latitude ionosphere and magnetosphere. In this paper we elucidate the steady state relationship between the electromagnetic energy flux (divergence of the dc Poynting flux), the Joule heating rate, and the mechanical energy transfer rate in the high-latitude ionosphere. We also demonstrate the important role of the neutral wind and its conductivity-weighted distribution with altitude in determining the resultant exchange of electromagnetic energy at high latitudes. Because the Poynting flux approach accounts for the neutral wind implicitly and describes the net electromagnetic energy flux between the magnetosphere and ionosphere, it is a fundamental measure of energy transfer in the system. A significant portion of this energy transfer results in Joule heating; however, the conversion of electromagnetic energy flux into mechanical energy of the neutrals is also considerable and can in some regions exceed the Joule heating rate. We will show that neglect of the neutral dynamics in calculations of the Joule heating rate can be misleading. To evaluate and interpret the electromagnetic energy flux at high latitudes, we employ the vector spherical harmonic model, which is based on the National Center for Atmospheric Research thermosphere–ionosphere general circulation model, to provide the steady state properties of the thermosphere–ionosphere system under moderate to quiet geomagnetic activity. For the specific geophysical conditions modeled we conclude that (1) the electromagnetic energy flux is predominantly directed into the high-latitude ionosphere with greater input in the morning sector than in the evening sector, as supported by DE 2 observations. (2) The Joule heating rate accounts for much of the electromagnetic energy deposited in the ionosphere with the conductivity-weighted neutral wind contributing significantly to the Joule heating rate and thus affecting the net electromagnetic energy flux in the ionosphere. (3) On average, the mechanical energy transfer rate amounts to about 10% to 30% of the net electromagnetic energy flux in the auroral dawn, dusk, and polar cap regions, acting as a sink of electromagnetic energy flux in the dawn and dusk sectors and a source in the polar cap. (4) Weak regions of upward electromagnetic energy flux are found near the convection reversal boundaries where the mechanical energy transfer rate exceeds the Joule heating rate. In general, large upward electromagnetic energy fluxes may be rare, as the always positive Joule heating rate increases irrespective of the source of electromagnetic energy flux; that is, neutral dynamics contribute directly to the Joule heating rate.

1. Introduction

The magnetosphere–ionosphere (M–I) system at high latitudes can exhibit a diverse character in the distribution of currents and electric fields and in the population and energy of plasma particles. These features help to define the various regions of the M–I system. These regions are coupled through the exchange of energy between the electromagnetic field and the plasma. The energy exchange involved in this process can be described in terms of Poynting's theorem,

$$\iiint_V \frac{\partial}{\partial t}\left(\frac{B^2}{2\mu_0} + \frac{\varepsilon_0}{2}E^2\right) dV + \iiint_V \frac{\nabla\cdot(\mathbf{E}\times\mathbf{B})}{\mu_0}\, dV + \iiint_V \mathbf{j}\cdot\mathbf{E}\, dV = 0 \qquad (1)$$

where the first term is the time rate of change of the electromagnetic energy density within the volume, the second term is the divergence of the electromagnetic (Poynting) energy flux within

Paper number 95JA01159.
0148-0227/95/95JA-01159$05.00

the volume, and the third term is the volume energy transfer rate. The derivation of Poynting's theorem comes directly from Maxwell's equations using the identity $\nabla\cdot(\mathbf{E}\times\mathbf{B}) \equiv \mathbf{B}\cdot(\nabla\times\mathbf{E}) - \mathbf{E}\cdot(\nabla\times\mathbf{B})$. For magnetospheric–ionospheric applications the magnetic field energy density, to a very good approximation, greatly exceeds the electric field energy density. Poynting's theorem, given by (1), can then be written as

$$\iiint_V \frac{\partial}{\partial t}\left(\frac{B^2}{2\mu_0}\right) dV + \iiint_V \frac{\nabla\cdot(\mathbf{E}\times\delta\mathbf{B})}{\mu_0}\, dV + \iiint_V \mathbf{j}\cdot\mathbf{E}\, dV = 0 \ , \qquad (2)$$

with $\delta\mathbf{B}$ representing the perturbation magnetic field due to the large-scale ionospheric current system [see *Kelley et al.*, 1991].

Poynting's theorem has been used to provide a general description of the energy exchange between the solar wind and magnetosphere [e.g., *Hill*, 1983; *Cowley*, 1991], for the interpretation of time-varying electromagnetic fields [e.g., *Fraser*, 1985], and, more recently, for the evaluation and interpretation of large-scale energy transfer in the ionosphere [e.g., *Cowley*, 1991; *Kelley et al.*, 1991; *Thayer and Vickrey*, 1992; *Gary et al.*, 1994]. For investigations concerned with high-latitude ionospheric energetics, the electromagnetic energy flux described by Poynting's theorem is a fundamental quantity because it describes the energy exchange between the magnetosphere and ionosphere. Joule heating and the bulk motion of the neutral gas in the high-latitude ionosphere are a direct result of this energy exchange. It is this more recent use of Poynting's theorem that will be developed further in our modeling study.

As stated by *Cowley* [1991], Poynting's theorem in the steady state demonstrates that any increase in plasma energy that occurs in one region of space must be at the direct expense of plasma energy that is lost in another, where the two regions are connected by a current tube. Thus source regions where energy is transferred from the plasma to the electromagnetic field ($\mathbf{J}\cdot\mathbf{E}$ negative) must be balanced by sink regions of energy transfer from the electromagnetic field to the plasma ($\mathbf{J}\cdot\mathbf{E}$ positive). On the basis of this premise and the magnetic coupling of the magnetosphere and ionosphere at high latitudes, source or sink regions of electromagnetic energy flux in the high-latitude ionosphere must be matched by sink or source regions in the magnetosphere.

Frequently, the ionosphere is treated purely as a resistive load acting as a sink of electromagnetic energy being converted to thermal energy of the gas. This view, however, neglects the reactive nature of the high-latitude ionosphere due to the presence of neutral winds and their potential contribution to the electrodynamics. The neutral wind acts as a modifying influence in determining how much Poynting flux is required by the magnetosphere to power the dissipation processes in the high-latitude ionosphere and may potentially make the ionosphere a source of electromagnetic energy [*Thayer and Vickrey*, 1992]. Recently, *Kelley et al.* [1991] and *Gary et al.* [1994] have shown through low-altitude, polar-orbiting satellite observations that the large-scale transfer of energy and momentum via the electromagnetic field between the solar-wind-magnetosphere and the ionosphere–thermosphere at high latitudes can be determined by evaluating the dc component of the field-aligned Poynting flux. The derived results, interpreted from observations, have shown extensive regions of electromagnetic energy flux into the high-latitude ionosphere demonstrating the magnetospheric dynamo as the dominant electrical energy source. However, electromagnetic energy flux out of the ionosphere over large scales has also been observed [see *Gary et al.*, 1994]. The outward directed energy flux can be interpreted, under steady state conditions, as having a generator in the ionosphere, presumably through the neutral wind dynamo mechanism.

Thayer and Vickrey [1992] investigated the neutral wind contribution to the high-latitude energetics by comparing two uncoupled systems: a magnetospheric circuit and an ionospheric circuit. They quantified the electrical energy contained in each system separately and demonstrated the importance of the neutral wind dynamo as a potential source of electrical energy at high latitudes. In that study, *Thayer and Vickrey* [1992] demonstrated the influence of the neutral wind on the Poynting flux by writing the steady state form of Poynting's theorem as

$$-\iiint_V \frac{\nabla\cdot(\mathbf{E}\times\delta\mathbf{B})}{\mu_0}\, dV = \iiint_V \mathbf{j}\cdot\mathbf{E}\, dV = \iiint_V \left[\mathbf{j}\cdot\mathbf{E}' + \mathbf{u}_n\cdot(\mathbf{j}\times\mathbf{B})\right] dV \ , \qquad (3)$$

where $\mathbf{E}'$ is the electric field in the frame of reference of the neutral gas and $\mathbf{E}$ is the electric field in the inertial frame. From (3) the divergence of Poynting flux is equal to the volume energy transfer rate which is equal to the sum of the Joule heating rate and the mechanical energy transfer rate. As a positive definite quantity, the Joule heating rate is a sink of electromagnetic energy flux in the ionosphere, while the mechanical energy transfer rate could be a sink or source, depending on the specific relationships among the neutral wind, conductivity, and electric field. By applying Gauss' theorem and following the arguments presented by *Kelley et al.* [1991], the divergence in the Poynting flux may be related to the vertical or field-aligned Poynting flux.

Equation (3) has important implications for studies of ionospheric and thermospheric energetics that involve a complex coupling among the conductivity, electric field, and neutral wind. The determination of the electromagnetic energy flux is further complicated by the different response times of each of these parameters to changes in the M-I system. The response time for conductivity and neutral wind is also altitude dependent with, for example, the neutral wind responding more rapidly in the *F* region than in the *E* region to changes in the electric field. Therefore determination of the field-aligned Poynting flux from measurement must insure that a quasi steady state condition is reached in order to interpret those results using the source-sink concept. However, the different response times, specifically the long response of the neutral wind compared to changes in the electric field and conductivity, allow for the neutral wind affects on the M-I system to be investigated. This was first demonstrated by *Lyons et al.* [1985] by evaluating the polar cap currents resulting from "spun-up" neutral winds and setting the ion convection to zero. *Deng et al.* [1993] investigated the effects of the time-dependent neutral wind dynamo on the high-latitude ionospheric electrodynamics after a geomagnetic storm using the National Center for Atmospheric Research (NCAR) thermosphere–ionosphere general circulation model (TIGCM) and found that the neutral wind contributes significantly to the ionospheric current system after the storm. They also calculated the electromagnetic energy flux but, unfortunately, used the independent generator calculations presented by *Thayer and Vickrey* [1992] and not the coupled expression. More recently, *Lu et al.* [1995] have used the assimilated mapping of ionospheric electrodynamics (AMIE) technique to simulate substorm and equinox conditions and evaluate the high-latitude electromagnetic energy flux using the coupled expression described by *Thayer and Vickrey* [1992].

It is important to make the distinction between the divergence in the Poynting flux and the Joule heating rate of the gas. If the ionospheric current density and electric field are measured in the inertial reference frame, then the flux of electromagnetic energy describing the heat and momentum transfer of energy between the magnetosphere and ionosphere can be determined (as demonstrated by *Kelley et al.* [1991] and *Gary et al.* [1994]). It is extremely important to note that an evaluation of the volume Joule heating rate requires a measure of the electric field in a reference frame moving with the neutral gas at all altitudes. This electric field is not a quantity that is directly measured. The common practice of computing $\Sigma_p E^2$, where E is the magnitude of the electric field in the inertial frame and Σ_p is the height-integrated Pedersen conductivity, is not necessarily a measure of the Joule heating rate. We point out here that substantial errors in both the magnitude of the Joule heating rate and in the momentum transfer rate to the neutral atmosphere may arise by making this assumption. However, the presence of the neutral wind is implicitly included in a measure of the field-aligned Poynting flux. Therefore it is important to investigate the exchange of electromagnetic energy in the high-latitude ionosphere using this source–sink concept of Poynting's theorem to provide further insight into the M–I electrodynamic system. Here we will pursue a modeling effort to treat the coupled aspects of the M–I system by evaluating the exchange of electromagnetic energy in the high-latitude ionosphere. As part of this effort, we demonstrate the important electrodynamic role of the neutral wind and its conductivity-weighted distribution in altitude. We also develop further the relationship of Poynting's theorem to ionospheric studies of Joule heating and neutral wind dynamics to elucidate the sources and sinks of electromagnetic energy in the high-latitude ionosphere.

2. Approach

Adopting the source-sink concept, we apply Poynting's theorem to the high-latitude ionosphere where the ionosphere is directly coupled to the magnetosphere through highly conducting magnetic field lines. Electromagnetic energy flux is transferred between the source and sink regions of the magnetosphere and ionosphere via electric fields and field-aligned currents. To study the sources and sinks of electromagnetic energy in the high-latitude ionosphere under steady state conditions, we use the expression for Poynting's theorem described in (3). To model this expression, we use the vector spherical harmonic (VSH) model of *Killeen et al.* [1987] to provide the necessary thermospheric and ionospheric parameters.

The VSH model is based on a spectral representation of the output fields from the NCAR-TIGCM simulations. The NCAR-TIGCM is a time-dependent, three-dimensional model that solves the fully coupled, nonlinear, hydrodynamic, thermodynamic, and continuity equations of the neutral gas self-consistently with the ion energy, ion momentum, and ion continuity equations [see *Roble et al.*, 1988, and references therein]. A simulation is uniquely determined by the input parameters to the model (i.e., EUV and UV fluxes, auroral particle precipitation, high-latitude ionospheric convection, and lower thermospheric tides). During a model run the particle fluxes and the cross polar cap potential may be specified to remain fixed throughout the 24-hour model simulation. This type of model simulation is referred to as a diurnally reproducible state, meaning the model parameters are reproducible over a model day, and the "UT effects" associated with the diurnal migration of the geomagnetic pole about the geographic pole are incorporated. Although the diurnally reproducible state may not actually occur in nature, due to shorter-term variations in the solar wind / magnetosphere interaction, the model simulation does provide a description of the global, UT-varying thermosphere–ionosphere system during a particular geophysical situation. A set of NCAR-TIGCM runs have been expanded into VSH model coefficients that can be used to represent a range of geophysical conditions.

In the TIGCM formulation the magnetosphere is treated as a generator delivering a fixed voltage to the ionosphere using the Heelis ion convection model [*Heelis et al.*, 1982]. The parameterization of the ion convection pattern is tied to estimates of the total auroral hemispheric power input from the National Oceanic and Atmospheric Administration (NOAA) / TIROS particle flux measurements (H_p index). For the model simulation, any charge separation in the ionosphere due to neutral winds or gradients in conductivity are closed through field-aligned currents. Thus, for calculations of the electromagnetic energy flux, the neutral winds contribute to the current system while the electric field originates in the magnetosphere. The model ionosphere is coupled to the magnetosphere through the imposed electric field and particle precipitation, but no direct magnetospheric feedback is incorporated into the model to address how the processes in the ionosphere influence the magnetospheric response.

In this study a model simulation providing a self-consistent description of thermosphere–ionosphere processes is used to study the coupled aspects of the M-I system at high latitudes. This approach differs from that used by *Thayer and Vickrey* [1992] in which the electrodynamic properties of the ionosphere and magnetosphere were evaluated separately to demonstrate the potential role the neutral winds could play in high-latitude electrodynamics. To make our calculations, we define a volume that covers the area from the geomagnetic pole to the 60°N magnetic latitude circle and extends in altitude from 110 to 400 km. We assume that the vertical magnetic flux tubes permeate this volume, each enclosing a 5° × 5° latitude / longitude bin. The calculations are performed at each grid point assuming horizontal uniformity of the parameters within each 5° bin. Applying these approximations to (3), the expression evaluated at each grid point in the modeling effort becomes

$$S_z = \int_z \mathbf{j}\cdot\mathbf{E}\,dz = \int_z \left[\mathbf{j}\cdot\mathbf{E}' + \mathbf{u}_n\cdot\left(\mathbf{j}\times\mathbf{B}_0\right)\right]dz \quad , \tag{4}$$

where S_z is the field-aligned Poynting flux. The coordinate system employed is right-handed, with $\hat{x}$ directed positive northward, $\hat{y}$ directed positive eastward, and $\hat{z}$ directed positive downward.

The model simulation used extensively in this study is representative of moderate to quiet geomagnetic activity (H_p index = 11 GW and cross-cap potential = 60 kV) and solar maximum conditions ($F_{10.7} = 220 \times 10^{-22}$ W m^{-2} s^{-1}). Polar plots (from the model simulation for the December solstice in the northern hemisphere at 0400 UT) of the electric field magnitude in millivolts per meter and the height-integrated Pedersen conductivity in mhos are shown in Plates 1a and b, respectively, on a magnetic latitude / magnetic local time grid extending in magnetic latitude from 60°N to the geomagnetic pole. The electric field magnitude shown in Plate 1a represents a two-cell ion convection pattern with its greatest values found inside the polar cap. The strong electric field over the polar cap will be used to demonstrate that significant ion-neutral coupling results in a small downward electromagnetic energy flux that would otherwise be large if the neutral winds were neglected. Thus the electric field contribution to the net electromagnetic energy flux is compensated by the electric field's influence on driving the neutral wind. Evidence of this effect will be demonstrated in the following sections. The distribution of the height-integrated Pedersen conductivity is structured across the polar cap with enhanced values in the midnight and dawn sectors and a factor of 3 reduction in magnitude inside the polar cap. The enhanced regions of conductivity are due to the NCAR-TIGCM formulation for auroral particle precipitation [*Roble and Ridley*, 1987].

Plates 1c and 1d are altitude plots of the local Pedersen and Hall conductivity in mhos/m along the dawn-dusk magnetic meridian. The local Pedersen conductivity peaks near 130 km with enhancements in the dawn and dusk sectors of the E region and moderate conductivity values in the polar cap in both E and F regions. The local Hall conductivity is limited to the E region with peak values near 115 km and an asymmetric distribution across the polar cap with maxima found in the dawn sector. These parameters are important contributors to the net electromagnetic energy flux into the ionosphere and will be used in the evaluation of (4). The neutral wind contribution to (4) will be discussed in more detail in section 4. Owing to the coarse 5° × 5° grid of the NCAR-TIGCM, the model parameterizations, and the inherent smoothing of the spectral representation by the VSH model, the model output variables represent only the large-scale features of the system, as discussed by *Deng et al.* [1993].

3. Analysis

We begin the analysis by evaluating the height-integrated energy transfer rate, $\mathbf{J}\cdot\mathbf{E}$, in the high-latitude ionosphere which, from (4), is equal to the field-aligned Poynting flux. The relationship of the energy transfer rate or the electromagnetic energy flux to the electric field, conductivity, and neutral wind can be shown by expanding (4) to give the expression

$$\int_z \mathbf{j}\cdot\mathbf{E}\,dz = \Sigma_p E^2 + \mathbf{E}\cdot\int_z \sigma_p\left(\mathbf{u}_n\times\mathbf{B}\right)dz + \mathbf{E}\cdot\int_z \sigma_h \mathbf{u}_n|\mathbf{B}|\,dz \quad , \tag{5}$$

where σ_p and σ_h are the local Pedersen and Hall conductivities and Σ_p is the height-integrated Pedersen conductivity. The total electromagnetic energy flux calculated from (5) for the model run described in section 2 is displayed in Plate 2a on a magnetic latitude / magnetic local time grid in units of milliwatts per square meter for the northern winter hemisphere at 0400 UT. The distribution of electromagnetic energy flux shown in Plate 2a is representative of the field-aligned Poynting flux at high latitudes. The electromagnetic energy flux is predominantly directed into the entire polar ionosphere with dawn sector values between 2.0 and 3.0 mW m^{-2}, polar cap values less than 1.0 mW m^{-2}, and dusk sector values between 1.0 and 1.5 mW m^{-2}. An asymmetry in the electromagnetic energy flux across the noon-midnight meridian is apparent in Plate 2a with more electromagnetic energy flux directed into the ionosphere in the morning sector (0000–1200 MLT) than in the evening sector (1200–0000 MLT) by a factor of 2 or more. Weak regions of negative electrical energy flux or upward Poynting flux (less than –0.1 mW m^{-2}) are determined from the model and are located in the regions near the ion convection reversals. These features of negative electrical energy flux are caused by the electrical contribution of the neutral wind, as will be discussed in section 4. If the electromagnetic energy flux in Plate 2a is integrated over the area of the polar cap, 90° to 60° magnetic latitude, the total electromagnetic power into the ionosphere is approximately 3.5×10^{11}W.

Plate 2b illustrates the total electromagnetic energy flux from a more geomagnetically active simulation using a cross-cap potential of 90 kV and an H_p index of 33 GW. The active case has features very similar to those discussed for the less active case shown in Plate 2a, however, the magnitude of the electromagnetic energy flux in the auroral zone has increased proportionally by a factor of about 3. The polar cap values in Plate 2b are of similar magnitude to those of the less active case.

Recently, *Gary et al.* [1995] provided statistical averages of the field-aligned dc Poynting flux determined from DE 2 throughout the polar cap. Using DE 2 data of ion drift velocities and magnetic fields, the field-aligned Poynting flux was calculated for some 576 orbits over the satellite lifetime using the technique described by *Gary et al.* [1994]. The data were sorted for interplanetary magnetic field (IMF) conditions (northward and southward) and geomagnetic activity ($K_p \leq 3$ and $K_p > 3$) and binned by invariant latitude and magnetic local time. In general, it was found that the average field-aligned Poynting flux is directed into the ionosphere throughout the entire polar cap, as was determined from the model simulation. The magnitudes of the averaged Poynting flux are reasonably reproduced by the model results shown in Plates 2a and 2b. Asymmetries in the average Poynting flux for both high and low K_p were determined from the observations with the dawn and noon sectors having greater values than the dusk and midnight sectors. The observed asymmetry between the dawn and dusk sectors corresponds well with that determined from the model. However, the model also predicts a strong region of downward Poynting flux in the midnight sector that is not observed in the data. This may be due to the parameterization of the particle precipitation used in the model and to the averaging over all seasons of the DE 2 data.

When averaging the DE 2 data during conditions of only upward Poynting flux, it was found that the magnitudes never exceeded –2.25 mW m^{-2} anywhere within the polar cap. An interesting feature in the DE 2 data set is the significant occurrence and magnitude of upward Poynting flux in the predawn sector during periods of southward IMF and high K_p conditions. The results of the coupled model shown in Plates 2a and 2b illustrate much weaker regions of upward Poynting flux near the convection reversal locations.

The distribution of each of the height-integrated terms given in (5) along the dawn-dusk magnetic plane in units of milliwatts per square meter is illustrated in Figure 1 to demonstrate their relative contributions to the total electromagnetic energy flux shown in Plate 2a. The total electromagnetic energy flux is given by the solid line in Figure 1 which shows the asymmetric distribution of energy flux between the dawn and dusk sectors. The first term on the right-hand side of (5), term 1, is a positive definite quantity accounting for the resistive dissipation of electromagnetic energy and, as shown by the dashed line in Figure 1, is the dominate term contributing to the positive or downward flux of electromagnetic energy into the ionosphere. Term 1 peak values of 2.0 mW m^{-2} occur in the polar cap with nearly equal enhancements of 1.5 mW m^{-2} located in the dawn and dusk sectors. The other two terms in (5) account for the electric field–neutral wind coupling in the ionosphere and tend to reduce the net flux of electromagnetic energy directed into the ionosphere. Term 2, the Pedersen term, is the main contributor to the reduction in the downward energy flux, as shown by the dotted line in Figure 1, with peak values in the

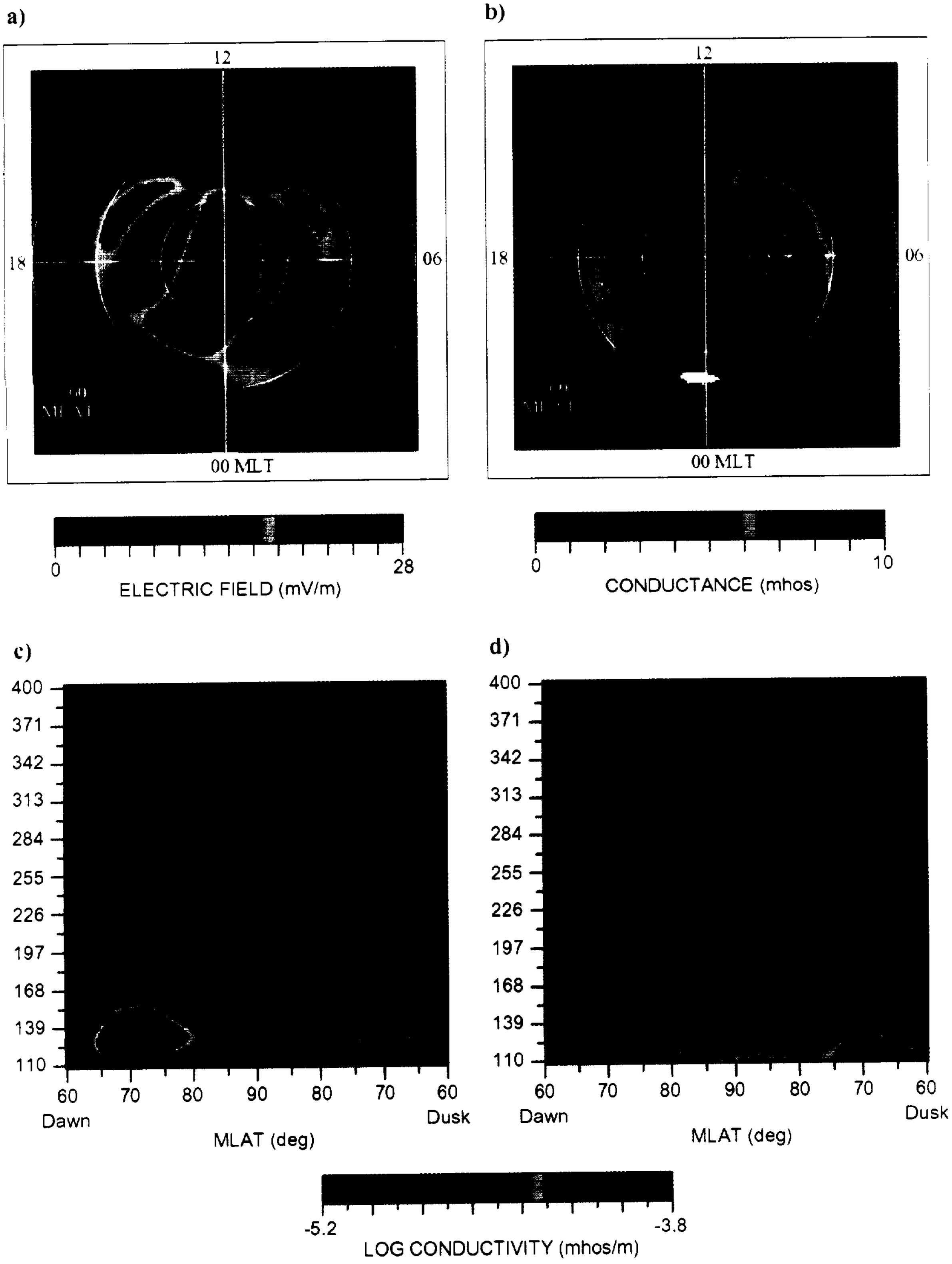

Plate 1. Polar plots on a magnetic grid of (a) electric field magnitude in millivolts per meter and (b) height-integrated Pedersen conductivity in mhos. Altitude plots along the dawn-dusk magnetic plane of the local (c) log Pedersen and (d) log Hall conductivity in mhos/m.

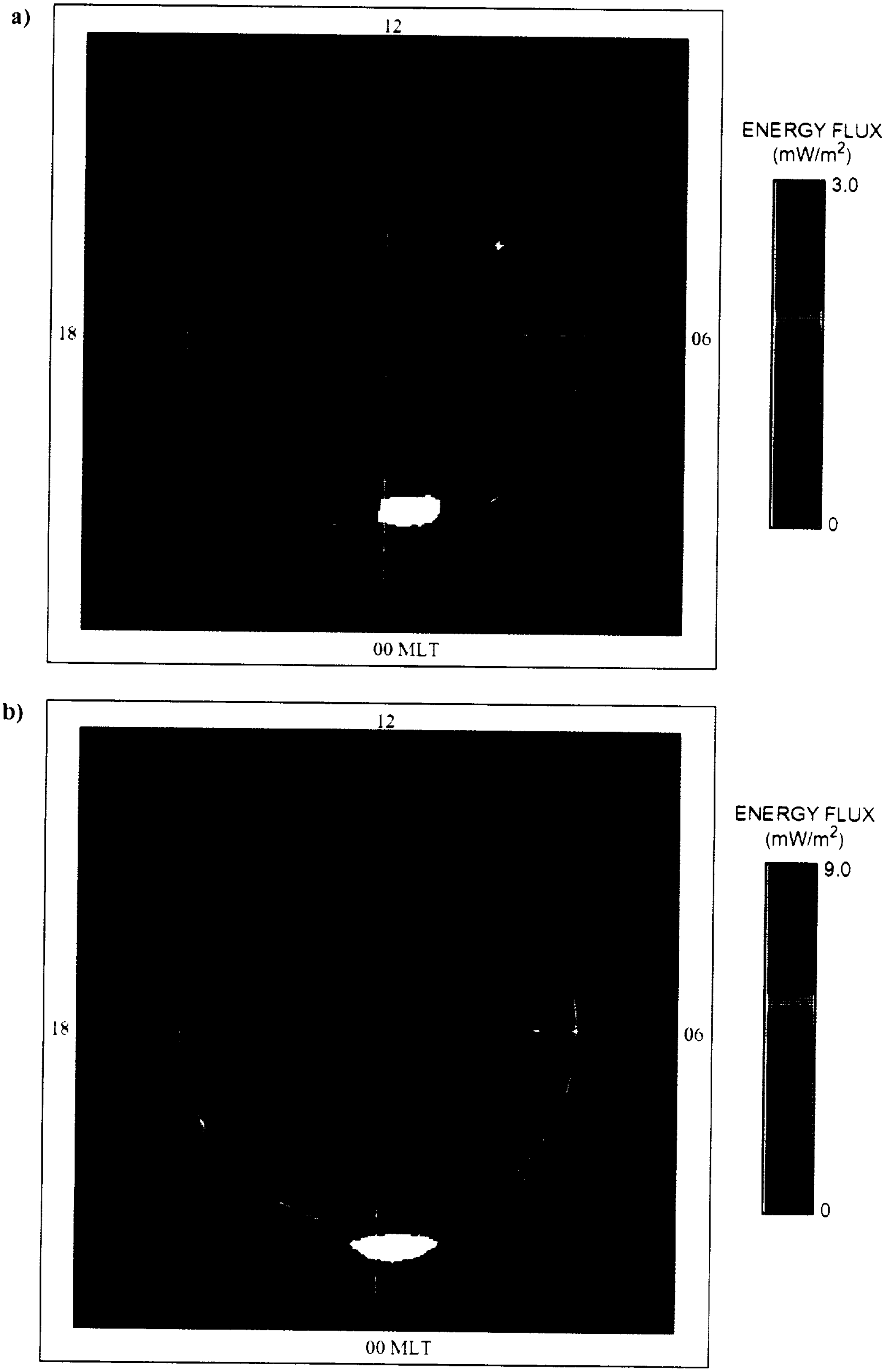

Plate 2. Polar plots on a magnetic grid of the distribution of electromagnetic energy flux for (a) 60-kV cross-cap potential and (b) 90-kV cross-cap potential.

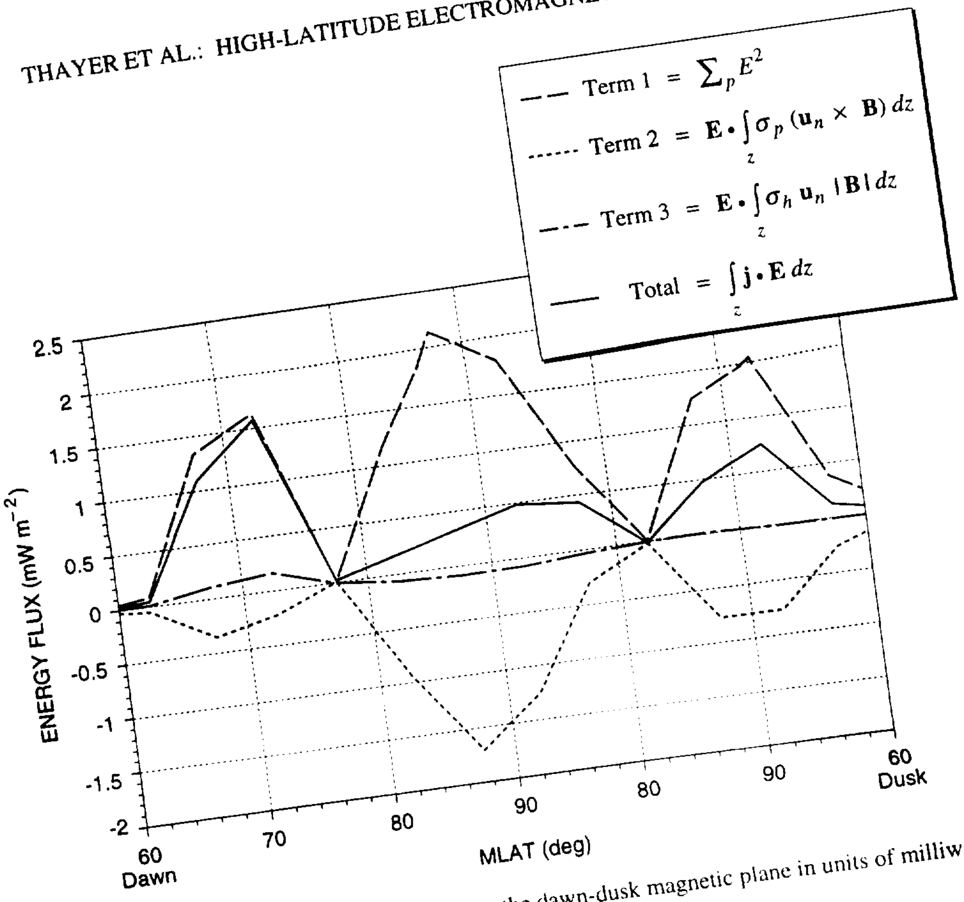

Figure 1. Height-integrated terms given in (5) along the dawn-dusk magnetic plane in units of milliwatts per square meter.

polar cap of -1.7 mW m^{-2} and values of -0.7 and -0.3 mW m^{-2} in the dusk and dawn sectors, respectively. Strong ionospheric coupling between the neutral wind and the electric field in the dusk and polar cap regions and weak coupling in the dawn sector account for the asymmetry in the dawn-dusk distribution of term 2 and are responsible for the asymmetry in the dawn-dusk distribution of the total electromagnetic energy flux. Term 3, the Hall term, is small everywhere, with values in the dawn sector of about 0.2 and -0.1 mW m^{-2} in the polar cap.

To illustrate the height dependencies in evaluating the integrals in (5), model calculations are made for each term along the dawn-dusk plane at 5-km increments from 110 to 400 km. Plate 3 is a plot of the altitude distribution for each term integrated in (5) and displayed in Figure 1. Plate 3a represents the distribution in altitude of term 1 along the dawn-dusk plane in units of 1.0 × 10^{-7} mW m^{-3}. The main contribution to this positive definite term comes from the *E* region with enhancements in the dawn, dusk, and polar cap regions. The enhancement in the polar cap is due to the presence of strong electric fields in this region, while enhancements in the dawn and dusk sector are due primarily to enhancements in the conductivity (with greater Pedersen conductivity in the dawn sector than in the dusk sector). Lesser contributions made at altitudes above the *E* region are also limited to dawn, dusk, and polar cap regions. A noticeable contribution to term 1 from the *F* region can be seen in the polar cap where soft particle precipitation enhances the Pedersen conductivity (see Plate 1c).

The altitude distribution of term 2 is illustrated in Plate 3b. This term accounts for the coupling between the electric field and the Pedersen-weighted neutral wind. Throughout all altitudes this term is predominantly negative, with most of the contribution coming from altitudes above 140 km. As illustrated by the integrated result for term 2 in Figure 1, the main contributions come from the dawn, dusk, and polar cap regions with contributions from *F* region and *E* region altitudes. The greatest contribution to term 2 comes from the polar cap at *F* region altitudes, where the neutral winds are strongly coupled to the electric field. The magnitude of term 2 with increasing altitude is quite uniform in both the dawn and dusk sectors, as a reduction in Pedersen conductivity is countered by an increase in the neutral wind. The dawn and dusk sectors illustrate the asymmetric pattern seen in the integrated result throughout all altitudes. The altitude invariance of this term demonstrates that the *F* region ion convection is strongly imposed on the neutral circulation well into the *E* region. This is a very important aspect of the model simulation, as this term is the dominant one in reducing the total electromagnetic energy flux into the ionosphere.

The coupling between the electric field and Hall-weighte neutral wind, term 3, is displayed in Plate 3c showing its altitu distribution to be isolated to the lower *E* region and concentr in the dawn and polar cap sectors. The height distributio limited by the Hall conductivity, as was shown in Plate 1d, v the distribution along the dawn-dusk plane is attributable t relationship between the electric field and the neutral wind. neutral winds in the lower *E* region are a factor of 3 to 4 le magnitude than winds in the *F* region. The lower *E* region n wind pattern is also rotated counterclockwise compared wi *F* region circulation and favors a more cyclonic neutral circulation. These variations in the neutral wind with heigh result of the complex interaction between tidal forcin magnetospheric forcing in the *E* region, as is discuss *Mikkelsen and Larsen* [1991]. Because of the counterclo

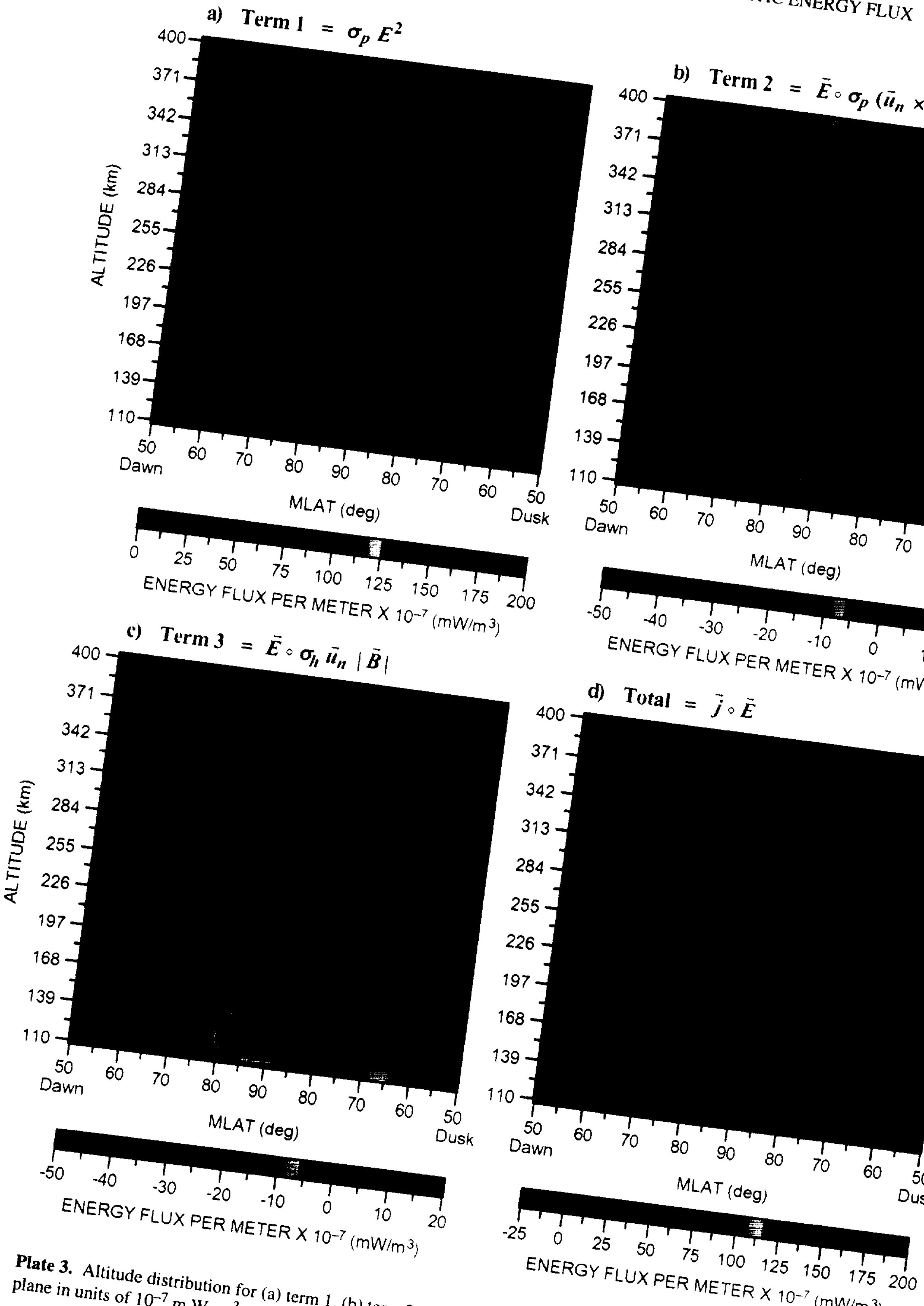

Plate 3. Altitude distribution for (a) term 1, (b) term 2, (c) term 3, and (d) total in (5) along the dawn-dusk magnetic plane in units of 10^{-7} m W m^{-3}.

rotation of the wind pattern with decreasing altitude, the winds in the polar cap are in opposite direction to the imposed dawn-dusk electric field, resulting in a negative energy flux. However, owing to the more cyclonic behavior of the *E* region winds, the electric field and winds in the dawn sector are in the same direction, resulting in a positive energy flux. Because this term does not contribute to the Joule heating rate, a positive energy flux is representative of electrical energy being converted to mechanical energy, while a negative energy flux is representative of mechanical energy converted to electrical energy. This term is less important after height integration, yet it represents a contribution that is typically not accounted for in studies of electrodynamics at high latitudes.

The altitude distribution of the net electromagnetic energy flux per meter along the dawn-dusk plane is displayed in Plate 3d. The greatest contribution to the electrical energy flux comes from the *E* region where term 1 dominates. The dawn-dusk distribution of positive electromagnetic energy flux per meter in the *E* region is skewed toward the dawn sector as terms 3 and 1 contribute positively in this sector. In the *E* region dusk sector, positive electromagnetic energy flux per meter is reduced due to term 2. In the *F* region the electromagnetic energy flux per meter is negative due to the dominating negative contribution from term 2. As will be shown, a net electromagnetic energy flux is indicative of the condition where the component of the conductivity-weighted neutral wind in the $\mathbf{E}\times\mathbf{B}$ direction exceeds the $\mathbf{E}\times\mathbf{B}$ plasma drift velocity.

4. Discussion

In section 3 we demonstrated that the neutral wind coupled with the electric field contributes significantly to reducing the dc field-aligned Poynting flux into the ionosphere, particularly in the polar cap and dusk sector. If it is assumed that the magnetic field is independent of height over our altitude range, an effective neutral wind can be determined to describe the height-integrated neutral wind profile weighted by the conductivity.

$$\mathbf{U}_{\mathrm{eff}} = \frac{\int_z \sigma_p \mathbf{u}_n \, dz + \int_z \sigma_h \hat{b}\times\mathbf{u}_n \, dz}{\Sigma_p} \quad . \qquad (6)$$

The effective neutral wind from (6) for the model simulation used above is displayed in Figure 2 with the same format as Plate 2. The resultant effective neutral wind has a pattern similar to that of the *F* region [see *Thayer and Killeen,* 1993] with speeds reduced by approximately 50%. There is also a small counterclockwise twist of the pattern due to the contribution from *E* region altitudes (see discussion by *Mikkelsen and Larsen* [1991]). The weighting of the neutral wind with height by the ionospheric conductivity results in a combined influence of neutral wind dynamics and conductivity variations with altitude.

Using (6), the electromagnetic energy flux may be written in a more informative way as

$$\int_z \mathbf{j}\cdot\mathbf{E}\, dz = \Sigma_p\left[E^2 - \mathbf{U}_{\mathrm{eff}}\cdot(\mathbf{E}\times\mathbf{B})\right] \quad . \qquad (7)$$

Expressed in this form, the effective neutral wind acts as a modifying influence on what fraction of Poynting flux energy supplied by the magnetosphere is involved in dissipation processes in the high-latitude ionosphere, as discussed previously. However, the neutral wind's influence may make the ionosphere a source of electromagnetic energy ($\mathbf{J}\cdot\mathbf{E}$ negative) if the effective neutral wind has a component in the $\mathbf{E}\times\mathbf{B}$ direction that exceeds the $\mathbf{E}\times\mathbf{B}$ plasma drift velocity. The negative or upward Poynting flux regions discussed above are located near the convection reversal boundaries where the effective neutral wind in the $\mathbf{E}\times\mathbf{B}$ direction exceeds the plasma drift velocity. At the convection reversal boundaries there is no Poynting flux because the electric field is zero. In the polar cap, small or near-zero downward Poynting flux can also occur, as the effective neutral wind is antisunward and approaches the velocity of the $\mathbf{E}\times\mathbf{B}$ plasma drift due to complementary pressure gradient and ion drag forces. Individual DE 2 orbits of the Poynting flux from *Gary et al.* [1994] have shown small and near-zero values for the downward Poynting flux inside the polar cap.

Thus it is the component of the effective neutral wind in the $\mathbf{E}\times\mathbf{B}$ direction that is important for energetics in the steady state, not the effective neutral wind vector itself. Because the effective neutral wind is very similar to the $\mathbf{E}\times\mathbf{B}$ plasma drift in the dusk and polar cap regions, an asymmetry in the high-latitude distribution of the electromagnetic energy flux results. The influence of the effective neutral wind coupled to the electric field is illustrated in Figure 1 by combining the results of terms 2 and 3 from (5). Referring to Figure 1, the enhancement of negative energy flux in the polar cap is a result of the effective neutral wind having a strong component in the $\mathbf{E}\times\mathbf{B}$ direction. The asymmetry in the negative electromagnetic energy flux from terms 2 and 3 between the dawn and dusk sectors reflects the dawn-dusk asymmetry demonstrated by the effective neutral wind pattern shown in Figure 2. This asymmetry has also been observed in the *F* region neutral circulation pattern [e.g., *Thayer and Killeen,* 1993]. *Thayer and Killeen* [1993] demonstrated that an ion convection pattern with dawn and dusk cells of equal and opposite potential results in an asymmetric neutral circulation pattern with

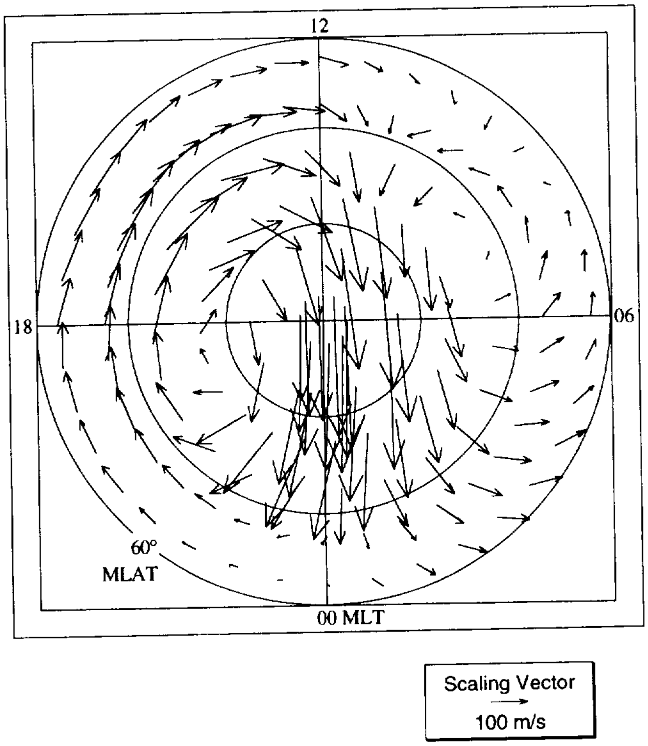

Figure 2. Polar plot of the effective neutral wind (same format as Plate 2).

the dawn cell less organized than the dusk cell. *Gundlach et al.* [1988] explain this asymmetry in terms of the disparate balance of hydrodynamic forces between the dusk and dawn sectors. In Figure 1 the higher positive values of the net electrical energy flux (solid line) in the dawn sector demonstrate that the effective neutral wind is less coupled to the electric field in the dawn sector than in the dusk sector. Overall, the neutral wind contribution to the energy flux in the ionosphere is significant, particularly in the polar cap and dusk sector (as was concluded by *Thayer and Vickrey* [1992]).

We have shown that the neutral wind contributes significantly to the overall electromagnetic energy flux in the high-latitude ionosphere. However, we have not determined how much the neutral wind is contributing to the Joule heating of the gas or to the mechanical energy of the gas. The partitioning of electromagnetic energy flux into its sinks (kinetic and internal energy of the gas) and sources (electrical energy caused by the neutral wind dynamo) can be addressed by evaluating separately the Joule heating rate and mechanical energy transfer rate described in (3).

Joule Heating Rate

The Joule heating rate is a positive definite quantity acting purely as a sink of electromagnetic energy in the ionosphere as electrical energy is transferred to the internal energy of the gas as heat. The height-integrated Joule heating rate can be obtained without approximation given the height distribution of the neutral wind, electric field, and conductivity as described by the expression

$$\int_z \mathbf{j}\cdot\mathbf{E}'\,dz = \int_z \mathbf{j}\cdot\left(\mathbf{E}+\mathbf{u}_n\times\mathbf{B}\right)dz = \int_z \sigma_p\left(\mathbf{E}+\mathbf{u}_n\times\mathbf{B}\right)^2 dz \quad . \qquad (8)$$

An illustration of the height-integrated Joule heating rate for the simulation described in the previous sections is given in Plate 4a. The main features of the Joule heating pattern are enhanced regions of Joule heating in the auroral oval with maxima in the dawn and postmidnight sectors and relatively weak enhancements in the dusk sector and inside the polar cap. The Joule heating rate displays an asymmetric pattern in the auroral zone with the Joule heating rate in the dawn sector a factor of 3 greater than in the dusk sector. Comparing these results with the electromagnetic energy flux calculations given in Plate 2a, we find that the magnitude and pattern of the Joule heating rate are very similar to the electromagnetic energy flux. Thus most of the electromagnetic energy flux directed into the ionosphere is dissipated as heat under the conditions of this simulation. That is not to say that the neutral winds contribute insignificantly to the distribution of the electromagnetic energy flux at high latitudes but that the winds are contributing most to the Joule heating rate of the gas.

To elucidate the impact of the neutral wind on the Joule heating rate at high latitudes, a calculation of the Joule heating rate neglecting the neutral wind is shown in Plate 4b. Neglecting the neutral wind has its greatest impact in the dusk sector and central polar cap where the Joule heating rate is overestimated by as much as a factor of 3. This makes the point that although the electric field or conductivity may be enhanced in these regions, the neutral winds are also strongly coupled to the electric field, resulting in a much lower Joule heating rate than might be anticipated if the winds are ignored.

Because the Poynting flux approach implicitly accounts for the neutral wind and describes the net electromagnetic energy flux between the magnetosphere and ionosphere, it is a fundamental measure of energy transfer in the system. As we have just shown, the Joule heating rate is a significant part of the electromagnetic energy flux. Given a better understanding for the quantities $\mathbf{j}\cdot\mathbf{E}$ (the electromagnetic energy flux) and $\mathbf{j}\cdot\mathbf{E}'$ (the Joule heating rate), it is worth reviewing the approaches taken by many investigators in evaluating empirically the Joule heating rate in the high-latitude ionosphere and how these approaches relate to the electromagnetic energy flux. These investigations are mainly to quantify the height-integrated Joule heating rate to describe the change in the internal energy of the gas caused by the dissipation of electrical energy in the ionosphere. Because of the difficulty in determining the neutral wind with height, approximations to the neutral wind are typically made when calculating the Joule heating rate from measurements. However, the manner in which the approximation to the neutral wind is treated can result in different interpretations for the evaluated Joule heating rate and, subsequently, the electromagnetic energy flux.

For the case when the height distribution of the conductivity and electric field (typically assumed independent of height) are known and the neutral wind is assumed to be zero, the form of the height-integrated Joule heating rate is $\mathbf{J}\cdot\mathbf{E}' = \mathbf{J}\cdot\mathbf{E} = \Sigma_p E^2$. This form of the equation represents the electromagnetic energy flux and means that the mechanical energy of the gas is zero. Thus electromagnetic energy from the magnetosphere described by the divergence in the Poynting flux is dissipated entirely in the ionosphere (acting purely as a resistive load described by the height-integrated Pedersen conductivity) as thermal energy. This can be considered the standard approach used in many investigations of high-latitude energetics [e.g., *Banks et al.*, 1981; *Foster et al.*, 1983]. We have demonstrated in Plate 4 that this assumption can be quite misleading for the conditions modeled in this simulation, particularly in the dusk sector and the central polar cap.

A different interpretation results for this case if the height distribution of the current density, instead of the conductivity, is known. For instance, if the current distribution is determined by solving the expression $\mathbf{j} = en_e\left(\mathbf{V}_i - \mathbf{V}_e\right)$ from measurements at different altitudes, say, from radar measurements [e.g., *Kamide and Brekke*, 1993], and the neutral wind is assumed zero, then the height-integrated Joule heating rate is actually the total electromagnetic energy flux converted, dissipated, or generated in the ionosphere. This can be seen more clearly by expressing the current density in the form $\mathbf{j} = \overline{\overline{\sigma}}\cdot(\mathbf{E} + \mathbf{u}_n \times \mathbf{B})$. This shows that the height distribution of the neutral wind is implicit within the measurement of j. Also, the Joule heating rate is a positive definite quantity, but the determination of $\mathbf{j}\cdot\mathbf{E}$ could be of either sign, as discussed by *Thayer and Vickrey* [1992]. The same result occurs if the height-integrated current density and the electric field are determined from a satellite measurement of **E** and $\delta\mathbf{B}$, exemplified by the recent DE 2 field-aligned Poynting flux results described by *Gary et al.* [1994].

In more general terms, if the neutral wind is contributing at all to the energetics, it is implicitly contained within the current density and the electric field; the distribution between these two depends on the electrical coupling between the ionosphere and magnetosphere. Irrespective of whether neutral wind contributions are contained in the current density or electric field, their effects on the net electromagnetic energy flux are accounted for if both the current density and electric field are determined. Furthermore, the measure of the electromagnetic energy flux is a more fundamental quantity than the Joule heating rate and may be more accurately determined from spacecraft or ground-based instruments capable of measuring the electric field and the ionospheric current density.

Mechanical Energy Transfer Rate

The mechanical energy transfer rate is either a sink or source of electromagnetic energy flux, depending on whether electromagnetic energy is converted into the bulk motion of the neutral gas (sink) or generated by the motion of the neutral gas through dynamo action (source). In this steady state model simulation the conductivity-weighted neutral wind acts as an electrical source by contributing to the current distribution in the ionosphere. As a sink of electromagnetic energy, the conductivity-weighted neutral wind is powered by the $\mathbf{J}\times\mathbf{B}$ force. The sign of the mechanical energy transfer rate illustrates whether the neutral wind is opposite (negative) or in the direction of (positive) the $\mathbf{J}\times\mathbf{B}$ force. A negative mechanical energy transfer rate would indicate that the neutral winds are opposing the $\mathbf{J}\times\mathbf{B}$ force and energy is transformed from mechanical form to electrical form and vice versa.

Figure 3 is a plot of the height-integrated mechanical energy transfer rate, Joule heating rate, and the total electromagnetic energy flux along the dawn-dusk plane, similar in format to Figure 1. The height-integrated Joule heating rate in Figure 3 (dashed line) accounts for much of the electromagnetic energy flux into the ionosphere (solid line), as was demonstrated by Plate 4a. The mechanical energy transfer rate is positive in the dawn and dusk sectors and negative in the polar cap. The positive mechanical energy transfer rate in the dawn and dusk sectors therefore acts as a sink of electromagnetic energy. Here electrical energy is being converted to the mechanical energy of the gas in an effort to maintain sunward plasma flow in these sectors. In the polar cap the mechanical energy transfer rate acts as a source of electrical energy, as the winds are complemented by pressure gradient and ion drag forces. Figure 4 is a plot of the percent contribution from the Joule heating rate (dashed line) and the mechanical energy transfer rate (dotted line) to the net electromagnetic energy flux. The percent relative contribution of the Joule heating rate and mechanical energy transfer rate is determined by the expression 100 · |J| / (|J| + |M|) and 100 · |M| / (|J| + |M|), respectively. In the dawn and dusk sectors the contribution from the mechanical energy transfer rate varies between 10 and 30%. In the polar cap, where the mechanical energy transfer rate is negative, the contribution to the electromagnetic energy flux is also between about 10 and 30%. In the locations near the ion convection reversal boundaries the mechanical energy transfer rate can contribute as much as the Joule heating rate, allowing for the possibility of a net upward Poynting flux.

In steady state a net upward (negative) electromagnetic energy flux can only be generated by a negative mechanical energy transfer rate that exceeds the Joule heating rate. However, a net electromagnetic energy flux directed downward into the ionosphere (positive) still allows for the generation of electrical energy in the ionosphere (that is, the mechanical energy transfer rate may still be negative). This is because when the neutral wind opposes the $\mathbf{J}\times\mathbf{B}$ force, resulting in a negative mechanical energy transfer rate, the Joule heating rate increases and becomes even more positive. This can be seen if we expand the expressions for the mechanical energy transfer rate

$$\int_z \mathbf{u}_n\cdot(\mathbf{j}\times\mathbf{B})\,dz = -\mathbf{E}\cdot\int_z \sigma_p\left(\mathbf{u}_n\times\mathbf{B}\right)dz + \mathbf{E}\cdot\int_z \sigma_h \mathbf{u}_n|\mathbf{B}|dz - \int_z \sigma_p\left(\mathbf{u}_n\times\mathbf{B}\right)^2 dz \quad . \tag{9}$$

and the Joule heating rate

$$\int_z \mathbf{j}\cdot\mathbf{E}'\,dz = \Sigma_p E^2 + 2\mathbf{E}\cdot\int_z \sigma_p\left(\mathbf{u}_n\times\mathbf{B}\right)dz + \int_z \sigma_p\left(\mathbf{u}_n\times\mathbf{B}\right)^2 dz \quad . \tag{10}$$

The addition of (9) and (10) results in the expression for the electromagnetic energy flux given by (5). It can be seen from the

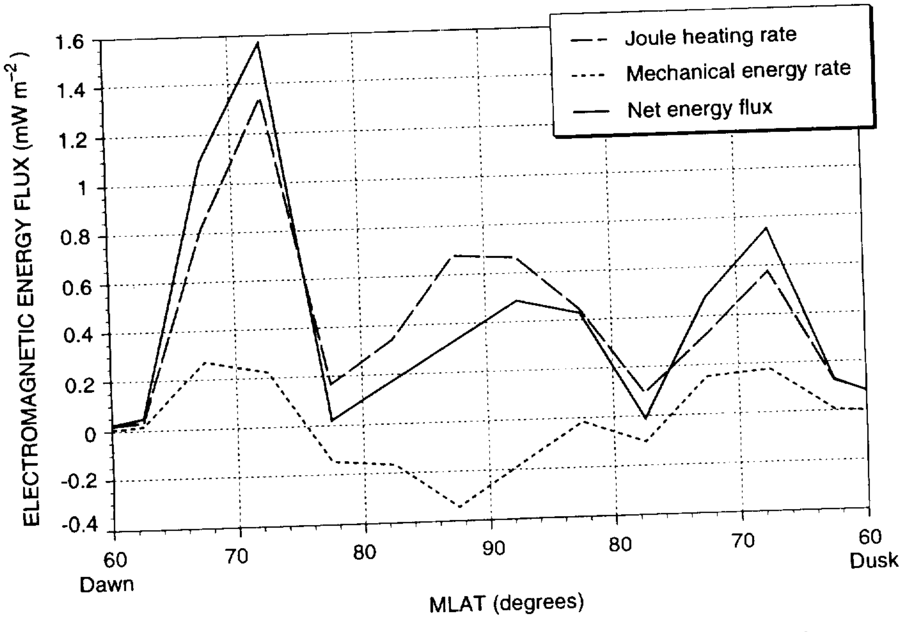

Figure 3. Height-integrated mechanical energy transfer rate, Joule heating rate, and total electromagnetic energy flux along the dawn-dusk magnetic plane (same format as Figure 1).

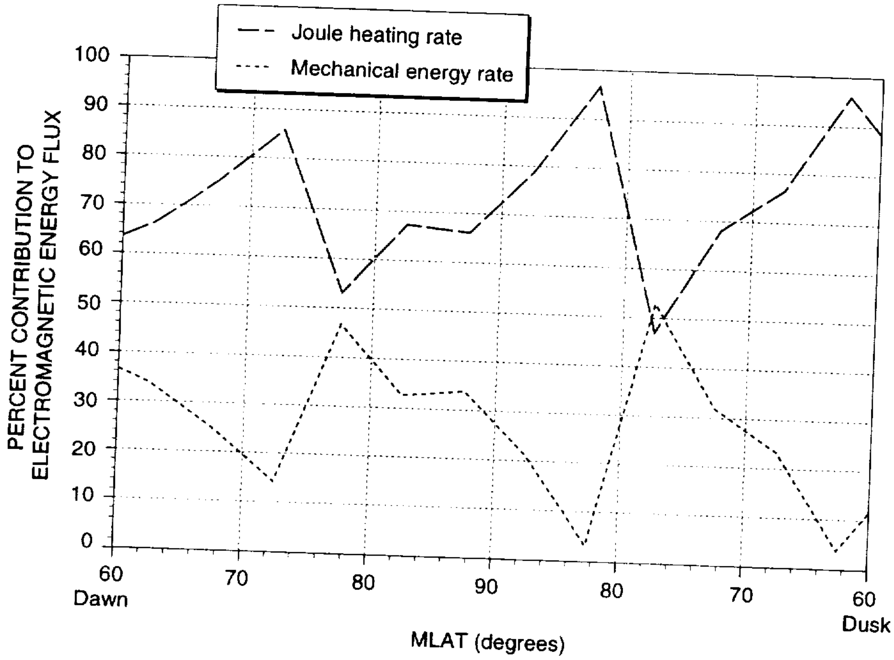

Figure 4. Percent contribution from the Joule heating rate and the mechanical energy transfer rate to the net electromagnetic energy flux.

two equations that any negative contribution to the mechanical energy transfer rate provided by the first and last terms of (9) result in a more positive Joule heating rate. The Hall term given by the second term in (9) is the only independent contributor in the mechanical energy transfer rate equation that would directly influence the net electromagnetic energy flux. However, the height-integrated Hall term was shown in Figure 1 to be a minor contributor to the net electrical energy flux. As was shown earlier by (7), the only time the net electromagnetic energy flux can be upward is when the height-integrated, conductivity-weighted neutral wind in the **E**×**B** direction exceeds the **E**×**B** plasma drift velocity. This would cause term 3 in the mechanical energy transfer rate equation (9) to become more negative than the positive values of term 1 in (9) and reduce the Joule heating rate such that a negative electromagnetic energy flux results. The offsetting terms in (9), the weak contribution from the Hall term, and the always positive Joule heating rate preclude the existence of a large, sustained upward Poynting flux under these modeled conditions and quite possibly in nature, as demonstrated by the DE 2 results.

5. Conclusions

We investigated the exchange of electromagnetic energy in the high-latitude ionosphere using a steady state, source-sink concept of Poynting's theorem to provide further insight into the M-I electrodynamic system. Poynting's theorem applied to the high-latitude M-I system and the theorem's relationship with the Joule heating rate and mechanical energy transfer rate have been elucidated and the consequences of this relationship evaluated through numerical modeling. Because the Poynting flux approach accounts for the neutral wind implicitly and describes the net electromagnetic energy flux between the magnetosphere and ionosphere, it represents a fundamental measure of energy transfer in the system. The Joule heating rate is a significant part of the energy exchange but requires accurate modeling of the neutral wind. Evaluation of the contributing factors to the electromagnetic energy flux has a strong dependence on the extent of the coupling among the conductivity, neutral wind, and electric field throughout the *E* and *F* regions.

Here we used the VSH model to provide the necessary thermosphere-ionosphere parameters to evaluate and interpret the electromagnetic energy flux at high latitudes for moderate to quiet geomagnetic conditions during solar maximum. Although the model is coupled to the magnetosphere through the mapping of the magnetospheric electric field and particle precipitation, no direct feedback to the magnetosphere has been attempted. To this end, any neutral wind dynamo action in the model would be manifested in terms of currents, with the magnetosphere acting as a pure voltage generator. This study is representative of the situation where the neutral winds have had sufficient time to respond to the imposed electric field. In a "real world" situation this may not be the case and the results of this study may change; however, irrespective of how the conditions change, the importance of the electric field-neutral wind coupling on the electromagnetics cannot be ignored. In support of the model the simulated results compare well with the measurements made by the DE 2 satellite.

The analysis of the steady state electromagnetic energy flux at high latitudes under the model conditions of moderate to quiet geomagnetic activity, December solstice, solar maximum has lead to a number of conclusions.

1. The electromagnetic energy flux or field-aligned Poynting flux is predominantly directed into the high-latitude ionosphere with weak regions of upward electromagnetic energy flux near the boundaries of the convection reversals. The distribution of electromagnetic energy flux at high latitudes is asymmetric with greater downward flux in the morning sector than in the evening sector. The region of the polar cap has the lowest values of downward electromagnetic energy flux.

2. The Joule heating rate accounts for much of the electromagnetic energy converted in the ionosphere with the conductivity-weighted neutral wind contributing significantly to

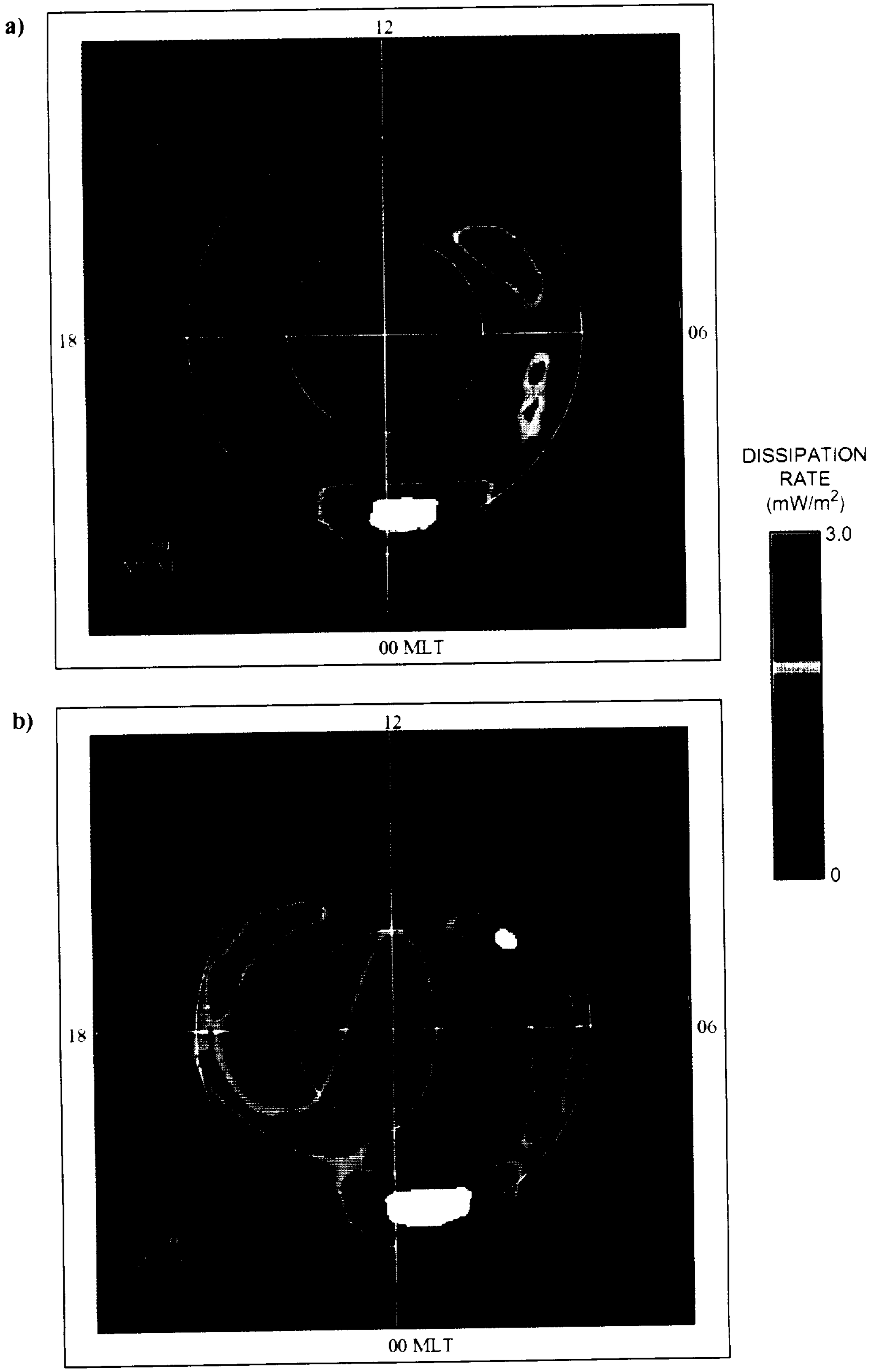

Plate 4. Polar plots of (a) the height-integrated Joule heating rate with neutral winds and (b) height-integrated Joule heating rate without neutral winds (same format as Plate 2).

the Joule heating rate and thus affecting the net electromagnetic energy flux between the magnetosphere and ionosphere.

3. On average, the mechanical energy transfer rate amounts to about 10 to 30% of the net electromagnetic energy flux in the dawn, dusk, and polar cap regions, acting as a sink of electromagnetic energy flux in the dawn and dusk sectors and as a source of electromagnetic energy flux in the polar cap.

4. Weak upward electromagnetic energy flux is found in the regions near the convection reversal boundaries due to the mechanical energy transfer rate exceeding the Joule heating rate. The upward electromagnetic energy flux was found to be small, partly due to the relation of the conductivity-weighted neutral wind to the imposed electric field and partly due to the Joule heating rate increasing irrespective of the source of electromagnetic energy flux.

This analysis of the electromagnetic energy flux at high latitudes has led to a better understanding of the significance of Poynting flux measurements. Moreover, it tests the models in their ability to properly address the extent of the coupling among the conductivity, neutral wind, and electric field throughout the *E* and *F* regions. It is apparent from the simulations used in this study that the neutral wind is strongly coupled to the electric field well into the *E* region. Observational evidence of the electrical coupling with altitude needs to be gathered to validate the model's electrical characteristics, particularly in the *E* region. An outstanding question that needs observational support is to what extent do the tidal forces from below and electric field forces from above influence the electrical coupling in the *E* region. Measurements in the central polar cap may be most effective in addressing this issue, as the electric field, neutral wind, and conductivity can be significant in this region, but yet the net electromagnetic energy flux is small.

Acknowledgments. This work was supported by NASA contract NAS5-31214 and NASA grant NAGW-3508. We would like to thank Tim Killeen, Rob Raskin, and Alan Burns at the University of Michigan for the VSH model code.

The Editor thanks D. J. Knudsen and J. C. Foster for their assistance in evaluating this paper.

References

Banks, P. M., J. C. Foster, and J. R. Doupnik, Chatanika radar observations relating to the latitudinal and local time variations of Joule heating, *J. Geophys. Res.*, *86*, 6869-6878, 1981.

Cowley, S. W. H., Acceleration and heating of space plasmas: Basic concepts, *Ann. Geophys.*, *9*, 176-187, 1991.

Deng, W., T. L. Killeen, A. G. Burns, R. G Roble, J. A. Slavin, and L. E. Wharton, The effects of neutral inertia on ionospheric currents in the high-latitude thermosphere following a geomagnetic storm, *J. Geophys. Res.*, *98*, 7775-7790, 1993.

Foster, J. C., J.-P. St.-Maurice, and V. J. Abreu, Joule heating at high latitudes, *J. Geophys. Res.*, *88*, 4885-4896, 1983.

Fraser, B. J., Observations of Ion Cyclotron waves near synchronous orbit and on the ground, *Space Sci. Rev.*, *42*, 357-374, 1985.

Gary, J. B., R. A. Heelis, W. B. Hanson, and J. A. Slavin, Field-aligned poynting flux observations in the high-latitude ionosphere, *J. Geophys. Res.*, *99*, 11,417-11,427, 1994.

Gary, J. B., R. A. Heelis, and J. P. Thayer, Summary of field-aligned poynting flux observations from DE-2, *Geophys. Res. Lett.*, in press, 1995.

Gundlach, J. P., M. F. Larsen, and I. S. Mikkelsen, A simple model describing the nonlinear dynamics of the dusk / dawn asymmetry in the high-latitude thermospheric flow, *Geophys. Res. Lett.*, *15*, 307-310, 1988.

Heelis, R. A., J. K. Lowell, and R. W. Spiro, A model of the high-latitude ionospheric convection pattern, *J. Geophys. Res.*, *87*, 6339-6345, 1982.

Hill, T. W., Solar-wind magnetosphere coupling, in *Solar-Terrestrial Physics*, edited by R. L. Carovillano and J. M. Forbes, pp. 261-302, D. Reidel, Norwell, Mass., 1983.

Kamide, Y., and A. Brekke, Altitude variations of ionospheric currents at auroral latitudes, *Geophys. Res. Lett.*, *20*, 309-312, 1993.

Kelley, M. C., D. J. Knudsen, and J. F. Vickrey, Poynting flux measurements on a satellite: A diagnostic tool for space research, *J. Geophys. Res.*, *96*, 201-207, 1991.

Killeen, T. L., R. G. Roble, and N. W. Spencer, A computer model of global thermospheric winds and temperatures, *Adv. Space Res.*, *7*, 207-215, 1987.

Lu, G., A. D. Richmond, B. A. Emery, and R. G. Roble, Magnetosphere–ionosphere–thermosphere coupling: Effect of neutral winds on energy transfer and field-aligned current, *J. Geophys. Res.*, in press, 1995.

Lyons, L. R., T. L. Killeen, and R. L. Walterscheid, The neutral wind "flywheel" as a source of quiet-time, polar-cap currents, *Geophys. Res. Lett.*, *12*, 101-104, 1985.

Mikkelsen, I. S., and M. F. Larsen, A numerical modeling study of the interaction between the tides and the circulation forced by high-latitude plasma convection, *J. Geophys. Res.*, *96*, 1203-1213, 1991.

Roble, R. G., and E. C. Ridley, An auroral model for the NCAR thermospheric general circulation model, *Ann. Geophys., Ser. A*, *5A*, 369-382, 1987.

Roble, R. G., E. C. Ridley, A. D. Richmond, and R. E. Dickinson, A coupled thermosphere / ionosphere general circulation model, *Geophys. Res. Lett.*, *15*, 1325-1328, 1988.

Thayer, J. P., and T. L. Killeen, A kinematic analysis of the high-latitude thermospheric neutral circulation pattern, *J. Geophys. Res.*, *98*, 11,549-11,565, 1993.

Thayer, J. P., and J. F. Vickrey, On the contribution of the thermospheric neutral wind to high-latitude energetics, *Geophys. Res. Lett.*, *19*, 265-268, 1992.

J. B. Gary, Applied Physics Laboratory, Johns Hopkins University, Johns Hopkins Rd., Laurel, MD 20723. (email: gary@archer.jhuapl.edu)

R. A. Heelis, Physics Program, Center for Space Science, University of Texas at Dallas, Richardson, TX 75083. (email: heelis@utdallas.edu)

J. P. Thayer and J. F. Vickrey, SRI International, 333 Ravenswood Avenue, Menlo Park, CA 94025. (email: jeff_thayer@qm.sri.com; vickrey@sri.com)

(Received December 9, 1994; revised April 3, 1995;
accepted April 3, 1995.)

APPENDIX C

Gary, J.B., R.A. Heelis, and J.P. Thayer, "Summary of field-aligned Poynting flux observations from DE 2," *Geophys. Res. Lett*, 22, 1861-1864, 1995.

GEOPHYSICAL RESEARCH LETTERS, VOL. 22, NO. 14, PAGES 1861-1864, JULY 15, 1995

Summary of field-aligned Poynting flux observations from DE 2

J. B. Gary [1] and R. A. Heelis
University of Texas at Dallas, Richardson

J. P. Thayer
SRI International, Menlo Park, California

Abstract. Using DE 2 data of ion drift velocities and magnetic fields, we have calculated the field-aligned Poynting flux ($S_{||}$) for 576 orbits over the satellite lifetime. This is the first application over an extended data set of Poynting flux observations from in situ measurements. The data has been sorted by interplanetary magnetic field conditions (northward or southward IMF) and geomagnetic activity (Kp≤3 and Kp >3) and binned by invariant latitude and magnetic local time. Our general results may be summarized as 1) the averaged $S_{||}$ is everywhere directed into the ionosphere, indicating that electric fields of magnetospheric origin generally dominate, and 2) the distribution of $S_{||}$ for southward IMF can be well explained in terms of an average two cell convection pattern, while for northward IMF a multiple cell convection pattern may be inferred. We have addressed the interesting question of the distribution of upward Poynting flux by binning only upward observations and found that average upward Poynting flux of less than 3 mW/m^2 may occur anywhere across the high latitude ionosphere. We have also observed a region at high latitudes in the predawn sector where the average upward Poynting flux is of significant size and occurrence frequency during southward IMF and high Kp conditions.

Introduction

Several studies of large scale energy dissipation in the high latitude ionosphere have been conducted in the past. They have either involved radar observations [e.g., *Vickrey et al.*, 1982 and included references] or satellite measurements [e.g., *Heelis and Coley*, 1988, *Foster et al.*, 1983] of plasma densities and electric fields together with models of the height-integrated conductivities to estimate the Joule heating rate as $\Sigma_P E^2$, where Σ_P is the height-integrated Pedersen conductivity and E is the electric field in the ionosphere. The use of field-aligned Poynting flux ($S_{||}$) derived from satellite observations of electric fields and perturbation magnetic fields as proposed by *Kelley et al.* [1991] has recently been added as a method for determining the large scale energy conversion, or transfer, rate **E**·**J** in the ionosphere.

There are two advantages to using $S_{||}$ over electric field and energetic particle observations that are related to the inclusion of neutral wind effects and an independence from modeled conductivities. Computations of the Joule heating rate cannot take into account the height-integrated effects of the electric field, conductivities, and neutral wind motions [e.g., *Banks*, 1977, *Heelis and Coley*, 1988] whereas the Poynting flux is directly dependent on these parameters. *Thayer and Vickrey* [1992] and *Deng et al.* [1993] have recently used models of thermospheric circulation to estimate the magnitude of the electromagnetic energy generated by neutral wind dynamo actions and have related this to possible observations of the Poynting flux.

Data Presentation

In a previous work [*Gary et al.*, 1994], we have described our technique for determining $S_{||}$ from DE 2 observations of the ion drift velocity (**V**) and perturbation magnetic field (δ**B**). Of the several thousand orbits during the satellite lifetime, only about 1300 passes over the high latitude region are available which are suited to our purposes. Determination of $S_{||}$ requires near continuous data between middle latitudes ($\Lambda \leq 50$ deg.) on each side of a high latitude crossing in order to establish a perturbation magnetic field baseline as described in Gary *et al.* [1994]. In addition to this requirement, we have inspected each pass to ensure that the final calculation of $S_{||}$ is made using reliable data. Ultimately, 576 passes met our criteria for the production of reliable $S_{||}$. These orbits range over all DE 2 altitudes, from about 300 km to 1000 km, and represent passes from both hemispheres. As described by *Heelis and Coley* [1988], the 90 deg. inclination orbit of the DE 2 satellite causes coverage of season to be linked to the local time coverage with dawn-dusk passes occurring predominantly in summer/winter and noon-midnight passes near the equinoxes. It should also be mentioned that the lifetime of DE 2 occurred during a period of very high solar activity. Interpretations of our data need to be made with these points in mind.

---

[1] Now at Applied Physics Laboratory, Laurel, Maryland.

Paper number 95GL00570
0094-8534/95/95GL-00570$03.00

We have binned the data by invariant latitude (Λ) and magnetic local time (MLT) and sorted according to Kp and IMF B_z conditions when possible. Each bin covers 5 deg in Λ and 1 hour in MLT. Kp sorting separates low geomagnetic activity ($0<\mathrm{Kp}\leq 3$) and high activity ($\mathrm{Kp} > 3$), and IMF sorting separates northward from southward IMF. The results are shown in polar dials representing the high latitude region above 50 deg invariant latitude using a color coded intensity scale to indicate the magnitude of $S_{\|}$. Bins which contain diamonds represent regions where we have less than 75 observations, which we have taken to be the limit for undersampling. The choice of 75 as a limit ensures that at least two passes are included, as one pass may contribute as many as 70 observations in a single bin. Bins which have no shading and no diamond represent regions for which we have no observations. IMF data is available for only 302 of the 576 orbits used in this study, thus reducing the statistics considerably when we examine the distributions under different IMF and Kp conditions. In this work we will continue to use the sign convention where downward directed Poynting flux is negative ($S_{\|} < 0$) and indicates electromagnetic energy being converted into particle kinetic energy in the flux tube below the satellite, and upward Poynting flux ($S_{\|} > 0$) indicates the generation of electromagnetic energy below the satellite.

Observations for all IMF

The results of our binning procedure for all IMF and Kp conditions are presented in Figure 1. The averaged $S_{\|}$ is everywhere downward with the largest values occurring near dusk, dawn, and local noon. The highest energy transfer rates are observed between 65 and 80 deg invariant latitude. These regions are generally colocated with the auroral zone, indicating that on average most of the Birkeland currents close locally in region 1/region 2 current sheet pairs. It is easily seen in Figure 1 that the total energy transferred into the ionosphere is greater on the dayside of the dawn-dusk meridian than on the nightside. For the variety of IMF and Kp conditions which we have investigated, the dayside integrated values exceed the nightside values by 20% to 50%.

Across the dayside between 70 and 85 deg there is a region of relatively large $S_{\|}$. Part of this region can be associated with cusp currents as well as with the average convection patterns. A region of high average electric field was observed in our results above 70 deg between 0900 MLT and 1200 MLT. This overlaps a region of enhanced magnetic field perturbation producing the "cusp" signature in $S_{\|}$ at the same location. There is a bay of smaller valued $S_{\|}$ in the premidnight sector which corresponds to relatively small values of $\mathbf{E}$ and $\delta\mathbf{B}$ in the premidnight hours. The premidnight sector showed consistently lower values of $S_{\|}$ throughout our analysis, for all IMF and Kp conditions. Comparison between some of the published studies on ion drifts [*Kelley*, 1989, and included references] and neutral winds [*McCormac et al.*, 1991, *Kelley*, 1989] as well as model results [e.g., *Thayer and Killeen*, 1993] indicate that the general circulation of the ions and the neutrals is q similar in this region. For low Kp, the same asymmetries about the noon-midnight and dawn-dusk meridians exist as for high Kp, but the magnitudes of both $\mathbf{E}$ and $\delta\mathbf{B}$, and thus $S_{\|}$, are smaller. The low Kp distribution of $S_{\|}$ is dominated by the region of elevated activity near noon. The auroral zone is well defined across the nightside in the $S_{\|}$ data as a narrow belt between 65 and 70 deg.

Observations for northward and southward IMF

Figures 2(a) and 2(b) show the results of our sorting the data by the sign of IMF B_z and for high and low Kp, with Figure 2(a) showing the case of southward IMF at high Kp and Figure 2(b) the case of northward IMF at low Kp. Many features of the distribution of $S_{\|}$ can be fairly easily reconciled with typical convection patterns associated with northward and southward IMF, and the values at high Kp can be generally described as being larger than, and located at lower latitudes from, those at low Kp. For southward IMF, the average $S_{\|}$ exhibits elevated values along the dusk and dawn convection boundaries, or auroral zones, reaching a maximum of about 12 mW/m^2 as seen in Figure 2(a). Note also a region of enhanced $S_{\|}$ extending to higher latitudes between 1000 and 1200 MLT. This region, previously identified with enhanced electric fields in the cusp, is more easily identified when the orientation of the IMF is included in the data selection. The largest bin average is between 1500-1600 MLT and 60-65 deg, and is primarily composed of five southern hemisphere orbits that occurred during magnetic storms. *Deng et al.* [1993] described some of these orbits in their study of the response of the neutral atmosphere to geomagnetic storms. The bin averaged $S_{\|}$ is quite large above 60 deg invariant latitude, peaking between 65 and 75 deg.

The interaction between the IMF and geomagnetic field for northward IMF leads to much weaker driving of the ions from magnetospheric electric fields, and the northward IMF results in Figure 2(b) show little variation below 70 deg. The largest values are about 7.3mW/m^2 and occur across the dayside in the regions where typical multiple-cell (> 2) convection patterns might exist and the general motion of the ions would oppose that of the neutrals. The regions of $S_{\|}$ above the background near dawn and dusk are also consistent with a multiple-cell convection pattern.

Observations of upward Poynting flux

Several authors have addressed the ability of neutral wind motion to generate electromagnetic energy in the lower ionosphere. This energy would be transported along magnetic field lines into the magnetosphere. As discussed in e.g., *Kelley et al.* [1991], this would result in observations of upward $S_{\|}$. In their work on assessing the role of the neutral wind dynamo in high latitude energy generation, *Thayer and Vickrey* [1992] predicted

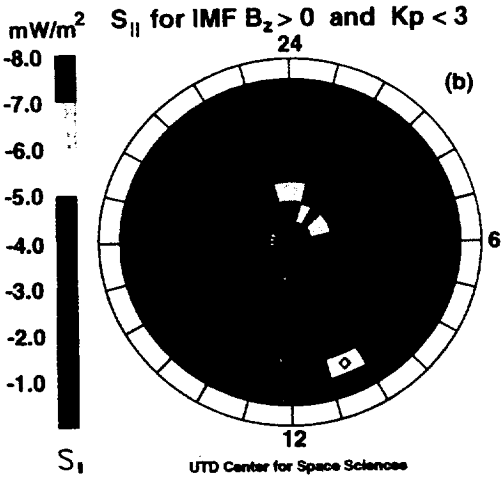

Figure 1. Polar dial showing the distribution of the average field-aligned Poynting flux ($S_{\parallel}$) in magnetic local time (MLT) and invariant latitude (Λ) above Λ=50°. The bins used in the averaging cover 1 hour in MLT and 5 degrees in Λ. The data are for all IMF orientations and Kp values, averaged over 570 DE 2 high latitude passes.

regions near convection reversals to be likely locations for upward Poynting flux observations. We have indeed observed individual cases where this may be the case. The variablity in location of the convection reversal leads these cases to be statistically unobservable. We have not observed any locations in the high-latitude ionosphere which exhibited upward Poynting flux over a relatively long term average. However, we have taken all observations of upward $S_{\parallel}$ and performed the same binning and sorting of the data as was applied to the overall observations in order to report on the distribution and occurrence of upward Poynting flux. Some of these results are presented in Figure 3. Perhaps the most obvious point to be made from the figure is that the average magnitude of upward Poynting flux is quite small under all conditions, with no single bin greater than 2.25 mW/m^2. Such small average values are in line with the modelling of *Thayer and Vickrey* [1992] and *Deng et al.* [1993]. All of our observations above the nominal uncertainty level of 0.5 mW/m^2 occur above 65 deg. invariant latitude.

Figure 3 depicts the distribution of upward $S_{\parallel}$ for all IMF and high Kp. The largest bin averages occur on the dawnside of the noon-midnight meridian, and are almost entirely composed of southward IMF observations. On the duskside, the occurrences are of smaller magnitude and seem to be sporadically located. There are no significant observations above 85 deg, few below 65 deg, and observations of upward $S_{\parallel}$ near noon are noticeably absent. For low Kp, observations of substantial (> 1mW/m^2) upward $S_{\parallel}$ averages all but vanish. The early morning hours which show the largest upward $S_{\parallel}$ at high Kp exhibit insignificant average values at low Kp.

It is apparent that, while observations of upward $S_{\parallel}$ occur over most of the high latitude ionosphere, they are not widely significant in an average sense. Bin averages greater than 0.5 mW/m^2 are rare, and it is possible that most could vanish if a substantially larger data set was

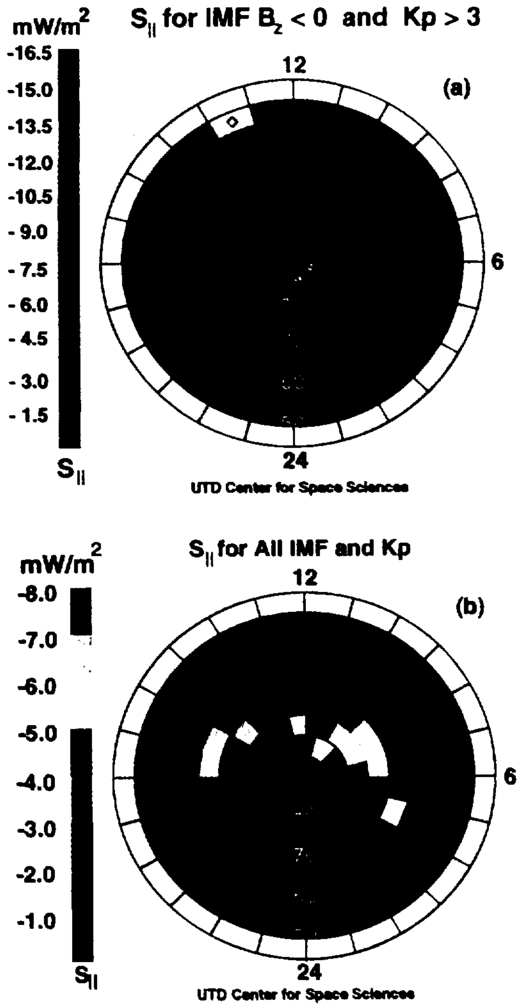

Figure 2. Results of sorting the bin averaged $S_{\parallel}$ data by southward and northward IMF for high and low Kp, in the same format as Figure 1 but with a different scale. Bins with no data are not colored. Bins with fewer than 75 measurements are shown with a diamond. (a) results for southward IMF and Kp>3, representing data from 92 high latitude passes. (b) results for northward IMF and Kp<3, representing data from 117 passes.

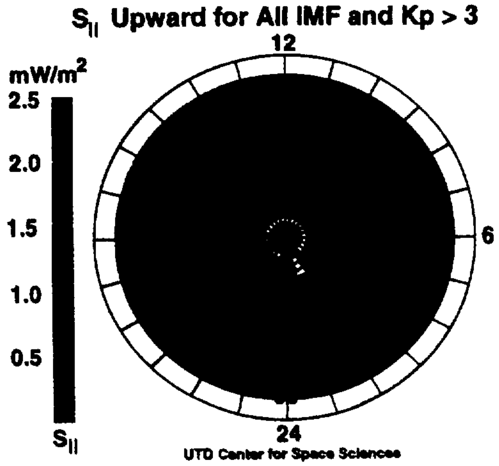

Figure 3. Results of the bin averaged upward Poynting flux in the same format as Figure 1. Only measurements of $S_{\parallel}$ >0 have been included in the averages for all IMF and Kp>3, representing data from 147 passes.

employed. A likely exception would be the region between 70-80 deg near 0300 MLT. We have examined the frequency of occurrence of upward $S_{||}$ greater than 0.5 mW/m^2 , and in this region it exceeds 20% for southward IMF. The occurrence frequency is determined by taking the ratio of the number of observations for which $S_{||} > 0.5$ mW/m^2 to the total number of observations in each bin. Detailed examination of the binned orbits in this region does not suggest that the upward Poynting flux observations are suspect. Few regions show an occurrence frequency greater than 10%, but even this frequency is somewhat remarkable. Examination of separate orbits reveals that the regions of appreciable upward Poynting flux are associated with field-aligned currents in the polar cap which are distinctly smaller in scale size than the large scale region 1 and region 2 current distributions. Such field-aligned currents are likely to arise from divergences in the horizontal ionospheric currents which should exist whenever the thermospheric winds become the dominant driver of electromagnetic energy.

The interpretation of upward Poynting flux observations as being largely due to neutral wind dynamo action is certainly not unambiguous. However, the neutral gas obtains its highest velocities during southward IMF and high Kp conditions in just this region. If the field lines connecting the predawn ionosphere to the magnetosphere are open during these observations, then they must extend far into regions where the magnetosheath plasma is super-Alfvenic. Communication between the magnetospheric driver and the ionosphere would be effectively severed. This argues for a weak connection along open field lines between the magnetospheric electric field driver and the ionospheric load.

Conclusion

Our work in determining the distribution of the energy transfer rate in the high latitude ionosphere using observations of the field-aligned Poynting flux $S_{||}$ has produced the following results:

1) $S_{||}$ is downward everywhere on average;

2) for southward IMF, a two-cell convection pattern is evidenced with the greatest $S_{||}$ occurring in the auroral zones at dawn and dusk, with an "offset" cusp region at higher latitudes just before noon;

3) for northward IMF, a multiple-cell convection pattern is evidenced with the greatest $S_{||}$ occurring near noon where we might expect the ion and neutral gas bulk flows to have opposite directions;

4) upward Poynting flux may be observed at all locations but at generally small values, averaging to less than 1 mW/m^2 , and never with sufficient frequency to dominate a long term average;

5) there is a region of significant upward Poynting flux generated in the predawn polar cap with an average of greater than 2 mW/m^2 , although the net $S_{||}$ is downward when all observations are averaged. Observations of upward $S_{||}$ account for more than 20% of the total observations for southward IMF with Kp>3 in this region;

This work is supported at the University of Texas at Dallas by NASA contract No. NAGW-3508 and by Air Force Geophysics Directorate contract F19628-93-K-0008, and at SRI International by NASA contract No. NAS5-31214.

References

Banks, P. M., Observations of Joule and particle heating in the auroral zone, *J. Atmos. Terr. Phys.*, *39*, 179, 1977.

Deng, W., T. L. Killeen, A. G. Burns, R. G. Roble, J. A. Slavin, and L. E. Wharton, The effects of neutral inertia on ionospheric currents in the high latitude thermosphere following a geomagnetic storm, *J. Geophys. Res.*, *98*, 7755-7790, 1993.

Foster, J. C., J.-P. St-Maurice, and V. J. Abreu, Joule heating at high latitudes,*J. Geophys. Res.*, *88*, 4885-4896, 1983.

Gary, J. B., R. A. Heelis, W. B. Hanson, and J. A. Slavin, Field-aligned Poynting flux observations in the high latitude ionosphere, *J. Geophys. Res.*, *99*, 11417-11427, 1994.

Heelis, R. A., and W. R. Coley, Global and local Joule heating effects seen by DE 2, *J. Geophys. Res.*, *96*, 7551-7557, 1988.

Kelley, M. C., *The Earth's Ionosphere*, Academic Press, New York, 1989.

Kelley, M. C., D. J. Knudsen, and J.F. Vickrey, Poynting flux measurements on a satellite: A diagnostic tool for space research., *J. Geophys. Res.*, *96*, 201-207,1991.

McCormac, F. G., T. L. Killeen, and J. P. Thayer, The influence of IMF B_y on the high-latitude thermospheric circulation during northward IMF, *J. Geophys. Res.*, *96*, 115-128,1991.

Thayer, J. P., and T. L. Killeen, A kinematic analysis of the high-latitude thermospheric neutral circulation pattern, *J. Geophys. Res.*, *98*, 11,549-11,565, 1993.

Thayer, J. P. and J. F. Vickrey, On the contribution of the thermospheric neutral wind to high-latitude energetics, *Geophys. Res. Lett.*, *19*, 265, 1992.

Vickrey, J. F., R. R. Vondrak, and S. J. Matthews, Energy deposition by precipitating particles and Joule dissipation in the auroral ionosphere, *J. Geophys. Res.*, *87*. 5184-5196, 1982.

J.B. Gary, John Hopkins Applied Physics Laboratory, Laurel, Maryland.

R.A. Heelis, University of Texas at Dallas, Richardson, Texas.

J.P. Thayer, SRI International, Menlo Park, California.

(received August 8, 1994; revised December 22, 1994; accepted January 20, 1995.)

APPENDIX D

Thayer, J.P., "Height-resolved Joule heating rates in the high-latitude E region and the influence of neutral winds," submitted to the *Journal of Geophysical Research.*

HEIGHT-RESOLVED JOULE HEATING RATES IN THE HIGH-LATITUDE E REGION AND THE INFLUENCE OF NEUTRAL WINDS

J.P. Thayer

SRI International, Menlo Park, California

For submission to *Journal of Geophysical Research*

March 1997

ABSTRACT

Height-resolved and height-integrated estimates of the Joule heating rate in the high-latitude E region that include the effects of the neutral wind have been derived from measurements made by the Sondrestrom incoherent-scatter radar. Analyzed in detail are two Sondrestrom radar data sets from World-Day experiments that represent solar minimum, daytime conditions with periods of geomagnetic activity. These measurements show much more structure in the height-resolved Joule heating rate when neutral winds are included in the analysis. The neutral wind impact on the height-resolved Joule heating rate was present during all periods of elevated Joule heating and displayed an altitude-dependent influence that led to both positive and negative contributions within the E region. Most often, the wind impact was to create a much narrower region of Joule heating. The influence of the neutral wind on the height-integrated Joule heating rate from 90 to 140 km was significant, at times, with observed reductions of 40% and observed enhancements of as much as 400%. However, the height-integrated Joule heating rate often did not reflect the degree of neutral wind influence on the local Joule heating rate because the altitude-dependent behavior of the wind would tend to cancel out during the height-integration process. Evidence of electric field behavior controlling the neutral wind influence on the Joule heating rate was also observed. During directional changes in the electric field, the neutral winds tended to enhance the Joule heating rate while directionally steady electric fields resulted in an overall reduction of the Joule heating rate by the neutral wind.

1. INTRODUCTION

Much work has been done on quantifying the dissipation rate of electromagnetic energy in the ionosphere–thermosphere system through estimates of the Joule heating rate by spacecraft and ground-based measurements [i.e., Foster et al., 1983; Rich et al., 1987, 1991; Heelis and Coley, 1988; de la Beaujardiére et al., 1991; Baumjohann and Kamide, 1984]. These contributions have largely been in the form of height-integrated Joule heating rates that quantify the dissipation rate of electromagnetic energy exchanged between the ionosphere and magnetosphere. Various assumptions are used in each technique, however, a common assumption is to neglect the neutral winds and to presume that the height distribution of the Joule heating rate is described solely by the Pedersen conductivity. This assumption is invoked not because the neutral winds are considered negligible but because of the large uncertainty in describing the altitude distribution of the neutral wind through the E and F region. Modeling efforts using the NCAR Thermosphere–Ionosphere General Circulation Model (NCAR–TIGCM) have demonstrated that the neutral winds are, at times, significant contributors to the height-integrated Joule heating rate [e.g., Thayer et al., 1995; Lu et al., 1995]. However, high-latitude E-region neutral dynamics are still poorly understood and difficult to represent adequately in a model due to uncertainties in representing tidal forcing from below and magnetospheric forcing from above. Thus, the altitude distribution of the electromagnetic energy dissipation rate in the ionosphere and the role of the neutral winds still remain as fundamental questions. The difficulty in addressing such issues has been due to the difficulty in making measurements of the vertical distribution of the electrodynamic parameters, such as currents, electric fields, conductivities, and neutral winds, needed to estimate completely the Joule heating rate. The added difficulty is the various interdependencies amongst these parameters, thus requiring near simultaneous, height-resolved observations of these parameters for proper assessment of the Joule heating rate.

Incoherent-scatter radar measurements provide the most comprehensive measurement set for estimating the local current, electric field, conductivity, and neutral wind within the E region for extended periods. These local, high-resolution measurements of E-region electrodynamic parameters allow for the distribution of electromagnetic energy dissipation within the E region to be elucidated. This was first demonstrated by Brekke and Rino [1978] where they determined the E region currents and conductivities from incoherent-scatter radar measurements at Chatanika, Alaska, using a multipulse scheme that provided sufficient (~10 km) resolution of the E region, and evaluated empirically the local and height-integrated Joule heating rate under active conditions. However, the poor signal statistics associated with this mode limited the observations to times of only very active conditions. A more typical approach using the radar has been to determine the electric field and Pedersen conductivity throughout the E and F region using long pulse schemes and either considering local effects by the neutral wind [de la Beaujardiére et al., 1991], setting the neutral wind to zero [Banks, 1977], or using a reference wind model [Vickrey et al., 1982]. Although this more typical approach has the advantage of operating under less active conditions, the poor E-region resolution, lack of adequate representation of the neutral

wind, and pulse smearing effects limit the efficacy of such an approach for studies concerned with the altitude distribution of the Joule heating rate.

Since the earlier work, improvements to incoherent-scatter radars—for example, new or improved pulse schemes—have enhanced studies of E-region electrodynamics. Recently, Brekke et al. [1990] described improvements to EISCAT measurements and the ability to determine ionospheric currents at high temporal and spatial resolution using a multipulse scheme. Kamide and Brekke [1993] presented additional EISCAT results on the height distribution of E-region currents within the auroral electrojets. EISCAT has further improved their E-region capabilities by employing an alternating code scheme that provides range resolution similar to their multipulse scheme but with improved signal statistics. Similar high-resolution operating modes have been implemented at the Sondrestrom, Greenland, incoherent-scatter radar with the alternating code algorithm [Lehtinen, 1986; Lehtinen and Haggstrom, 1987] enabling improved measurements of E-region parameters at an altitude resolution of 3 km.

The improved capability of the Sondrestrom radar allows for a detailed analysis of E-region electrodynamics. More specifically, it permits the direct assessment of the height-resolved and height-integrated Joule heating rate in the high-latitude E region that includes neutral wind effects. As a result, this paper presents the first height-resolved estimates of the E-region Joule heating rate over Sondrestrom at such high resolution and evaluates the contribution of the neutral wind to the local as well as the height-integrated Joule heating rates. Two 24-hour MLTCS (Mesosphere Lower Thermosphere Coupling Study) World-Day radar experiments (August 5, 1993 and May 2, 1995) that correspond to solar minimum, daytime periods of moderate to active geomagnetic conditions are used in the analysis to evaluate the Joule heating rates. The approach taken is presented in the following section where the Joule heating rate expressions are provided and the neutral wind influence is clarified. This is followed by a section that describes the data analysis of the radar measurements and presents detailed analysis of the electrodynamic parameters derivable from the radar. A discussion section examines the Joule heating rate for the two radar experiments in detail and assesses the role of the neutral winds. The conclusion section summarizes the findings from this study which, in part, indicate much more structure in the height-resolved Joule heating rate when neutral winds are included in the analysis.

2. APPROACH

Many investigations of the Joule heating rate have used the expression

$$q_j = j_\perp \bullet E'_\perp = \sigma_p E'^2_\perp = \sigma_p \left(E_\perp + u_n \times B\right)^2 \qquad (1)$$

and have required the need to make some approximations to the calculation. This is due to the fact that to evaluate accurately the Joule heating rate by (1) requires knowledge of the electric field and the distribution of the neutral wind and conductivity with height (requiring collision frequency and gyrofrequency calculations based on plasma and neutral composition). Quite often the neutral wind in (1) is assumed to be zero resulting in the approximate expressions for the local and height-integrated Joule heating rate given, respectively, as

$$q_j^E = \sigma_P E^2 \quad ; \quad Q_j^E = \int_{90}^{Z_{Upper}} \sigma(z)_P E^2\, dz = \Sigma_P E^2 \ . \qquad (2)$$

Another approach to estimating the Joule heating rate that was discussed, for example, by Cole [1962, 1975] is the expression

$$q_j = j_\perp \bullet E'_\perp = \frac{j_\perp^2}{\sigma_c} \quad ; \quad Q_j = \int_{90}^{Z_{Upper}} \frac{j(z)_\perp^2}{\sigma(z)_c} dz \ , \qquad (3)$$

where σ_C is the Cowling conductivity given by

$$\sigma_c = \sigma_P + \frac{\sigma_H^2}{\sigma_P} \qquad (4)$$

with σ_P and σ_H being the symbols for the local Pedersen and Hall conductivity, respectively. The presence of the Cowling conductivity in (3) is solely due to the fact that the magnitude of the horizontal current, $|j_\perp|$, can be written as

$$|j_\perp| = \left(\sigma_P^2 + \sigma_H^2\right)^{1/2} |E'_\perp|$$

$$|j_\perp| = \left[\sigma_P\left(\sigma_P + \frac{\sigma_H^2}{\sigma_P}\right)\right]^{1/2} |E'_\perp|$$

$$|j_\perp| = \left(\sigma_P \sigma_c\right)^{1/2} |E'_\perp| \quad . \qquad (5)$$

Solving for $E'_\perp$ and substituting into (1) gives the Joule heating rate expressed by (3).

Because this expression involves the difficult measurement of the local current density and the Pedersen and Hall conductivity in the E region, many investigations have not used this approach. However, using (3) has the advantage that the effects of the neutral wind on the Joule heating rate are inherently contained within the current density measurement and do not have to be determined explicitly. The approach taken is to use the Sondrestrom radar measurements to evaluate the height-resolved and height-integrated Joule heating rates using (2) and (3), and

compare their relative differences to elucidate the neutral wind impact. Additional analysis of the neutral wind behavior related to the observed differences in the two Joule heating rates will be carried out by directly deriving the neutral wind from the radar measurements.

Although the local difference between the Joule heating rates estimated by (2) and (3) can show the impact of the neutral wind, the neutral wind magnitude and direction cannot be uniquely determined from these two estimates alone. Yet, there are conditions when the observed differences between the two calculations constrain the possible combinations of wind magnitude and direction. It is, therefore, useful for further interpretation to express what the difference between the two approaches represents and how well the neutral wind can be quantified based only on measurements of q_j^E and q_j.

For the local Joule heating rate, the difference between q_j and q_j^E can be expressed as

$$\Delta q(z) = j_\perp(z)\bullet E'_\perp(z) - \sigma_p(z)E_\perp^2 = \sigma_p(z)\left[(u_n(z)\times B)^2 - 2u_n(z)\bullet(E\times B)\right] . \tag{6}$$

This expression can be further simplified by using direction cosines such that

$$\Delta q(z) = \sigma_p(z)|B|\left[|u_n(z)|^2|B| - 2|E||u_n(z)|\cos(\theta)\right] , \tag{7}$$

where the symbol | | represents the magnitude of the vector and the $|u_n(z)|\cos(\theta)$ term represents the component of the neutral wind in the E×B direction. From (6) it can be recognized that by simply having a non zero neutral wind, irrespective of direction, the local Joule heating rate will be enhanced. This would lead to a positive difference between q_j and q_j^E. From (6) the only way the net impact of the neutral wind can reduce the Joule heating rate is if there is a component of the neutral wind in the E×B direction. To express this analytically, (7) can be written in the form of a quadratic equation and solved for the magnitude of the neutral wind using the full range of possible angles for the wind direction with respect to the E×B direction. The quadratic expression from (7) becomes

$$|u_n(z)|^2|B| - 2|E||u_n(z)|\cos(\theta) - \frac{\Delta q(z)}{\sigma_p(z)|B|} = 0 \tag{8}$$

and its solution may be written as

$$|u_n(z)| = \frac{|E|\cos(\theta)}{|B|} \pm \frac{\sqrt{|E|^2\cos^2(\theta) + \frac{\Delta q(z)}{\sigma_p(z)}}}{|B|} . \tag{9}$$

Only positive, real roots are appropriate when describing the behavior of the neutral wind magnitude. It can be shown that a small positive discriminant in (9) leads to the smallest range of possible angles centered on the E×B direction and the smallest range in neutral wind magnitude. Thus, when $\Delta q(z)/\sigma_P(z)$ is negative and close but less than $|E|^2$, the problem is constrained and the magnitude of the neutral wind and its angle are more isolated. However, when $\Delta q(z)$ is

positive the result is non-unique as all angles and a range of magnitudes may provide the correct answer. This behavior will be illustrated in the results section.

Radar Estimates of Electrodynamic Parameters

In general, it is difficult to measure all of the required electrodynamic parameters simultaneously to study adequately E-region electrodynamics. Considerable progress has been made over the years toward improving the measurement of these quantities with the Sondrestrom radar. The recent implementation of the alternating code scheme (with 3 km range resolution) in combination with simultaneous long pulse measurements (with 48 km range resolution) at Sondrestrom provides a radar data set suitable for electrodynamic studies of the E and F region. This combination of waveforms is the transmitter mode used throughout the experiments presented in this study.

To apply the expressions described above to incoherent-scatter radar measurements it is best to reduce the equations in terms of the most basic parameters derived directly from the radar. This simplifies the error propagation and, although some equations may not be intuitive, they illustrate directly the variables that are measured versus those that are modeled or approximated. For example, the local current density may be written (assuming charge neutrality and equal ion species velocities) as

$$j = en_e\left(v_i - v_e\right) \quad , \tag{10}$$

where e is the electronic charge, n_e is the electron density, v_i, is the E-region ion drift velocity, and v_e is the electron drift velocity (assumed equal to the F-region ion drift). All these quantities are directly derivable from the radar measurement. Using the coordinate system with the x-direction positive magnetic east, the y-direction positive north, and the z-direction positive upward along the magnetic field, the east and north components of the current density may be written as

$$\begin{aligned} j_x(z) &= en_e\left(v_x(z) + \frac{E_y}{B}\right) \\ j_y(z) &= en_e\left(v_y(z) - \frac{E_x}{B}\right) \quad . \end{aligned} \tag{11}$$

Using propagation of errors and ignoring correlation terms, the relative uncertainty of the current density is given by

$$\frac{\sigma_j}{j} = \sqrt{\frac{\sigma_{n_e}^2}{n_e^2} + \frac{\sigma_{v_i}^2}{(\Delta v)^2} + \frac{\sigma_{v_e}^2}{(\Delta v)^2}} \tag{12}$$

with σ representing the standard deviation and Δv corresponding to the drift velocity difference between the E-region and F-region ion drifts for a particular E region altitude. Thus, the error in the current estimation grows as the differential velocity between the E and F region drifts gets

small. This limits the ability to determine the current density accurately above the E region using this approach.

For the local Joule heating rate, (3) becomes

$$j \bullet E' = q_j = \frac{j^2 B\Omega_i}{en_e \nu_{in}} = \frac{en_e(v_i - v_e)^2 B\Omega_i}{\nu_{in}} \quad , \tag{13}$$

where B is the Earth's magnetic field (assumed constant with height), Ω_i is the ion gyrofrequency, and ν_{in} is the modeled ion-neutral collision frequency. The ion-neutral collision frequency depends on the collision terms for NO^+, $O_2{}^+$, O^+ in a neutral atmosphere determined by MSIS-90 of N_2, O_2, O (see Schunk and Nagy [1980]). The total ion-neutral collision frequency is determined by the sum of the collision frequencies after weighting each collision frequency by the ratio of the specific ion density to the total ion density. The number densities of the different ionic species are obtained using an empirical model of $[O^+]$ / n_e [Kelly and Wickwar, 1981] and an assumed molecular composition of 75% NO^+ and 25% $O_2{}^+$. The relative error for the local Joule heating rate is given as

$$\frac{\sigma_{q_j}}{q_j} = \sqrt{\frac{\sigma_{n_e}^2}{n_e^2} + \frac{\sigma_{\nu_{in}}^2}{\nu_{in}{}^2} + \frac{4\sigma_j^2}{j^2}} \quad . \tag{14}$$

Here, the error in the Joule heating rate is most sensitive to errors in the current density and, therefore, calculations of the Joule heating rate using this approach are also limited to E-region altitudes.

Deriving the Joule heating rate from radar data using (3) has the advantage that the explicit calculation of the neutral wind is not required. However, as was shown by (9), the actual behavior of the wind cannot be determined uniquely from the difference between the two Joule heating approaches. Therefore, the neutral wind is derived directly from the radar measurement for interpretation of the observed behavior in the Joule heating rates.

Rino et al. [1977] describe the approach used to derive the neutral wind from the radar measurements. The height-dependent neutral wind velocity is deduced from the steady-state ion equation of motion applied to E-region altitudes and takes the form

$$\begin{aligned} u_x(z) &= v_x(z) - \frac{\Omega_i}{\nu_{in}}\left(\frac{E_x}{B} - v_y(z)\right) \\ u_y(z) &= v_y(z) - \frac{\Omega_i}{\nu_{in}}\left(\frac{E_y}{B} + v_x(z)\right) \quad . \end{aligned} \tag{15}$$

In general, the limiting factor in deriving the neutral wind and using it in (1) has been the dependency of the neutral wind on the collision frequency model, as shown by Rino et al. [1977] and Johnson [1990], along with limitations in certain radar pulse schemes. The decreasing collision frequency with height amplifies any error in the measured value of the electric field

and/or drift velocity at upper E-region altitudes. However, as shown by Johnson [1990], there are configurations where the collision frequency has little impact on the derived wind. In addition, the alternating code waveform used in this study has improved signal statistics over multipulse schemes providing more accurate estimates of the ion drift velocity in the upper E region. Shown in the next section will be that the neutral wind estimates using (15) can give, at times, reliable estimates up to altitudes of 140 km with some sensitivity to collision frequency. The calculation of the Joule heating rate using (13) and the Pedersen conductivity used in (2) are also sensitive to the model collision frequency. An assessment of these dependencies will be discussed in a later section.

3. RESULTS

Presented are all of the electrodynamic properties derivable from the radar measurements needed in the evaluation of the E-region Joule heating rate for one particular period of observations, August 5, 1993, between 08:00 and 22:00 UT. Subsequent analysis of other data will include only the plots needed to evaluate adequately the derived Joule heating rate with the understanding that the same process used in analyzing the August 5, 1993 observations was applied to these data. The analysis begins by illustrating as the ion drift velocity, electron density, and derived electric field for this day. Then the current density and conductivity properties of the E region are analyzed, which will lead into estimating the Joule heating rate.

On August 5, 1993, the Sondrestrom radar performed a three-position radar experiment (one position directed parallel to the magnetic field at 141° azimuth, 80° elevation, and the others 120° apart at 70° elevation) that employed the alternating code scheme on one frequency and a long pulse scheme on the other frequency. Each position was integrated for 5 minutes and for two range gates, giving a range resolution of 6 km in the E region. The line-of-sight ion velocities throughout the E and F region are determined from these measurements and resolved at each gate into a geomagnetic coordinate system with the x-direction positive magnetic east, the y-direction positive north, and the z-direction positive upward along the magnetic field. The technique of combining the three-position data is discussed by Johnson [1990]. A general assumption in forming the resolved velocity is that the velocity vector does not vary significantly over the spatial region described by the three-position measurement. Also, it is not assumed that each line-of-sight remains fixed for the interval required to make a three-position measurement, but rather, the line-of-sight quantities are allowed to vary linearly in time.

The resolved electric field and the E-region ion drift velocities resulting from these three-position measurements and the mean E-region electron density are shown in Figures 1 and 2. The observations are representative of dayside auroral oval measurements covering the magnetic local time period from 05:49 to 19:49 with the solar zenith angle ranging from 82.8° to 77.5°, respectively, with a minimum solar zenith angle of 50.1°. The electric field is presented in Figure 1 in components of direction and magnitude, which will be useful when discussing the estimates for the Joule heating rate. The one-sigma error in the electric field is no greater than ± 2mV/m throughout the experiment. The electric field direction shows a typical two-cell ion convection with nearly equal behavior of the electric field magnitude on either side of the noon meridian. This electric field results in eastward ion drifts in the morning sector, northward ion drifts (antisunward) in the noontime sector, and northwestward ion drifts in the evening sector, as illustrated in Figure 2 by the ion drifts in the upper E region drifting essentially in the E×B direction. The E-region ion velocities in Figure 2 rotate clockwise in the direction of the electric field with decreasing height from the F region to the lower E region as the ratio of the ion gyrofrequency to the ion-neutral collision frequency decreases. The electron densities in Figure 2 are relatively uniform throughout the E region. Note that the electron densities are temperature

corrected above 120 km, while below this altitude it is assumed that the ion and electron temperatures are equal.

The E-region current density for this data set is shown in Figure 3. The current density was determined by (11) using the electric field data presented in Figure 1 and the electron density and ion drift data presented in Figure 2. As discussed for example by Brekke et al. [1990], the E-region current density will be rotated 90° clockwise from the ion drift velocity at any height as long as the neutral wind and electric field parallel to the magnetic field can be ignored and only one ion species is present. By comparison with the ion drifts in Figure 2, one can see that the current density direction in Figure 3, in general, follows this rule. However, there are regions where the current density is not 90° to the ion drift; these significant departures are associated to neutral wind effects. This will be more clearly demonstrated in the analysis of the Joule heating rate.

Case I – Joule Heating Rates for August 5, 1993

Presented in Figure 4 is a comparison between height-resolved Joule heating rates derived from the radar data for August 5, 1993, using (2) and (13) and their height-integrated quantities integrated over E-region altitudes from 90 to 140 km. The difference plot relates to (6) given in section 2 and, therefore, provides an indication of the neutral wind influence on the Joule heating rate.

Height-Integrated Data

Discussed first is the height-integrated Joule heating rates presented in Figure 4a where the height-integrated Joule heating rate (Q_j^E) excluding neutral winds, depicted by the solid black line, is compared with the height-integrated Joule heating rate (Q_j) including neutral winds, depicted by the solid orange line. An error check is made on the height-integrated Joule heating rates (Q_j) with values having a percent error exceeding 50% forced to zero. Found here are two active periods during the experiment occurring near 10:00 UT and 18:00 UT. At and after 10:00 UT, relatively good agreement between the two approaches is seen indicating that overall the neutral wind effect on the height-integrated Joule heating rate is of minor significance during this time. However, prior to 10:00 UT, Q_j exceeds Q_j^E indicating a neutral wind enhancement to the height-integrated Joule heating rate. This contribution occurs during times of changing electric field direction (see Figure 1a) while after 10:00 UT the electric field direction is steadier. Later, between 13:00 UT and 15:00 UT, the neutral winds contribute again to enhance the Joule heating rate during a time when the electric field direction is transitioning from primarily southward to northward.

The active period near 18:00 UT results in the largest discrepancy between height-integrated quantities, with the neutral winds acting to reduce the height-integrated Joule heating rate by over 40% near peak activity in the electric field magnitude. The impact of the neutral wind to reduce the Joule heating rate is dependent on the time history of the neutral wind forcing.

Referring to Figure 1a, the time period near 18:00 UT shows the electric field magnitude increased but the direction of the electric field remained constant since 15:00 UT. This would indicate that the neutral winds in the F region and topside E region have been forced by ion drag over at least a three-hour period to flow in the direction of the ion drift and effectively reduce the Joule heating rate when the electric field magnitude increased.

Height-Resolved Data

The height profiles used to determine the height-integrated Joule heating rates are provided in Figure 4b. Gaps in the data represent times of poor signal statistics. In this figure, the height-resolved Joule heating rates (q_j^E), using (2), are presented in the bottom panel and the height-resolved Joule heating rates (q_j), using (13), are presented in the top panel. The middle panel represents the difference between the top and bottom panels to highlight the comparison and illustrate the local effect of the neutral wind. A negative difference (blueward) means the wind is reducing the local Joule heating rate while a positive difference (redward) means the wind is enhancing the local Joule heating rate. The dark yellow to light green transition in the color bar marks the transition between positive and negative differences.

The shape of the profiles shown in the bottom panel reflect the vertical distribution of the Pedersen conductivity as the electric field is assumed to map without attenuation through the E region. This shape is modified in the top panel by the effects of neutral winds contained within the current density measurement as the conductivity-weighted neutral wind contributes to the local Joule heating rate in an altitude-dependent manner. Prior to 10:00 UT, the middle panel shows mostly positive differences in the upper E region indicating local wind enhancements of the Joule heating rate. This upper E-region contribution is the reason for the enhancement in the height-integrated Joule heating rate shown in Figure 4a during this time. After 10:00 UT, weakly negative contributions in the lower E region and weakly positive contributions in the upper E region result in little influence of the neutral wind on the height-integrated Joule heating rate. Although this was recognized in the height-integrated data, it is shown by the height-resolved measurement that it is a cancellation of wind during the height-integration process that makes it insignificant, not the fact that the wind is simply negligible in the E region.

Near 18:00 UT, the middle panel of Figure 4b shows a strong negative difference in the upper E region becoming moderately positive in the lower E region near 117 km. This would indicate that the wind is rotating in altitude as is typically the case in the E region. The negative difference on the topside indicates the neutral winds are moving in an E×B direction, or, equivalently in the direction of the F-region ion drift. This neutral flow has the effect of significantly reducing the local Joule heating rate in the upper E region. As the altitude decreases the neutral winds begin to rotate and enhance the Joule heating rate in the lower E region. This enhancement can be seen in the middle panel by the positive difference depicted in red and by the more localized Joule heating rate in the top panel peaking at 117 km with a half-width of only about 12 km. The localization of the Joule heating rate in altitude is an important effect

caused by neutral winds, which is not recognized in the height-integrated quantity. In fact, the height-integrated estimates by themselves could be mistakenly interpreted as an overall reduction in Joule heating throughout the column when instead the Joule heating is simply being enhanced in a more local altitude regime by the neutral wind. Moreover, the upper E-region winds are reducing the local Joule heating rate by more than 75% during this time while the lower-E region winds are enhancing the Joule heating rate by nearly 50% at the peak. Therefore, the neutral winds are playing a larger role locally than indicated by the overall 40% reduction observed in the height-integrated Joule heating rate. This is the first indication of such an event and the impact of such a localized heat source on the ionosphere–thermosphere needs further evaluation.

From estimates of q_j and q_j^E, the general direction of the neutral wind required to produce the observed changes in the E-region Joule heating rate during the penetration event near 18:00 UT have been crudely identified. This behavior was described analytically in section 2 by (8); shown in Figure 5 is the solution to (8) using height-resolved radar data taken at 17:43 UT (near the time of maximum reduction in the height-integrated Joule heating rate). The plot represents the positive real roots of the neutral wind magnitude for all angles that may satisfy the local difference between q_j and q_j^E weighted by the Pedersen conductivity at each altitude in the E region. The color code identifies the altitude of each curve and the zero angle represents the E×B direction at this time with increasing angles representing counterclockwise rotation. For this particular profile, the positive roots at 145.6 km are most constrained in angle with a range of only ±20°. Thus, although the magnitudes cover a broad range of possibilities, the direction of the neutral wind can be relatively well identified. The next three altitudes (coded orange, yellow, and light green) result in the same roots with their curves nearly identical and difficult to distinguish on the plot. Again, the required direction of the neutral wind is well constrained to within a range of angles of ±30°. As $\Delta q(z)$, scaled by the Pedersen conductivity, becomes less negative with decreasing height, a broader range of angles and magnitudes become possible solutions and, by 117 km and below, all angles and a large range of wind magnitudes are conceivable. These analytical solutions follow the general discussion provided above and illustrate the range of values possible depending on whether $\Delta q(z)$ is positive or negative.

Also plotted in Figure 5 is the estimate of the neutral wind magnitude and angle with respect to the E×B direction, depicted by the star symbol, derived using the steady-state ion momentum equation approach and solving for the neutral wind using (15). At all altitudes, the derived wind magnitude and angle from this approach fall very close to the specific roots needed to reduce $\Delta q(z)$ to zero. This would indicate that, for the collision frequency model used, the neutral wind estimate is representative of the actual wind behavior throughout the E region. An insert of the neutral wind distribution with height in Figure 5 shows more clearly the behavior of the neutral wind with altitude. Here, the wind components are displayed with positive magnitudes corresponding to eastward and northward. As indicated in both graphs of Figure 5, the wind is rotating in a counterclockwise direction with decreasing altitude, starting in the E×B direction of the northwest in the upper E region and ending in the southward direction in the

lower E region. The magnitude of the wind significantly decreases with decreasing altitude as the wind speed is near 1200 m/sec at 145.6 km, reduces to near 400 m/sec by 123.0 km, and eventually drops below 50 m/sec at and below 106 m/sec.

CASE II – Joule Heating Rates for May 2, 1995

The same analysis in case I was performed on radar data taken on May 2, 1995. The mode was identical to the August 5, 1993 data set and the electric field direction and magnitude for this day are presented in Figure 6. The electric field behavior throughout this day is quite variable and, prior to 4:00 UT on this day (not shown), the electric field was strongly northeastward for three hours and, at times, exceeded 100 mV/m. This complex behavior in the electric field is reflected in the variability of the Joule heating rate presented in Figure 7. The analysis for the Joule heating rate is the same as above and the comparison between the two forms for the height-integrated and height-resolved quantities are presented in Figure 7a and b, respectively. The panels in Figure 7 are of the same format as those presented in Figure 4. The break in the height-integrated data in Figure 7a between 6:00 and 7:00 UT and the lack of variability in the height-resolved estimates in Figure 7b during these times is due to a significant drop in the electron density resulting in little Joule heating and poor signal statistics. This corresponds to a time when the relative error in the height-integrated Joule heating (Q_j) exceeded 50% and the height-integrated and height-resolved values are forced to zero.

Height-Integrated Data

The height-integrated quantities for this day in Figure 7a show variable Joule heating occurring between 4:00 and 10:00 UT followed by an extended period of enhanced Joule heating between 11:00 and 16:00 UT. During the period between 4:00 and 10:00 UT, the estimate of the height-integrated Joule heating rate, Q_j, often exceeds the estimate, Q_j^E, indicating that the overall impact of the neutral winds are to enhance the height-integrated Joule heating rate. Within this time frame, the electric field magnitude peaks a number of times and then gradually reduces, as shown in Figure 6. However, prior to this time period the electric field direction changed from northeastward to a southwestward direction with lesser but significant directional changes throughout the period. This supports the observation made in the previous data set that during directional changes in the electric field the neutral wind often contributes to enhance the height-integrated Joule heating rate.

After 11:00 UT to about 14:30 UT the height-integrated Joule heating rate intensified. During this time the direction of the electric field remained consistently southward while the electric field magnitude increased. Also during this time, both estimates of the Joule heating rate increased, with the Q_j estimate typically less than the Q_j^E estimate. A similar result was found in the previous case under a strong but directionally stable electric field. The Joule heating rate calculations following 14:30 UT are of particular interest as the magnitude of the electric field, shown in Figure 6, drops by a factor of three and the direction switches nearly 180° to mainly a northward electric field. The 180° transition in electric field direction takes about half an hour

(14:30 to 15:00 UT) to complete. Accompanying this transition period, the estimate of Q_j^E drops significantly in accord with the reduced electric field magnitude, while the Q_j estimate is enhanced. The Q_j estimate returns quickly to the reduced Q_j^E estimate after 15:00 UT—that is, once the electric field has completed its transition from southward to northward. This period is studied in more detail in the discussion section. Near 16:00 UT another moderate enhancement in the northward-directed electric field is found resulting in an enhancement in the Joule heating rate with the Q_j^E estimate exceeding the Q_j estimate.

Height-Resolved Data

The period between 7:00 and 9:00 UT was indicated in Figure 7a as a region of moderately enhanced height-integrated Joule heating. The middle panel in Figure 7b illustrates that for this period the neutral wind contribution occurs in the upper E region above about 124 km. The Joule heating rate profile of q_j is, as a result, broader than the q_j^E estimate in the upper E region and, thus, the wind impact is to distribute more heat over a larger altitude range.

The period from 11:00 to 16:00 UT in the middle panel of Figure 7b shows a combination of positive and negative difference values throughout the E region. The positive values (yellow-red regions) depicting neutral wind enhancements in the local Joule heating rate occur largely in the upper E region while the negative values (green-dark blue regions) depicting neutral wind reductions in the local Joule heating rate occur mostly in the lower to middle E region. Over the period from 11:00 to 14:30 UT, the electric field remains consistently southward (see Figure 6), resulting in an eastward E×B drift in the F region. Near 12:30 and 14:00 UT in Figure 7b, a significant reduction in the local Joule heating rate is found. This is similar to the event observed near 18:00 UT on August 5, 1993. The only way a reduction in the local Joule heating rate can occur is if there is a significant component of the neutral wind in the E×B direction—that is, for this case an eastward wind. This supports the general idea that a directionally steady electric field results in a neutral wind contribution that acts to reduce the height-integrated Joule heating rate and makes for more localized Joule heating in the E region.

In the period following 14:30 UT to about 15:00 UT, Figure 7b indicates a significant enhancement in the estimate for q_j occurring in the upper E region with a weak reduction in q_j at lower altitudes. As discussed previously, the electric field was significantly weaker in magnitude and its direction was changing from southward to northward over this time. This increase appears to be due to the neutral wind's residual response to the prior period of active conditions and large electric fields. The changing electric field direction with respect to the neutral wind during this time might be responsible for some of the enhancement but, because of the relatively weak electric field magnitude, the neutral wind magnitude must be the significant factor. This is analyzed further in the discussion section.

Following this event the neutral wind contribution drops dramatically and later acts to reduce the Joule heating rate in the upper E region during the electric field enhancement near

16:00 UT. Again, the neutral wind is acting to reduce the Joule heating on the topside of the E region making a more localized Joule heating with a peak near 117 km.

4. DISCUSSION

The electromagnetic properties of the E region are often characterized individually by estimating the current density, electric field, and conductivity, as was done in the previous section and presented in Figures 1, 2, and 3. Also shown in the previous section is that an equally important assessment of E-region electrodynamics is to determine how these combined properties relate to the dissipation of electromagnetic energy within the ionosphere. Moreover, the present analysis provides observational evidence of the electrical coupling with altitude that can be used to test whether models properly address the extent of E-region coupling among the conductivity, electric field, neutral winds, and currents. Analyzed further in this section are the observations presented in the previous section.

For both experiments it was found that the neutral wind contribution to the local Joule heating rate is altitude dependent. This behavior has led to a number of occasions where the winds effectively reduced the Joule heating rate, typically, just above the Pedersen conductivity peak. This resulted in the height-resolved Joule heating rate to be more concentrated over a narrow altitude regime. The impact of a more localized heat source on the ionosphere–thermosphere system is not well established. The radar-derived ion temperatures (not shown) illustrate a localized altitude region of enhanced temperatures during these times, as is expected if the heating is associated with localized ion frictional heating between the ions and neutrals. The transfer of this more localized heat source to the neutrals and the impact on the neutral composition, ion-neutral chemistry, and neutral dynamics is more complex and requires further assessment. It is expected with this type of narrow energy source gravity waves will be generated. A treatment of gravity wave generation, propagation, and dissipation based on a relatively broad vertical distribution of Joule heating was described by Richmond [1978]. The gravity wave spectrum generated depends on the spatial and temporal characteristics of the source with the vertical wavelengths of the waves dependent on the vertical extent of the source. Owing to our observations of a more localized Joule heating rate, one would expect a different spectrum of gravity waves and different propagation characteristics than that caused by a broader heat source. Further analysis of gravity wave processes associated with localized regions of enhanced Joule heating is required.

As is apparent from the data presented, the neutral wind behavior is critical in determining the altitude distribution of the Joule heating rate and how it may influence the ionosphere–thermosphere system. Figure 5 showed for the August 5, 1993 data near 18:00 UT that the wind rotates in a counterclockwise direction as the altitude decreases, producing a reduction in the Joule heating rate in the upper E region and an enhancement in the Joule heating rate in the lower E region. Counterclockwise rotation of the neutral wind has been commonly observed in numerous TMA trail rocket experiments that measure the neutral wind [e.g., Mikkelsen et al., 1981a; Mikkelsen et al., 1987; Larsen et al., 1995]. This altitude behavior has been attributed to vertically propagating semidiurnal tides that are dominant in the high-latitude, lower E region.

However, the observed enhancement in the lower and upper E-region wind field cannot be explained solely by tidal behavior and seems to be associated with the increase in the magnitude of the northeastward electric field.

In describing the general behavior of the E and F region dynamics, Mikkelsen et al. [1981a,b] and Mikkelsen and Larsen [1983] showed through observations and theoretical arguments that the wind system was in approximate geostrophic/gradient wind balance resulting from Coriolis, pressure gradient, and Lorentz forces. Further analysis of this behavior has been discussed most recently by Larsen and Walterscheid [1995] with emphasis on the effects of the Hall conductivity in modifying the Coriolis parameter and, thus, producing a modified geostrophic balance in the lower E region. This provided a possible theoretical explanation for enhanced neutral wind velocities observed in the lower E region TMA trails during the ARIA rocket experiment [Larsen et al., 1995] and other rocket experiments [Larsen et al., 1989; Mikkelsen et al., 1981a, 1987]. In describing the momentum balance the Lorentz forcing term was expressed in the form of Hall and Pedersen drag coefficients, so named because of their direct dependence on the Hall and Pedersen conductivity, respectively. In the F region and upper E region the Pedersen drag coefficient would be the dominant term for Lorentz forcing while in the lower E region both the Pedersen and Hall drag coefficients must be considered. Larsen and Walterscheid [1995] present a number of simplified solutions that describe the steady-state neutral wind response in the E and F region resulting from the modified geostrophic balance between the Coriolis and Lorentz forces. These simplified solutions will be related to the neutral wind observations for the August 5, 1993 data set.

Case I – Neutral Wind Behavior for August 5, 1993

The neutral wind behavior during the enhanced Joule heating rate period near 18:00 UT on August 5, 1993, has been shown in Figure 5. Figure 8 displays altitude profiles of the zonal and meridional neutral wind components derived from the radar measurements covering the time period from 16:57 to 18:28 UT. The profiles have been color-coded into three specific periods with the blue profiles representing the winds associated with the beginning of the event (16:57 to 17:32 UT), the green profiles representing the winds associated with the main event (17:37 to 17:53 UT), and the red profiles representing the winds associated with the end of the event (17:58 to 18:28 UT). Recall that throughout this period the electric field is intensifying but remains in the northeastward direction.

For the zonal wind, little change was found at and below 117 km throughout the entire event. Above this altitude, the zonal component was found to gradually transition from weakly eastward at the beginning of the event to strongly westward at the peak of the event with the magnitude of this component increasing significantly from 117 km to 140 km. After the peak, the eastward component gradually reduces to weakly westward values (indicated by the red profiles) in the upper E region. This behavior in the eastward component is indicative of enhanced Pedersen drag, directed toward the northwest due to the E×B plasma drift, forcing the

upper E region zonal winds in a westward direction as the electric field intensifies. This behavior is in agreement with the results of Larsen and Walterscheid [1995].

The meridional component of the neutral wind covering the period from 16:57 to 18:28 UT shows more variability in the lower E region; transitioning from weakly northward at the beginning of the event to strongly southward at the peak of the event, maximizing at 117 km. Following the peak, the lower E-region meridional winds gradually reduce to weakly southward winds. In the upper E region the meridional wind shifts in opposite accord to the lower E-region winds with this component becoming strongly northward at the peak of the event and returning to a weakly northward component at the end of the event. The upper E region winds are again consistent with forcing by the northwest Pedersen drag term. The lower E region forcing is more complex with the transitioning between the Pedersen drag force and the Hall drag force as the Hall conductivity begins to dominate over the Pedersen conductivity at and below about 117 km. From the Larsen and Walterscheid [1995] study, a dominant Hall drag under westward plasma drift would produce a northward neutral wind in the lower E region. One can observe the opposite effect in the lower E-region winds with a southward enhancement in the meridional winds during an enhanced northwestward plasma drift. The assumption of steady state by Larsen and Walterscheid, the exclusion of upward propagating tides that become important in this part of the E region, and the effects of the local Joule heating rate on the neutral dynamics may be responsible for the deviation between the theory and our lower E-region observations.

Overall, the neutral wind behavior presented in Figure 8 explains the differences between the q_j and q_j^E estimates with each of these profiles throughout the experiment matching the specific roots needed to satisfy (8) in the same manner as was performed for the single profile shown in Figure 5. Figure 9 shows the neutral wind vectors from 17:00 to 19:00 UT that result from combining the components shown in Figure 8. The combined vectors show that as the electric field increased at the beginning of the event the upper E region neutral winds began to increase in magnitude and rotate counterclockwise into the E×B direction, effectively reducing the Joule heating rate in the upper E region at the peak of the event. After the peak, the upper E region winds reduced in magnitude but remained in the E×B direction. In the lower E region below 120 km, a rotation in time from eastward was found at the beginning of the event to southward-directed neutral winds maximizing at the peak of the event. The southward wind effectively enhances the local Joule heating rate in the lower E region. Thus, one finds from this event, and the other data set, that the counterclockwise rotation in the neutral wind with decreasing height impacts the Joule heating rate in an altitude-dependent manner. This event also illustrates that the electric field, with a peak magnitude of 60 mV/m, significantly influences the response of the neutral wind well into the lower E region.

Case II – Neutral Wind Behavior for May 2, 1995

The electric field and Joule heating rates for the May 2, 1995 experiment have been shown in Figures 6 and 7. The difference plot in Figure 7b revealed a number of regions of significant

and complex differences, which reflect the variable conditions for this day. This complex behavior in the local and height-integrated Joule heating rates implies a complex behavior in the neutral wind field. As the differences between q_j and q_j^E have been attributed to neutral wind effects, it is important to recognize that the neutral winds have a much better memory of past forcing and a poor response to current events than the electric field and the resultant ion drift. The spatial scale of the forcing also impacts the ion drift and neutral wind response differently. This is particularly important in this present study as measurements made nearly overhead by the radar may reflect quite well the local changes in the electric field, ion drift, and neutral wind but interpretation of the neutral wind behavior would require better spatial and temporal coverage to trace its forcing history. For the August 5, 1993 data set it was implicitly assumed that the observed local behavior in the measured electric field and neutral wind represented a large-scale feature that could explain the observed local behavior in the wind. This appeared to be appropriate for the relatively quiet conditions associated with that day. For the May 2, 1995 data set, the complex conditions make it difficult to make such an assumption. Therefore, the behavior of the neutral wind, like in case I, has not been interpreted, but the impact of the neutral wind in describing the differences between q_j and q_j^E observed on this day has simply been indicated.

It has been shown in case I that the neutral winds derived from the ion momentum equation using (15) are equal to the specific roots needed to describe the differences between q_j and q_j^E. The roots for May 2, 1995 data have been evaluated and it was found that the neutral wind estimate using the ion momentum equation also is representative of the specific roots needed to describe the differences between the q_j and q_j^E for this day. Using these wind estimates and applying them to (7), the two terms that determine the sign of $\Delta q(z)$ can be evaluated. The first term, $|u_n(z)|^2|B|$, represents the contribution of the neutral wind magnitude to the Joule heating rate. The second term, $-2|E||u_n(z)|\cos(\theta)$, represents the contribution of the neutral wind component in the E×B direction to the local Joule heating rate. The interplay between these two terms determines the manner by which the neutral wind is enhancing or reducing the local Joule heating rate. Figure 10 is a plot of these two terms covering the time period between 06:58 and 16:27 UT. As most of the differences in Figure 7b are from the upper E region, both terms in Figure 10 have been plotted for the altitudes of 117.3 km, 123.0 km, 128.6 km, 134.3 km, and 139.9 km. The color code identifies these altitudes with the appropriate line. Term 1 will always serve to enhance the Joule heating rate and, therefore, will be a positive term contributing to $\Delta q(z)$. A negative term 2 is an indication that a component of the neutral wind is in the E×B direction while a positive value indicates the neutral wind component is opposite to the E×B direction. Therefore, in order to have a negative $\Delta q(z)$, there must be a component of the neutral wind in the E×B direction and of sufficient magnitude to make term 2 negative and greater than term 1. It should be noted, and is shown in (6), that the neutral wind contribution to the Joule heating rate is weighted by the local Pedersen conductivity. Thus, strong neutral winds can be present throughout the E region but its contribution to the Joule heating rate will also be dependent on the altitude distribution of the Pedersen conductivity. In combination with Figure

7b, the evaluated terms presented in Figure 10 will be used to help interpret and evaluate the differences between the q_j and q_j^E estimates for this day.

It is clear from Figure 10 that the Joule heating rate for the period between 7:00 and 10:00 UT is dominated by term 1 in the upper E region resulting in an overall enhancement of the Joule heating rate (see Figure 7). Term 2 in Figure 10 transitions from positive to negative values over this time period indicating a neutral wind rotation with time that is, at first, opposite to the E×B direction (enhancing Joule heating) and then rotates into the E×B direction (reducing Joule heating). A half-hour prior to this period the electric field direction rotated briefly from southward to eastward and the electric field magnitude increased by over a factor of 3.

After about 10:00 UT, the neutral wind behavior is quite variable with the magnitude of the neutral wind vacillating in accordance with vacillations in the neutral wind direction, as shown by both terms in Figure 10a,b. At times, term 2 becomes positive indicating a neutral wind direction opposite to the E×B drift and, thus, contributing to the enhancement of the Joule heating rate. However, for the most part term 2 was significantly negative and often exceeded the positive contribution from term 1, particularly at times near 12:30, 13:15, 14:00, and 16:00 UT. The period between 12:30 and 14:00 UT is similar to the event observed near 18:00 UT on August 5, 1993 with an extended period of a directionally steady electric field, which in this case was southward. The only way a reduction in the local Joule heating rate can occur is if there is a significant component of the neutral wind in the E×B direction—that is, for this case an eastward wind. The 16:00 UT period is a bit different as the reduction in the Joule heating rate came after the electric field became northeastward, thus, requiring a northwestward neutral wind.

In the period following 14:30 UT to about 15:00 UT, Figure 7 showed a significant enhancement in the estimate for q_j occurring in the upper E region with a weak reduction in q_j at lower altitudes. As discussed previously, the electric field was significantly weaker in magnitude and its direction was changing from southward to northward over this time. The electric field rotation is apparent in term 2 of Figure 10b as the values change from positive to strongly negative. The wind magnitude, indicated by term 1 in Figure 10a, increases significantly at this time and becomes the dominant term producing an overall enhancement in the Joule heating rate. The increase in the wind magnitude is not clear, however, this may be a good indication that the collision frequency model used is not appropriate under these active conditions. However, even after reducing the collision frequency profile by a factor of 2, the neutral wind was still a dominant factor and the feature, although reduced, still remained. The following subsection discusses further the impact of the collision frequency model on the Joule heating rates and neutral wind estimates.

Collision Frequency Sensitivity

In describing the height-resolved and height-integrated Joule heating rates and the associated neutral wind behavior a semi-empirical model was used to provide the ion-neutral collision frequency values that are needed in all of these calculations. The model was described

previously in section 2 and is uniquely specified for each experiment by using the appropriate A_p and $F_{10.7}$ indices as input into the MSIS-90 model for the particular day. The estimate of the Joule heating rate, q_j, using (13) is directly proportional to the inverse of the collision frequency. The approximated estimate of the Joule heating rate, q_j^E, using (2) is dependent on the collision frequency through the estimate of the Pedersen conductivity. As discussed by Brekke and Rino [1978], the height of maximum Joule heating rate, q_j^E, estimated by (2) is much more sensitive to the model collision frequency (and, therefore, the model neutral atmosphere) than that estimated by (13). The neutral wind estimate using (15) is also dependent on the inverse of the collision frequency but its impact is scaled by the relationship between the electric field and local ion drift given by the bracketed term in (15), as discussed by Rino et al. [1977] and Johnson [1990]. As each of the estimates are influenced in a different way by the collision frequency, it is important to recognize the sensitivity of these estimates for different collision frequency values. To perform this sensitivity test the collision frequency was modified by multiplying the neutral density provided by MSIS-90 by factors of 75% and 125%. The Joule heating event on August 5, 1993 near 18:00 UT presented in Figure 4 is used to illustrate the impact of the collision frequency on the actual data.

The collision frequency model used for this day is presented in Figure 11a along with collision frequency profiles scaled by 75% and 125% of the MSIS-90 density. Also plotted in Figure 11 are the q_j profiles (11b), the q_j^E profiles (11c), profiles of the collision frequency-dependent component of the Pedersen conductivity (11d), and profiles of the neutral wind components (11e) from the August 5, 1993 data set at 17:43 UT based on the different values of collision frequency given in Figure 11a. The sensitivity of the height-resolved Joule heating rate, q_j, shown in Figure 11b illustrates the inverse dependence of this estimate on the collision frequency. The collision frequency does not impact the peak height of the estimate nor the overall shape of the Joule heating profile but simply modifies the area under the curve. The change in area under the curve by the collision frequency will have an impact when this local estimate is height-integrated over E-region altitudes.

Figure 11c is a plot of the height-resolved Joule heating rate (q_j^E) and shows little change in the peak value but an overall shift of the entire profile to higher and lower altitudes. The lack of change in the area under the curve indicates that the collision frequency has little impact on the height-integrated estimate using (2). The Pedersen conductivity is the parameter in (2) that is dependent on the collision frequency and can be written as

$$\sigma_p(z) = \frac{en_e(z)}{B} \frac{\Omega_i(z)\nu_{in}(z)}{\Omega_i^2(z) + \nu_{in}^2(z)} \quad . \tag{16}$$

The second term determines the behavior of the Pedersen conductivity with collision frequency. This term is plotted in Figure 11d and shows clearly that a value of 125% of the collision frequency raises the entire layer up in altitude by about 3 km, while 75% of the value lowers the

layer by an equivalent distance. This is not as clearly seen in the q_j^E profiles in Figure 11c because of the changing electron density with height.

Figure 11e shows the sensitivity of the neutral wind zonal and meridional components to changes in the collision frequency. The unaltered behavior of the zonal component suggests an insensitivity to changes in collision frequency and reflects a small contribution from the bracketed term given in (15) for this time period. The meridional component is sensitive to collision frequency and responds most significantly in the lower E region. Here, the meridional wind increases when the collision frequency value is multiplied by 75%. This would create an unreasonable wind speed in the lower E region that is not easily justified physically. Multiplying the collision frequency by 125% reduces the meridional wind in the lower E region and increases the upper E region meridional winds. Irrespective of the changes in collision frequency (assuming the collision frequency shape does not change significantly), the neutral wind profile with altitude is not changed dramatically. This would indicate that, although some uncertainty exists, the neutral wind profile derived from the radar measurements is representative throughout the E region for this period. This behavior can also be seen in the difference plots between q_j and q_j^E presented in Figure 4b and 7b. Referring to Figure 4b, the multiplying factor of 125% intensifies the negative differences (blue) and reduces the positive differences (red), and vice versa for the factor of 75%. As these differences reflect the neutral wind behavior, the uncertainty in the collision frequency in determining the Joule heating rate may be bounded by placing physical constraints on the neutral wind.

The height-integrated quantities are obviously also affected by the collision frequency. When multiplying the collision frequency profile by 75% and 125%, little change is found in the height-integrated quantity, Q_j^E, as was indicated by the local estimates presented in Figure 11c. The height-integrated quantity Q_j, however, is sensitive to the collision frequency value as the area under the curve in Figure 11b changes with collision frequency. It is apparent that by changing the collision frequency the two height-integrated quantities could be forced to be equal. However, unless the two quantities have equal shapes throughout the E region, the neutral winds must be modified accordingly to compensate for the local differences and to make the height-integrated quantities the same. This results in nonphysical wind fields, thus, again limiting the range of possible collision frequency profiles.

Therefore, a tradeoff exists concerning the two approaches when considering the impact of collision frequency. The estimates of q_j provide profiles of the Joule heating rate with accurate estimates of the peak height and profile shape with the entire profile scaled by the uncertainty in the collision frequency. The profile estimates of q_j^E are dependent on the collision frequency in terms of its ability to determine the peak height of maximum Joule heating. The height-integrated quantity of Q_j^E shows an indifference to the collision frequency while the Q_j scales inversely by the collision frequency. Because the change in collision frequency impacts the two Joule heating rate estimates differently, the neutral wind profile must also be modified by changes in collision frequency. Assuming the shape of the collision frequency does not change

significantly, the collision frequency modifies the level of influence the E-region neutral winds have on the height-resolved and height-integrated Joule heating rates but does not eliminate their importance. The same results apply to the May 2, 1995 data set but due to the complexity in the conditions for that day, the collision frequency behavior is difficult to assess.

5. CONCLUSION

The improved capability of the Sondrestrom incoherent-scatter radar to sample the E region at high resolution provides new insight into high-latitude E-region electrodynamic behavior in terms of currents, conductivities, electric fields, and neutral winds. These electrodynamic parameters have been presented and used to evaluate the radar estimation of the height-resolved and height-integrated E-region Joule heating rates and the influence of the neutral wind on these estimates. Two separate approaches to estimating the Joule heating rate have been presented. The first, and more typical approach, has been to determine the Pedersen conductivity and electric field from the radar measurements and estimate the Joule heating rate, q_j^E, neglecting the neutral wind. The second, and less frequently used approach, has been to determine the local current density (which includes the neutral winds implicitly) and Cowling conductivity from the radar measurements and estimate the Joule heating rate, q_j, accounting for the neutral wind. Two 24-hour MLTCS World Day radar experiments (August 5, 1993 and May 2, 1995) that correspond to solar minimum, daytime periods of moderate geomagnetic activity were used to evaluate the Joule heating rates. The following describes the conclusions obtained from this study.

1. The ability to measure the height-resolved Joule heating rate, q_j, that includes the neutral wind revealed significantly more structure in both experiments than observed in the q_j^E profiles (whose altitude dependence is described by the Pedersen conductivity). This structure is attributed to the E-region neutral wind and its altitude-dependent influence on the Joule heating rate; often, enhancing the local Joule heating rate at one altitude while reducing the Joule heating rate at another. This led to a number of occasions where a much narrower and more localized enhancement occurred in the height-resolved Joule heating rate. Radar data from the August 5, 1993 experiment near 18:00 UT provided a good illustration of this effect with neutral winds reducing the local Joule heating rate by over 75% in the upper E region while neutral winds enhanced the local Joule heating rate by nearly 50% in the lower E region. The E-region height-integrated Joule heating rate for this particular time period experienced an overall decrease of 40% due to the neutral wind. Thus, the cancellation of opposing contributions to the Joule heating rate by the wind with height results in a lesser overall neutral wind contribution to the height-integrated quantity. In addition, the localization of the E-region Joule heating rate (about 12 km for the case discussed above) caused by the presence of the neutral wind is a new observation whose impact on the ionosphere–thermosphere system requires further investigation.

2. From the two radar experiments, one finds that the upper E-region neutral winds modify the Joule heating rate in a manner that is associated with the behavior of the electric field. Typically, it was found that when the electric field direction remained steady and only the magnitude of the electric field was enhanced the neutral winds acted to reduce the upper E-region Joule heating rate. During times when the electric field direction changed significantly, it was found that the neutral winds acted to enhance the upper E-region Joule heating rate.

Subsequent counterclockwise rotation of the neutral wind with decreasing altitude typically led to enhancements in the Joule heating rate in the lower E-region.

3. The most significant neutral wind contribution to the Joule heating rate came after a substorm period on May 2, 1995 where an enhancement in the height-integrated Joule heating rate by over 400% occurred. Here the majority of the neutral wind contribution came from the upper E region. This enhancement occurred during a 180° change in electric field direction and an overall reduction in electric field magnitude. Other enhancements of the height-integrated Joule heating rate by 200% were observed to occur during periods of significant changes in the electric field direction. Reduction of the height-integrated Joule heating rate by the neutral winds by as much as 40% were observed during periods of elevated magnitude in the electric field but with the direction of the electric field steady for extended periods.

4. Overall, the estimate of the height-integrated Joule heating rate, Q_j^E, assuming the neutral wind is zero served as a limited proxy for the two data sets presented and showed an invariance to moderate changes in the ion-neutral collision frequency model. The height-integrated Joule heating rate, Q_j, is more susceptible to changes in the ion-neutral collision frequency model, as the height-resolved profile is inversely proportional to the collision frequency. Yet, the height of maximum Joule heating is best estimated by the q_j profile, which is not influenced by the change in collision frequency. Finally, reasonable changes to the ion-neutral collision frequency model can modify the absolute values presented in this work, but cannot eliminate the neutral wind effects presented nor the trends observed.

Acknowledgments. This work was supported by the NSF Cooperative Agreement ATM-9317167, NASA contract NAGW-3508, and Air Force contract F19628-94-C-0100. Helpful discussions were provided by John Kelly, Roland Tsunoda, and Rick Doe at SRI. Thanks also to Carol Leger and Mary McCready for thir efforts in processing the Sondrestrom radar data.

6. REFERENCES

Banks, P.M., "Observations of Joule and Particle Heating in the Auroral Zone," *J. Atmos. and Terr. Phys.*, Vol. 39, p. 179, 1977.

Brekke, A.C., and C.L. Rino, "High-resolution altitude profiles of the auroral zone energy dissipation due to ionospheric currents," *J. Geophys. Res.*, Vol. 83, A6, 2517-2524, 1978.

Brekke, A., C. Hall, and O. Pettersen, "EISCAT UHF Studies of Ionospheric Currents on June 16-17, 1987," *Ann. Geophys.*, Vol. 8, p. 213, 1990.

Baumjohann, W., and Y. Kamide, "Hemispherical Joule heating and the AE indices," *J. Geophys. Res.*, Vol. 89, No. A1, p. 383-388, 1984.

Cole, K.D., "Joule heating of the upper atmosphere," *Aust. J. Phys.*, Vol. 15, p. 223, 1962.

Cole, K.D., "Energy deposition in the thermosphere caused by the solar wind," *J. of Atmos. and Terr. Phys.*, Vol. 37, pp. 939-949, 1975.

de la Beaujardiére, O., R. Johnson, and V.B. Wickwar, "Ground-based measurements of Joule heating rates," *Auroral Physics*, pp. 439-448, 1991.

Foster, J.C., J.-P. St.-Maurice, and V.J. Abreu, "Joule heating at high latitudes," *J. Geophys. Res.*, Vol. 88, No. A6, p. 4885, 1983.

Heelis, R.A., and W.R. Coley, "Global and local Joule heating effects seen by DE 2," *J. Geophys. Res.*, Vol. 93, No. A7, p. 7551, 1988.

Johnson, R.M., "Lower-thermospheric neutral winds at high latitude determined from incoherent scatter measurements: A review of techniques and observations," *Adv. Space Res.*, Vol. 10, No. 6, p. 261, 1990.

Kamide, Y., and A. Brekke, "Altitude variations of ionospheric currents at auroral latitudes," *Geophys. Res. Lett.*, Vol. 20, No. 4, p. 309, 1993.

Kelly, J.D. and V.B. Wickwar, Radar measurements of high-latitude ion composition between 140 and 300 km altitude, *J. Geophys. Res.*, *86*, A9, 7617–7626, 1981.

Lehtinen, M. S., Statistical Theory of Incoherent Scatter Measurements, Ph.D. thesis, Univ. of Helsinki, Helsinki, EISCAT Technical Note 86/45, 1986.

Lehtinen, M.S., and I. Haggstrom, "A new modulation principle for incoherent scatter measurements," *Radio Sci.*, Vol. 22, No. 4, p. 625, 1987.

Lu, G., A. D. Richmond, B. A. Emery, and R. G. Roble, "Magnetosphere–ionosphere–thermosphere coupling: Effect of neutral winds on energy transfer and field-aligned current,"*J. Geophys. Res.*, Vol. 100, No. A10, pp. 19,643-19,659, 1995.

Larsen, M.F., and R.L. Walterscheid, "Modified geostrophy in the thermosphere," *J. Geophys. Res.,* Vol. 100, No. A9, p. 17,321, 1995.

Larsen, M.F., I.S. Mikkelsen, J.W. Meriwether, R. Niciejewski, and J. Vickrey, "Simultaneous observations of neutral winds and electric fields at spaced locations in the dawn auroral oval," *J. Geophys. Res ,* Vol. 94, 17235–17243, 1989.

Larsen, M.F., T.R. Marshall, I.S. Mikkelsen, B.A. Emery, A. Christensen, D. Kayser, J. Hecht, L. Lyons, and R. Walterscheid, "Atmospheric Response in Aurora Experiment: Observations of E and F region neutral winds in a region of postmidnight diffuse aurora," *J. Geophys. Res.*, Vol. 100, 17299–17308, 1995.

Mikkelsen, I.S., T.S. Jorgensen, M.C. Kelley, M.F. Larsen, E. Pereira, and J. Vickrey, "Neutral winds and electric fields in the dusk auroral oval, 1, Measurements, "*J. Geophys. Res.*, Vol. 86, 1513–1524, 1981a.

Mikkelsen, I.S., T.S. Jorgensen, M.C. Kelley, M.F. Larsen, E. Pereira, and J. Vickrey, "Neutral winds and electric fields in the dusk auroral oval, 2, Theory and model," *J. Geophys. Res.*, Vol. 86, 1525–1536, 1981b.

Mikkelsen, I.S. and M.F. Larsen, "An analytic solution for the response of the neutral atmosphere to the high-latitude convection pattern," *J. Geophys. Res.*, Vol. 88, 8073–8080, 1983.

Mikkelsen, I.S., M.F. Larsen, M.C. Kelley, J. Vickrey, E. Friis-Christensen, J. Meriwether, and P. Shih, "Simultaneous measurements of the thermospheric wind profile at three separate positions in the dusk auroral oval," *J. Geophys. Res.*, Vol. 92, 4639–4648, 1987.

Rich, F.J., M.S. Gussenhoven, and M.E. Greenspan, "Using simultaneous particle and field observations on a low altitude satellite to estimate Joule heat energy flow into the high latitude ionosphere," *Annales Geophysicae,* pp. 527-534, 1987.

Rich, F.J., M.S. Gussenhoven, D.A. Hardy, and E. Holeman, "Average height-integrated Joule heating rates and magnetic deflection vectors due to field-aligned currents during sunspot minimum," *J. of Atmos. and Terr. Phys.,* Vol. 53, No. 3/4, pp. 293-308, 1991.

Richmond, A.D., "Gravity wave generation, propagation, and dissipation in the thermosphere," *J. Geophys. Res.,* Vol. 83, No. A9, p. 4131, 1978.

Rino, C.L., A. Brekke, and M.J. Baron, "High-resolution auroral zone E region neutral wind and current measurements by incoherent scatter radar," *J. Geophys. Res.,* Vol. 82, No. 16, p. 2295, 1977.

Schunk, R.W., and A.F. Nagy, "Ionospheres of the terrestrial planets," *Rev. Geophys. and Space Phys.,* Vol. 18, No. 4, p. 813, 1980.

Thayer, J.P., J.F. Vickrey, R.A. Heelis, and J.B. Gary, "Interpretation and modeling of the high-latitude electromagnetic energy flux," *J. Geophys. Res.*, Vol. 100, No. A10, pp. 19,715-19,728, 1995.

Vickrey, J.F., R.R. Vondrak, and S.J. Matthews, "Energy deposition by precipitating particles and Joule dissipation in the auroral ionosphere," *J. Geophys. Res.*, Vol. 87, No. A7, pp. 5184-5196, 1982.

FIGURES

Figure 1. Resolved electric field derived from three-position radar measurements for August 5, 1993 presented in the form of direction and magnitude versus Universal Time. Zero degrees represents an eastward electric field and positive angles correspond to a counterclockwise rotation from east. Errors in the electric field never exceed 2 mV/m.

Figure 2. Height-resolved, E-region ion drifts and the $\log_{10}$ electron densities at 6 km vertical resolution from three-position radar measurements for August 5, 1993.

Figure 3. Height-resolved, E-region current density and $\log_{10}$ Pedersen conductivity at 6 km vertical resolution for August 5, 1993 derived from the data presented in Figures 1 and 2.

Figure 4. (a) Compares the height-integrated Joule heating rate (Qj^E) excluding neutral winds, depicted by the solid black line, with the height-integrated Joule heating rate (Qj) including neutral winds, depicted by the solid orange line. The height profiles used to determine the height-integrated Joule heating rates are provided in (b). The height-resolved Joule heating rates (qj^E), using (2), are presented in the bottom panel and the height-resolved Joule heating rates (qj), using (13), are presented in the top panel. The middle panel represents the difference between the top and bottom panels with green-blue colors indicating reductions in the Joule heating rate and yellow-red indicating enhancements in the Joule heating rate. The difference plot relates to (6) given in section 2 and, therefore, provides an indication of the neutral wind influence on the Joule heating rate. Relative errors in Q_j in excess of 50% are excluded.

Figure 5. Height-resolved solutions to the quadratic formula given by (8) representing the possible neutral wind magnitudes and directions that can satisfy the observed differences between the two approaches to estimating the Joule heating rate are presented by the color-coded lines for August 5, 1993 at 17:43 UT. The wind direction is with respect to the E×B drift direction, indicated by zero degrees, with counterclockwise rotation of the wind associated with increasing angle. The altitude of each solution is color coded and the neutral wind values at each altitude derived using (15) are shown by the color-coded stars. Profiles of the zonal and meridional components of the wind are presented in the insert.

Figure 6. Resolved electric field derived from three position radar measurements for May 2, 1995 presented in the same manner as Figure 1. Errors in the electric field never exceed 2 mV/m.

Figure 7. (a) Height-integrated and (b) height-resolved Joule heating rates for May 2, 1995 presented in the same manner as Figure 4. Relative errors in Q_j in excess of 50% are excluded and the profiles are zeroed out.

Figure 8. Derived neutral wind zonal and meridional components covering the time period from 16:57 to 18:28 UT on August 5, 1993. The profiles are color-coded to represent select periods of the Joule heating event near 18:00 UT with blue lines representing prior to the peak, the green lines are during the peak, and the red lines are after the peak. The mean error for the two

components is also presented with variations in the error of ± 50 m/sec above 125 km and ± 20 m/sec below.

Figure 9. Resolved E-region neutral wind vectors for August 5, 1993 covering the same period as Figure 8.

Figure 10. The height-resolved contribution of the neutral wind to the Joule heating rate for May 2, 1995 is presented using the two terms in (7) with (a) term 1 = $|u_n(z)|^2|B|$ and (b) term 2 = $-2|E||u_n(z)|\cos(\theta)$. See section 2 text for details.

Figure 11. (a) Collision frequency model multiplied by constant factors of 75% and 125%. The sensitivity of (b) q_j, (c) q_j^E, (d) Pedersen factor, and (e) neutral wind to the collision frequency model for August 5, 1993 at 17:43 UT.

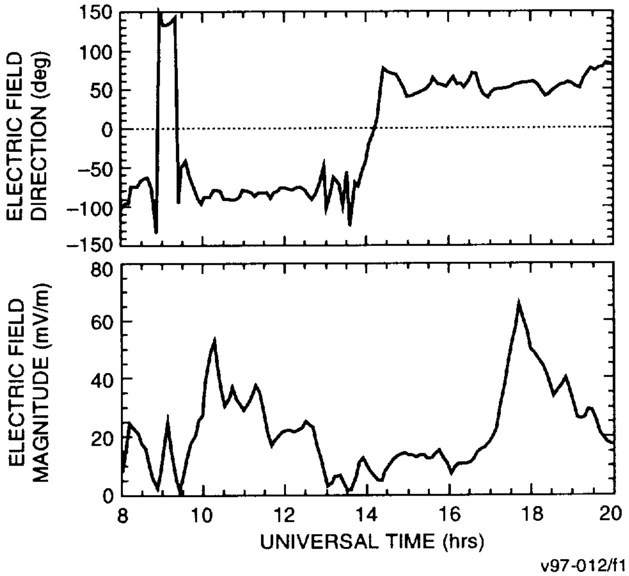
ELECTRIC FIELD DIRECTION (deg)
150
100
50
0
−50
−100
−150
ELECTRIC FIELD MAGNITUDE (mV/m)
80
60
40
20
0
8
10
12
14
16
18
20
UNIVERSAL TIME (hrs)
v97-012/f1

Figure 1

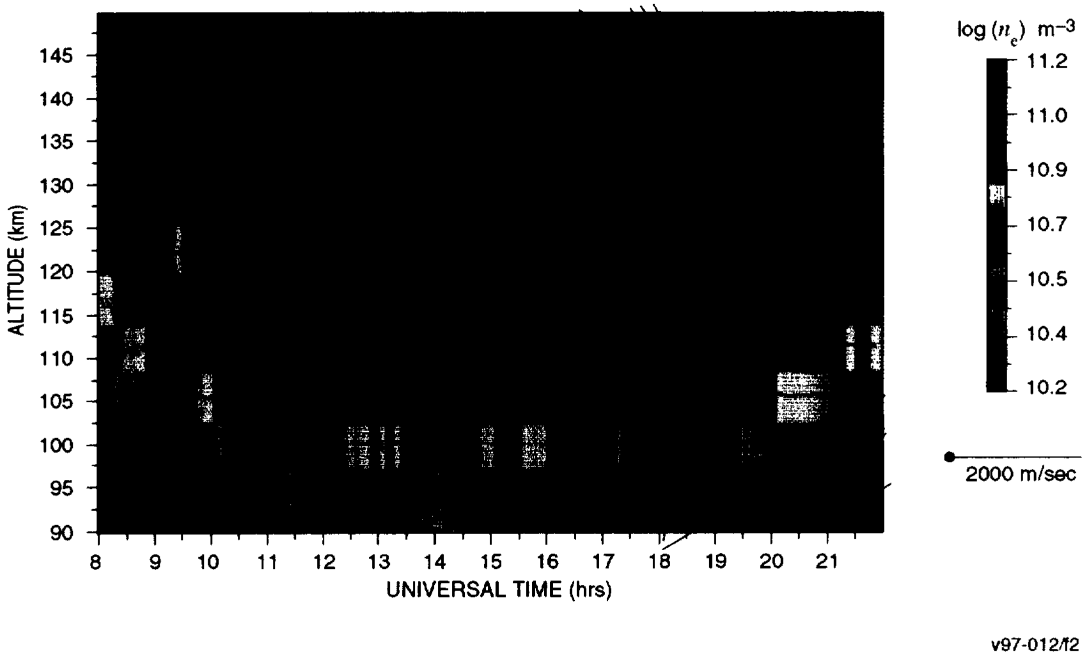

log (n_e) m^{-3}
11.2
11.0
10.9
10.7
10.5
10.4
10.2
2000 m/sec
ALTITUDE (km)
145
140
135
130
125
120
115
110
105
100
95
90
8
9
10
11
12
13
14
15
16
17
18
19
20
21
UNIVERSAL TIME (hrs)
v97-012/f2

Figure 2

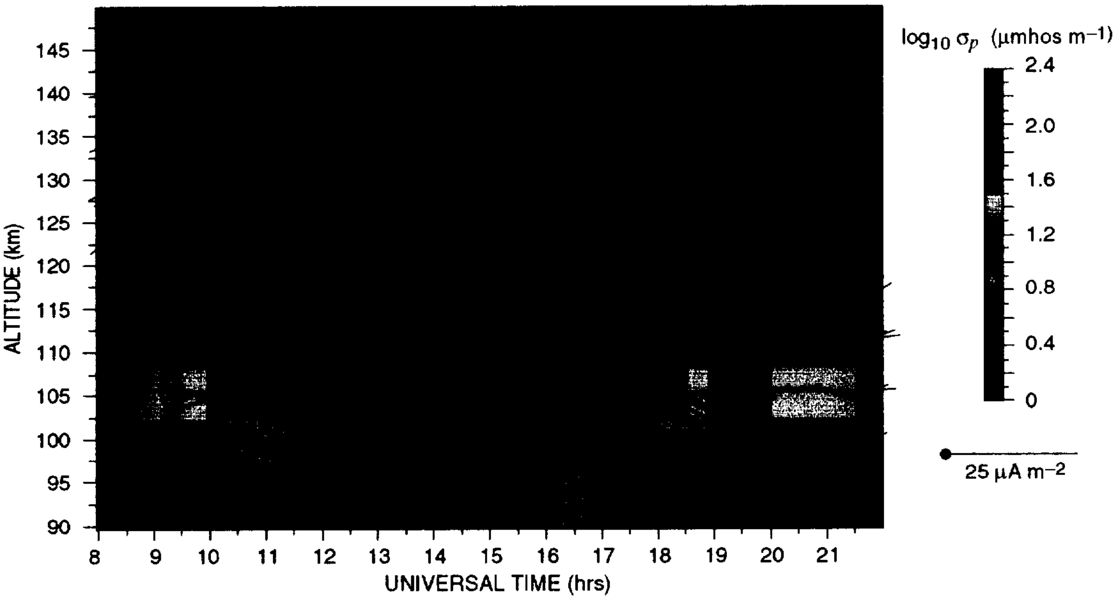

v97-012/13

Figure 3

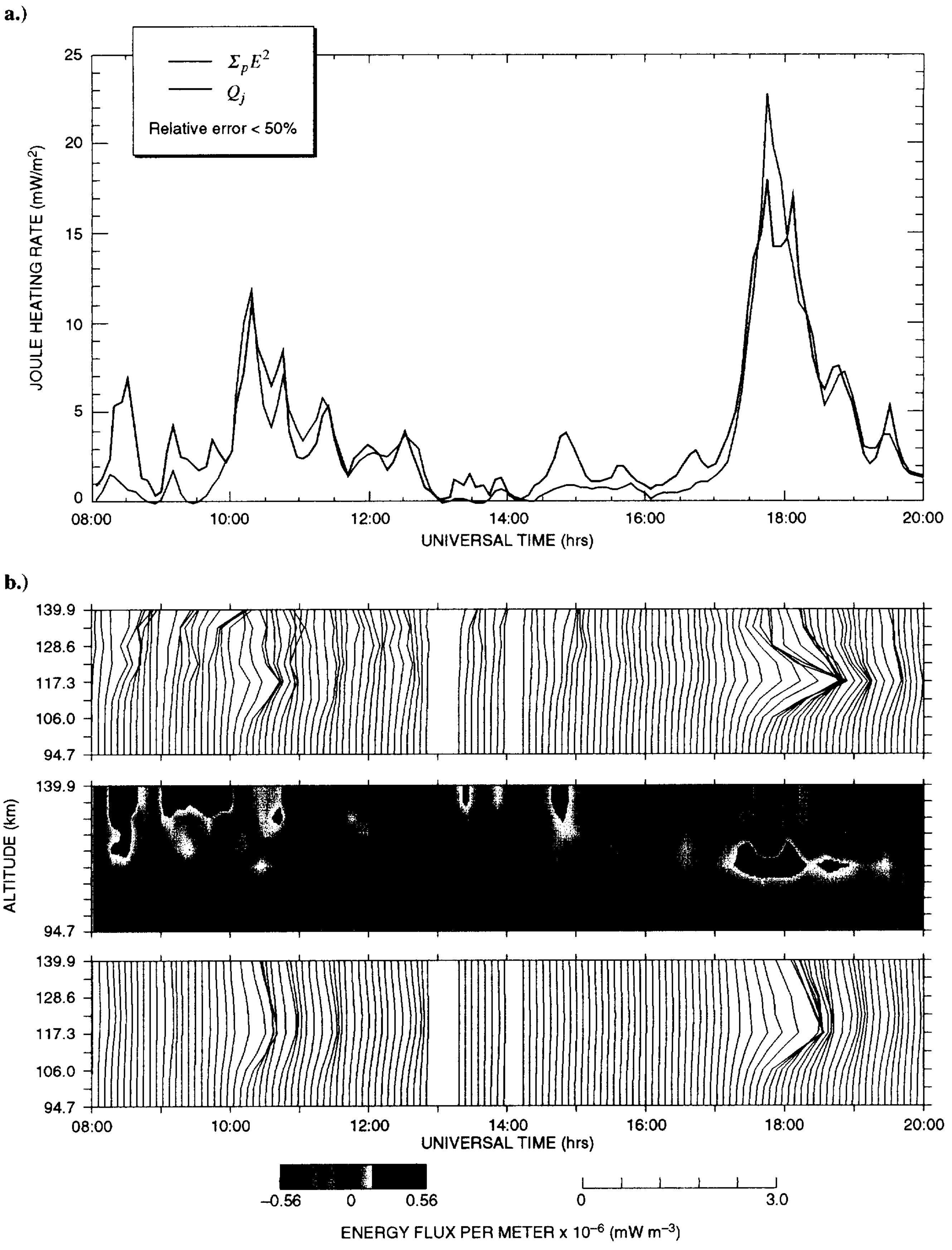

v97-012/14

Figure 4

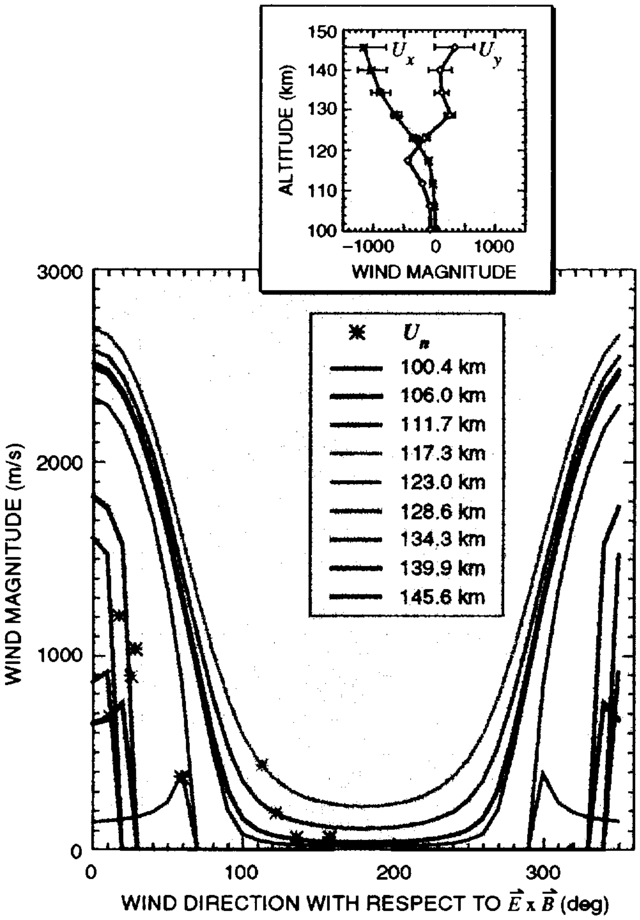

v97-012/15

Figure 5

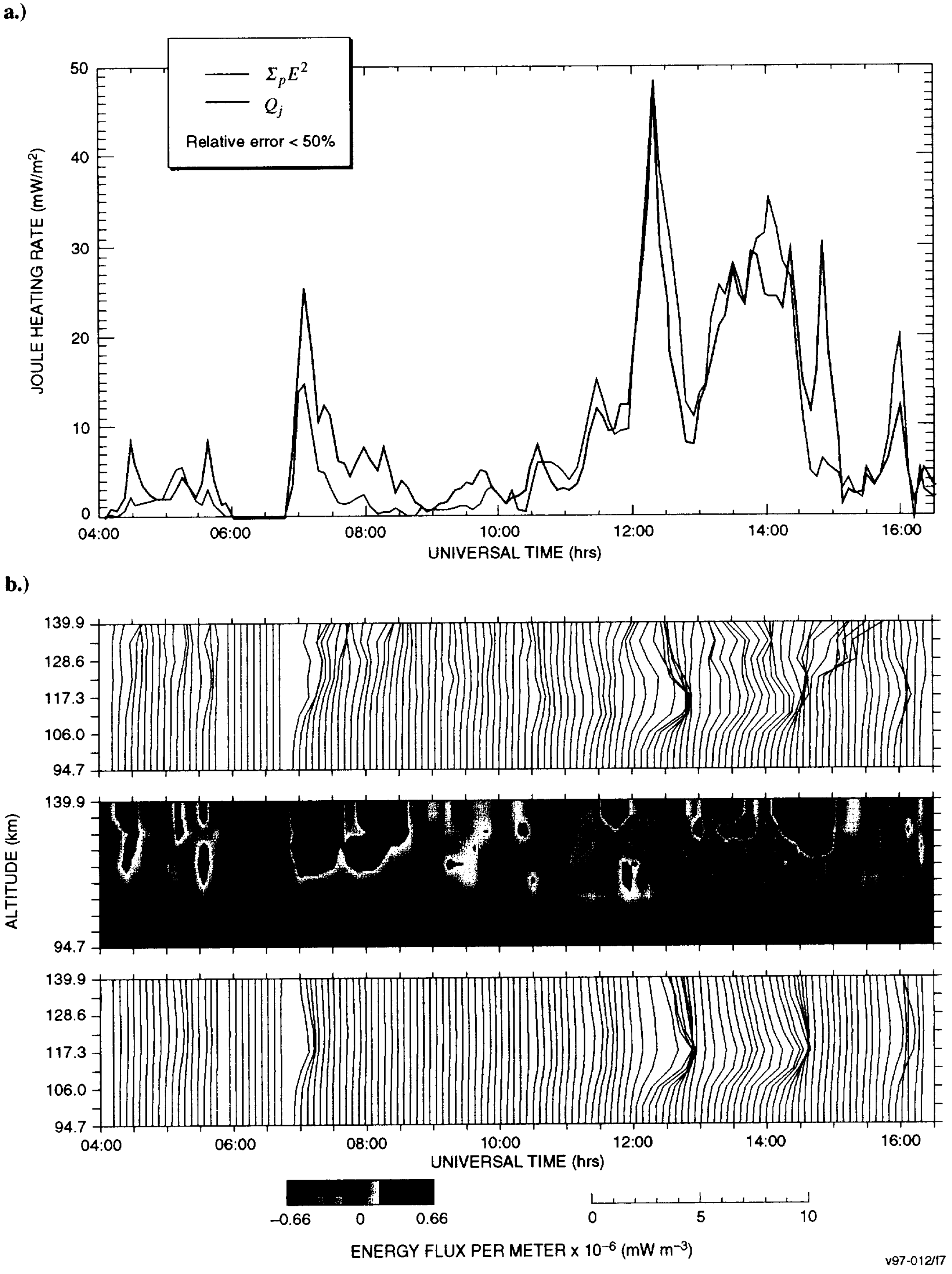
a.)
$\Sigma_p E^2$
Q_j
Relative error < 50%
JOULE HEATING RATE (mW/m^2)
50
40
30
20
10
0
04:00
06:00
08:00
10:00
12:00
14:00
16:00
UNIVERSAL TIME (hrs)
b.)
ALTITUDE (km)
139.9
128.6
117.3
106.0
94.7
04:00
06:00
08:00
10:00
12:00
14:00
16:00
UNIVERSAL TIME (hrs)
–0.66
0
0.66
0
5
10
ENERGY FLUX PER METER x 10^{-6} (mW m^{-3})
v97-012/f7

Figure 7

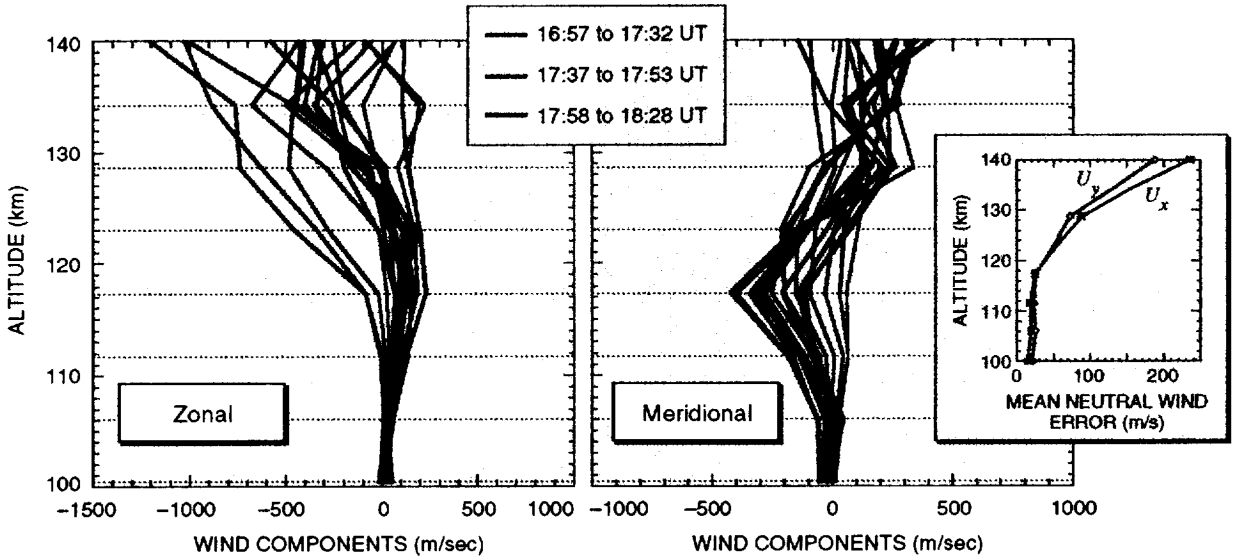

v97-012/18

Figure 8

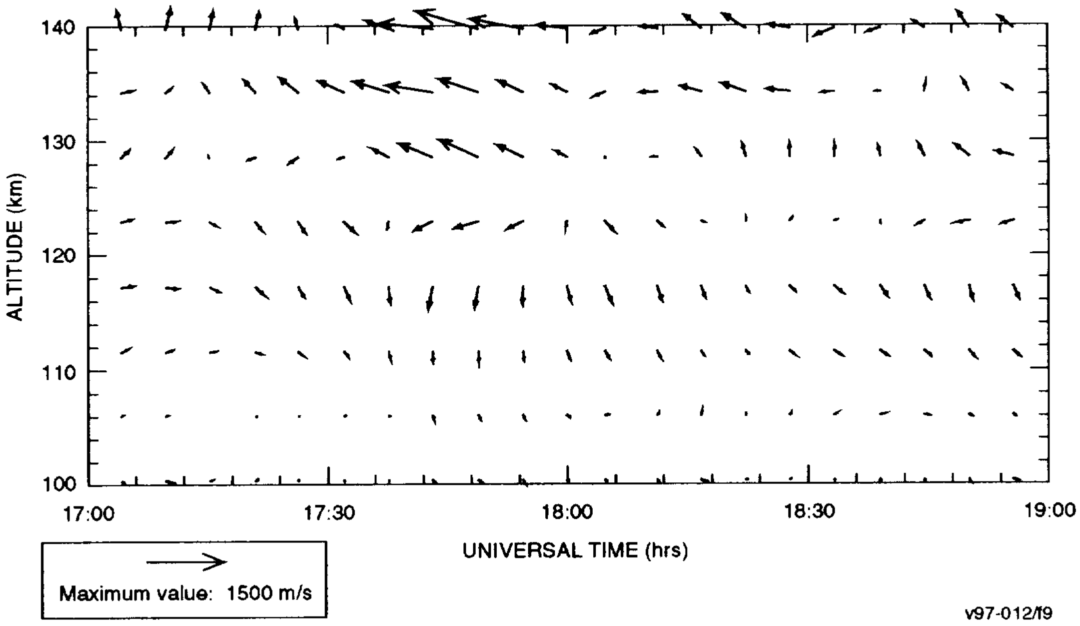
140
130
120
110
100
ALTITUDE (km)
17:00
17:30
18:00
18:30
19:00
UNIVERSAL TIME (hrs)
Maximum value: 1500 m/s
v97-012/f9

Figure 9

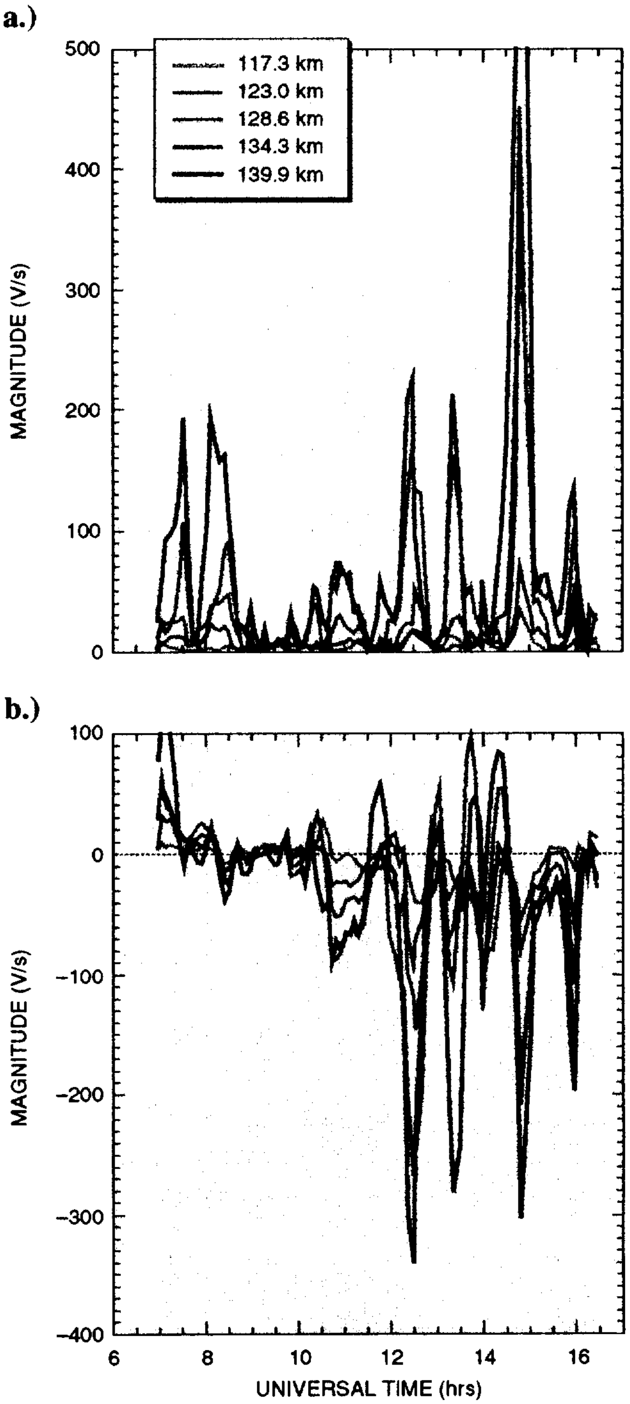

v97-012/f10

Figure 10

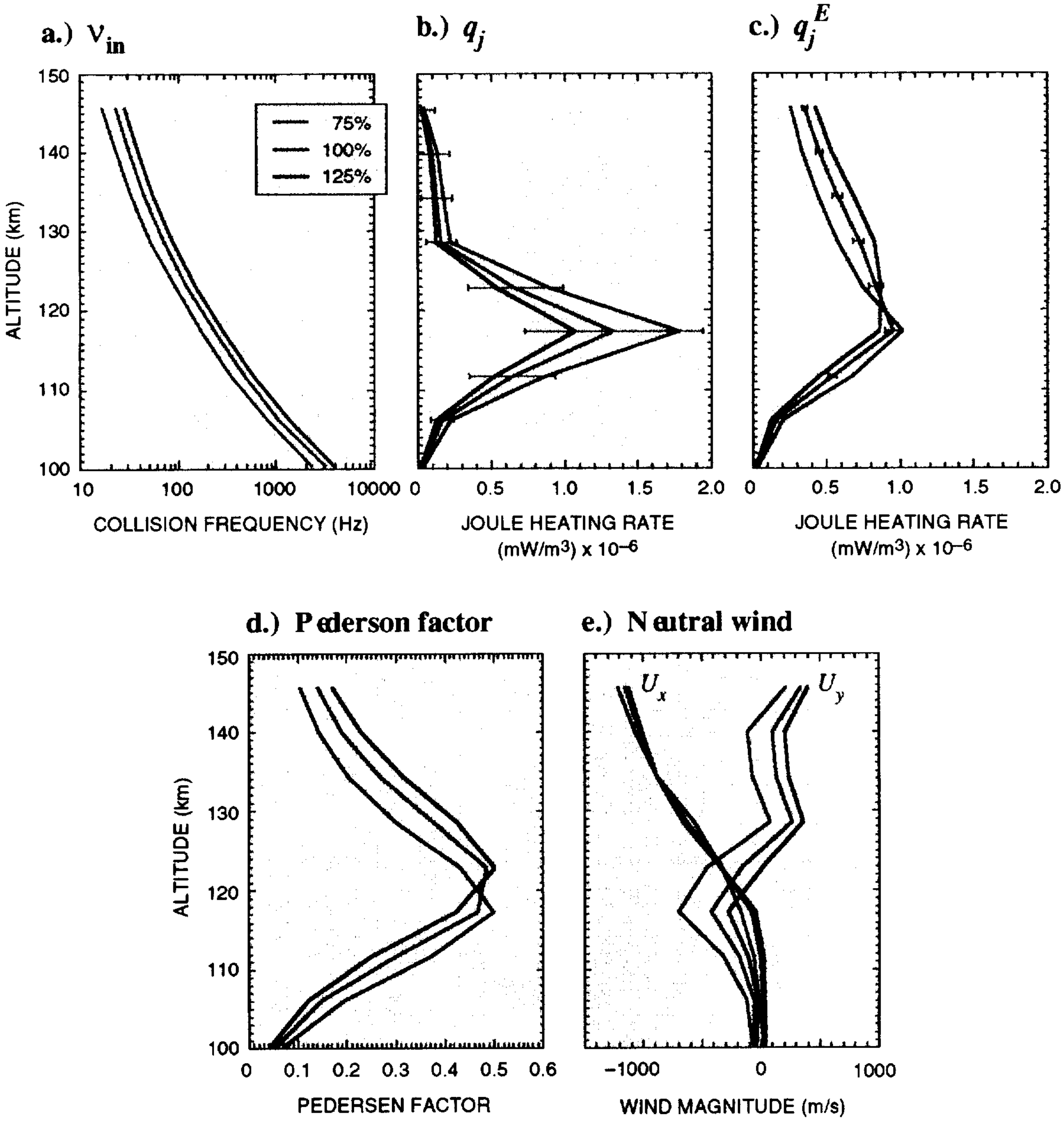

v97-012/f11

Figure 11